Fast optical recording of neuronal activity by three-dimensional custom-access serial holography

Walther Akemann, Sébastien Wolf, Vincent Villette, Benjamin Mathieu, Astou Tangara, Jozsua Fodor, Cathie Ventalon, Jean-François Léger, Stéphane Dieudonné, Laurent Bourdieu

▶ To cite this version:

Walther Akemann, Sébastien Wolf, Vincent Villette, Benjamin Mathieu, Astou Tangara, et al.. Fast optical recording of neuronal activity by three-dimensional custom-access serial holography. Nature Methods, 2022, 19 (1), pp.100-110. 10.1038/s41592-021-01329-7 . hal-03606564

HAL Id: hal-03606564
https://hal.science/hal-03606564

Submitted on 11 Mar 2022

Fast Optical Recording of Neuronal Activity by 3D Custom-Access Serial Holography

Walther Akemann[1], Sébastien Wolf[1,2,*], Vincent Villette[1,*], Benjamin Mathieu[1,*],
Astou Tangara[1], Jozsua Fodor[1], Cathie Ventalon[1],
Jean-François Léger[1,#], Stéphane Dieudonné[1,#,+], Laurent Bourdieu[1,#,+]

[1]Institut de Biologie de l'ENS (IBENS), École Normale Supérieure, CNRS, INSERM
[2]Laboratoire de Physique de l'ENS (LPENS), École Normale Supérieure, CNRS
Université PSL, 75005 Paris, France

*) contributed equally

#) shared senior authorship

+) corresponding authors

Correspondence:

laurent.bourdieu@ens.fr

stephane.dieudonne@ens.fr

Abstract

Optical recording of neuronal activity in 3D brain circuits at cellular and millisecond resolution *in-vivo* is essential for probing information flow in the brain. While random-access multiphoton microscopy permits fast optical access to neuronal targets in 3D, the method is challenged by motion artefacts when recording from behaving animals. Therefore, we developed 3D custom-access serial holography (3D-CASH). Built upon a fast acousto-optic light modulator, 3D-CASH performs serial sampling at 40 kHz from neurons at freely selectable 3D locations. Motion artefacts are eliminated by targeting each neuron with a size-optimized pattern of excitation light covering the cell body and its anticipated displacement field. Spike rates inferred from GCaMP6f recordings in visual cortex of awake mice tracked the phase of a moving bar stimulus with higher spike correlation between intra- compared to inter-laminar neuron pairs. 3D-CASH offers access to the millisecond correlation structure of *in-vivo* neuronal activity in 3D microcircuits.

Introduction

Large scale *in-vivo* imaging of neuronal activity[1,2] using multi-photon microscopy aims to decipher neural encoding and processing in distributed brain circuits during animal behaviors. However, the 3D structure of neuronal circuits operating on a time scale of milliseconds poses problem to conventional scanning microscopy as volumetric and millisecond acquisition are difficult to reconcile[3]. Volumetric multi-plane imaging[4–8] is limited to low sampling rates and low axial sampling densities as voxel acquisition is ultimately limited by the laser pulse rate. Spatial excitation multiplexing[9–13] improves 3D sampling, but extensive multiplexing degrades the signal-to-noise ratio, through accumulation of background fluorescence, and escalates brain heating[14,15].

Random-access multiphoton (RAMP) acquisition is a way to speed up sampling from distributed objects beyond image scanning[16,17]. RAMP targets a sequence of disjointed points of interest (POIs) in a non-contiguous 3D scan raster and thereby truncates spatial sampling for accelerated sampling in the time domain. 3D-RAMP has been implemented with acousto-optic deflectors (AODs), which control the 3D position of the excitation focus through tilt and defocus phase modulation of the scan beam[18]. RAMP recordings, however, were limited to *in-vitro* preparations[17,19,20] and to anesthetized animals[21–23], as recordings in awake animals suffered from brain motion-induced recording artefacts. To alleviate this problem, dedicated

AOD scan modes, such as patch scan[21,22] and scan of 3D hyper-surfaces[24], were deployed to acquire sufficient spatial information for *post-hoc* movement correction, but at the expense of temporal resolution. A recent solution to this problem applied on-line motion correction by tracking reference objects and adjusting the scan coordinates of an AOD-scanner in real time[25].

Here, we demonstrate a robust solution to the problem of motion artefacts in 3D-RAMP without interleaved imaging of reference objects, therefore offering faster sampling from neuronal populations. Previously, we demonstrated acousto-optic light modulation by a single pair of XY-AODs[26]. Here, we implement acousto-optic pulse-to-pulse light patterning and present a microscope for 3D-RAMP with holographic shaping of the two-photon excitation volume at 40 kHz. Using 3D custom-access serial holography (3D-CASH), we show that targeting single cells with an extended focus pattern imparts tolerance against tissue motion, while boosting the fluorescence yield. We illustrate 3D-CASH in recordings at high data throughput (20000 neurons per second) and high sampling rate (> 200 Hz) of GCaMP6f-expressing cortical neurons in layers 2/3 and 5 of primary visual cortex in behaving mice on a treadmill.

Results

Design of the 3DScope

The 3DScope (Fig. 1 and Extended Data Fig. 1) combines a 40 kHz chirped pulse laser amplifier, followed by a parametric wavelength converter (800-1300 nm), with two AODs (X-AOD and Y-AOD) of 15 mm aperture size and 23 μs cycle time. In each AOD, the laser beam is Bragg-diffracted from a 3D acousto-optic (AO) density grating formed by a propagating planar acoustic wave in a birefringent crystal. AO wave generation is carried out in a time-locked mode[26], in which frequency and amplitude-modulated (FM/AM) waves are generated under control of the laser clock and written anew for every laser pulse (Supplementary Fig. 1). This synchronous mode abolishes the focus drift associated with chirped AO gratings in earlier AOD-based 3D microscopes in asynchronous mode[20,22,27] and permits pulse-to-pulse linear (tilt) and quadratic (defocus) phase modulation for 3D access in sample space (Fig. 1a), as well as phase modulations of higher order (Supplementary Fig. 2).

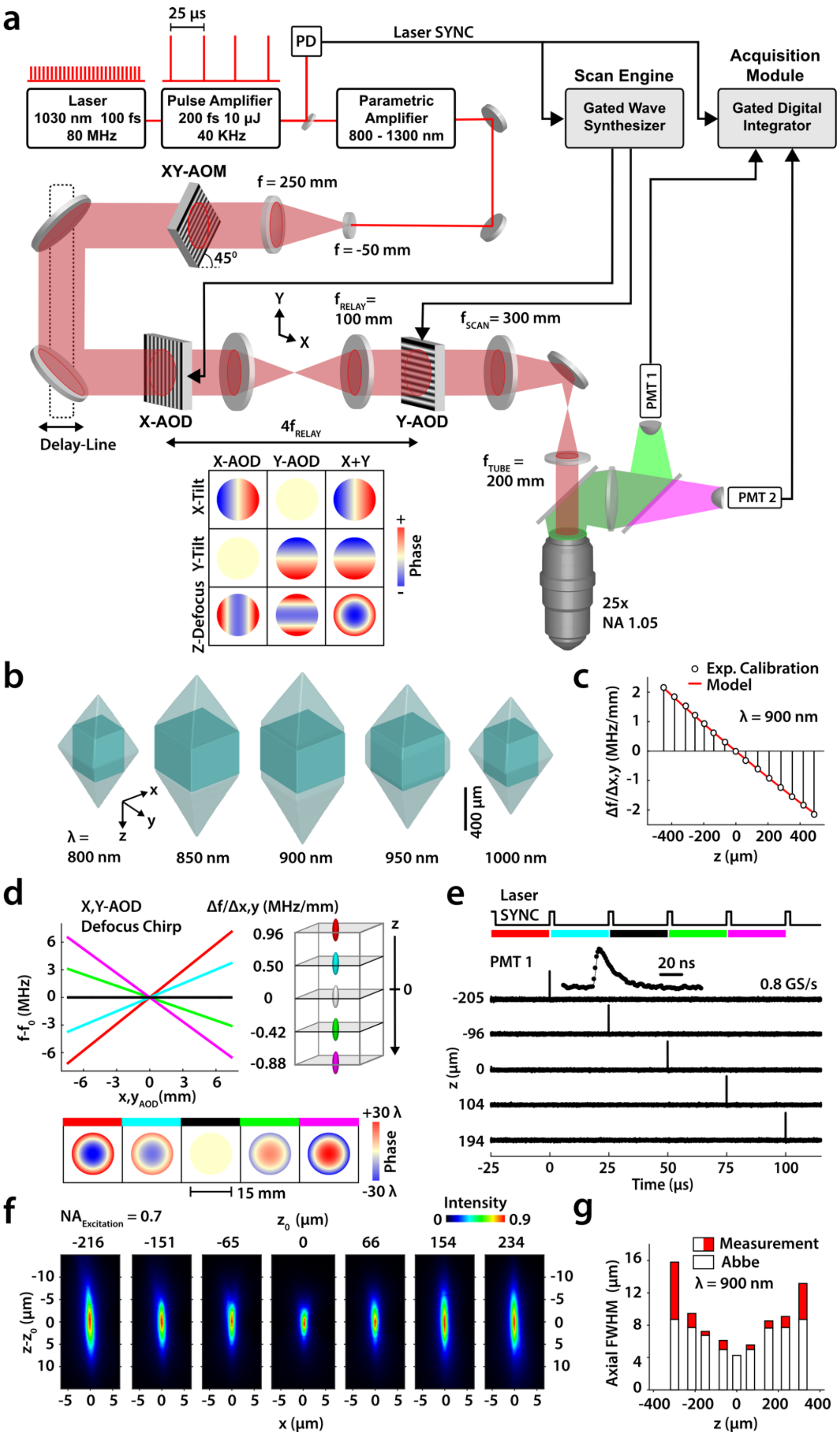

Fig. 1 Principle of the 3DScope

The 3DScope is a mirror-less scanning microscope for multi-photon excitation with full-frame, micro-frame and random address scan modes. **(a)** Schematic of the microscope: photo-multiplier tube (PMT), photodiode (PD), focal length (f), acousto-optic modulator (AOM), acousto-optic deflector (AOD), numerical aperture (NA) and laser emission synchronous timing signal (SYNC). Inset: Cartoon of spatial light modulation (x-tilt, y-tilt and z-defocus) by an X-AOD/Y-AOD tandem in 4f-configuration. **(b)** Total addressable 3D volume (semi-transparent) with embedded cuboid sub-volume of 400 μm height (solid color) modeled for a 25x objective. **(c)** Measured (black circles) and modelled (red line) calibration at 900 nm of AO linear frequency chirps producing z defocus up to ± 500 μm from the objective focal plane (z = 0). **(d)** Linear frequency chirps of -0.88 to +0.96 MHz/mm (left) together with resulting defocus phase modulation (0.75, 1.44, 0, -1.72 and -0.82 m defocus, respectively; bottom), same for both AODs, with each pulse targeting different depth (right). **(e)** Fluorescence measurement of a color plastic slide (500 nm thick) placed at axial target distances between -205 and +194 μm. For each target distance the defocus series (d) is repeated with every pulse given a different defocus chirp. Inset: detector signal at extended scale. **(f)** Maximum projection of the measured point-spread function (PSF) in the x-z plane for frequency chirps, from left to right, of 1.2, 0.77, 0.39, 0, -0.39, -0.77, -1.2 MHz/mm. **(g)** Full width at half maximum (FWHM) of the measured axial PSF (white and red bars combined) for axial targets at -400 to +400 μm and expected FWHM from an ideal Abbe objective (white bar).

The addressable volume is delimited by a bipyramidal boundary set by the AOD frequency bandwidth and the laser wavelength (Fig. 1b), offering a 500 x 500 μm^2 field of view under 25x objective magnification (Supplementary Fig. 3a). The measured axial focus shift is a linear function of the acoustic wave frequency chirp in agreement with the theory (Fig. 1c). We demonstrate pulse-to-pulse phase modulation by subjecting five consecutive laser pulses to AO frequency ramps of different slopes (Fig. 1d), which resulted in each pulse being focused to a different plane, about 100 μm apart (Fig. 1e). At zero chirp the point-spread function (PSF) had an axial full width at half maximum (FWHM) of 4.2 ± 0.8 μm (Supplementary Fig. 3b) consistent with a reduced excitation numerical aperture (NA_{ex} 0.7). In the presence of chirp, the FWHM broadened with distance of the focus from the objective focal plane (Fig. 1f). Within a distance of 200 μm the FWHM remains below 8 μm and is to 90 % explained by spherical aberration of an ideal Abbe objective receiving wave fronts with quadratic curvature[28] (Fig. 1g).

Acousto-optic patterning of light by single pulse holography

Susceptibility to target-motion-induced recording artefacts is the major setback of *in-vivo* RAMP recording. In addition, because of the low laser rate, the 3DScope is bound to low signal-to-noise ratios with diffraction-limited single focus excitation given that every molecule in the focal volume can emit at most one photon per laser cycle. We reasoned that both issues may be solved by extending the focal volume to sample a larger portion of each cell including its excursion space. For this, we first explored the light patterning function of the 3DScope. We derived biaxial phase and intensity holograms from the desired target pattern using a Gerchberg-Saxton algorithm[29] (Fig. 2a). By designing patterns of equidistant diffraction-limited foci we intended to multiplex the excitation volume, while limiting laser power dilution (Fig. 2b). To confirm designed patterns, we imaged the two-photon fluorescence emission of a thin fluorescein layer (Fig. 2c). We found good agreement between intended (Fig. 2b) and measured patterns (Fig. 2d) in the FM/AM mode. In FM only mode, however, the intensity became unequally distributed among spots, and side lobs appeared (Fig. 2d), in agreement with fast Fourier transform (FFT) reconstruction of the hologram (Supplementary Fig. 4). Therefore, the FM/AM mode provides higher fidelity to the target pattern than the FM mode, albeit at reduced power transmission. The size of single spots in a multi-spot array equals the focus size in the absence of holographic modulation, independent of the number of spots (Fig. 2e) and axial broadening in the presence of defocus is also identical (Fig. 2f). Finally, we devised holograms creating 3x3, 5x5 and 2x5 spot patterns (Fig. 2g, h) consistent with FFT reconstruction (Supplementary Fig. 5). The freedom to program spot density and distances and adapt these patterns on a pulse-to-pulse basis is the core element behind 3D-CASH.

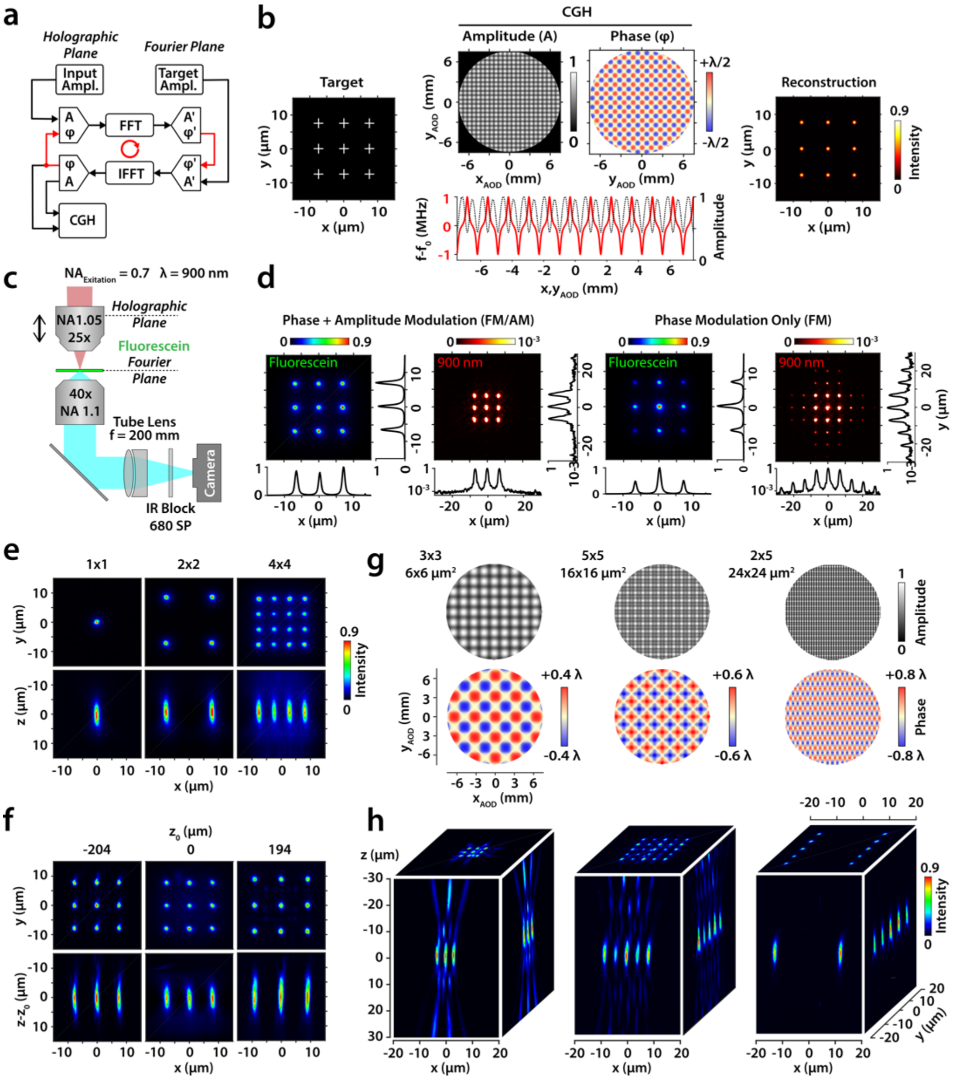

Fig. 2 Acousto-optic patterning of light

The 3DScope integrates spatial light modulation for holographic patterning of excitation light. **(a)** Computer-generated holograms (CGHs) are derived from a desired target intensity pattern by iterative phase retrieval through forward (FFT) and inverse (IFFT) fast Fourier transformation of the light fields (amplitude A and phase φ) in the holographic and Fourier planes. The iteration loop indicated in red. **b)** Example of a 3x3 (15x15 μm^2) target pattern (left), the CGH derived from the target (middle, top), the FM/AM acousto-optic modulation, identical for X- and Y-AODs, with f_0, the carrier frequency (middle, bottom) and reconstruction of the CGH by 2D-Fourier transform (right). **(c)** Experimental configuration for experimental reconstruction of the CGHs. **(d)** From left to right: Two-photon fluorescence image of a 10-20 μm thin aqueous fluorescein solution with holographic illumination (900 nm) using the CGH in (b) together with saturated infrared intensity image, after removal of the IR block, for FM/AM (left) and FM only (right). Intensity projections are shown next to each image. **(e)** Measured fluorescein fluorescence without hologram (1x1) and with (2x2)- and (4x4)-hologram. **(f)** Measured fluorescein fluorescence with (3x3)-hologram and with (left and right) and without (middle) defocus. **(g)** CGHs for the 3x3 (6x6 μm^2), 5x5 (16x16 μm^2) and 2x5 (24x24 μm^2) patterns. **(h)** Images obtained from the experimental reconstruction of CGHs in (g). All images represent maximum projections with respect to the perpendicular dimension.

Imparting motion tolerance to *in-vivo* 3D-RAMP recording

We then asked whether grid spot illumination can aid to stabilize RAMP point recordings against *in-vivo* brain tissue motion in awake mice (Fig. 3a). We first quantified from time lapse movies the lateral movements of cell bodies in head-fixed mice expressing EGFP under the GAD65 promoter (Fig. 3b). We found complex patterns of movement, with considerable cell displacements also in the absence of locomotion (Fig. 3b). In-plane motion was limited to a displacement space of 2 to 6 μm diameter, depending on the depth below pia (Fig. 3b,c), akin for axial motion (Supplementary Fig. 6). To test whether covering this space by a large enough grid pattern could counteract motion artefacts in RAMP recordings, we recorded EGFP fluorescence from cell body-centered POIs in the RAMP mode at 2.5 kHz while targeting each POI with a single spot focus and a 5x5 (15x15 μm^2) grid focus in pulse-to-pulse alternation (Fig. 3d). In the single-spot mode, the RAMP signal exhibited large-amplitude fluctuations giving rise to skewed noise distributions (Fig. 3e,f), while under grid-spot illumination this noise was diminished to low residual excess kurtosis (0.57 ± 0.43, mean ± standard deviation (SD) throughout, unless stated otherwise; 37 cells; Fig. 3f,g) approaching photonic shot noise. Patterned illumination therefore proves efficient in preventing motion-induced noise in *in-vivo* RAMP recordings. Next, we asked whether holographic illumination also entails gain in signal-to-noise ratio. In anesthetized mice, to minimize tissue movement, the fluorescence signal as a function of excitation power followed the gain curve of a two-photon absorption process, reaching half-saturation at 0.21 and 0.78 mW for a 1x1 and a 3x3 (4x4 μm) focal pattern, respectively, and with the 3x3 pattern yielding 3.4 times higher fluorescence (Fig. 3h). From the signal-to-noise ratio (SNR) we obtain a lower estimate of the number of detected photons per laser pulse (equal to SNR^2, Fig. 3h) reaching 1000 photons at saturation. EGFP photobleaching occurred with $4.3 \cdot 10^{-6}$ quantum yield (115 ± 142 s time constant at 2 kHz, 55 ± 22 % amplitude, 20 cells) at 25 % saturation, in agreement with reported data of GFP under low pulse rate excitation[30].

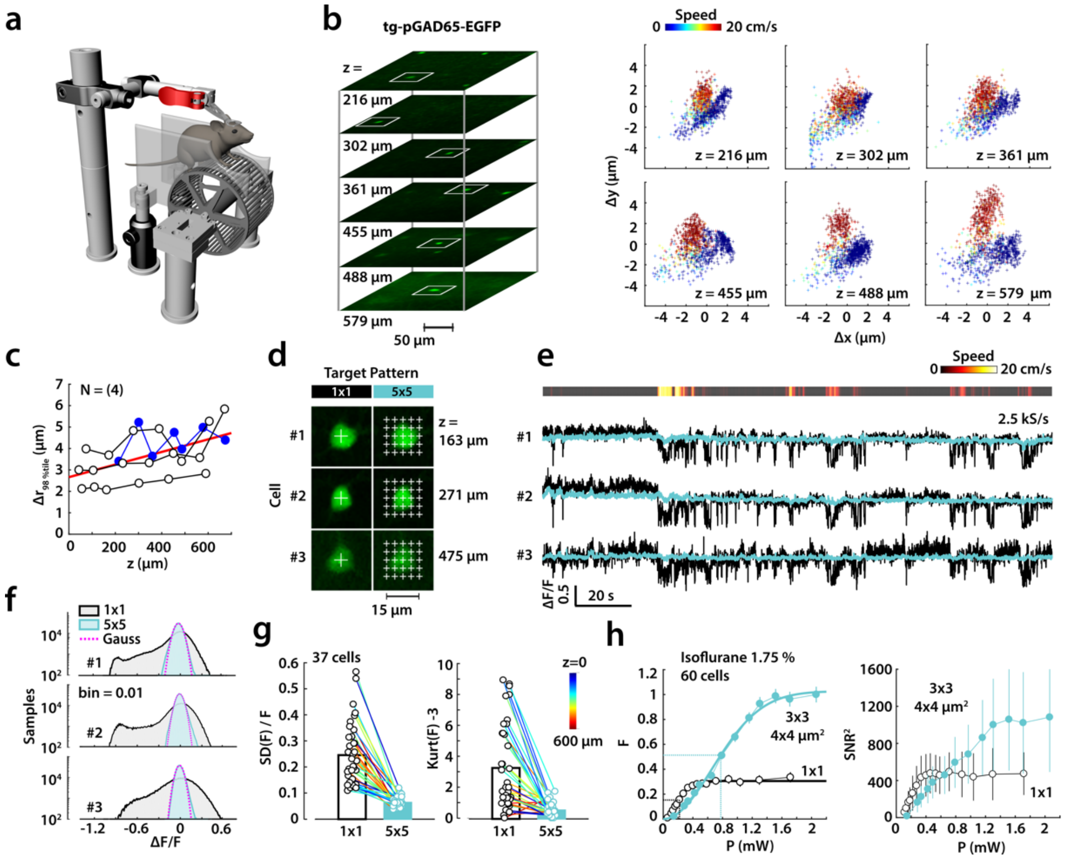

Fig. 3 Holographic illumination for stable RAMP recording in awake mice

(a) Head-fixation for mice implanted with a 5 mm cranial window over primary visual cortex walking on a treadmill. **(b)** Left: Optical sections from a two-photon fluorescence z-stack with selected cell bodies marked as white rectangles in a pGAD65-EGFP transgenic mouse. Right: x,y-Positions of selected cells given as deviation from the barycenter from time lapse movies recorded at 6 frames/s. Every data point is color-coded for simultaneously recorded walking speed. **(c)** Summary of cellular displacements (98 percentile of radial deviation from the barycenter; N = 4 animals) versus z-depth below pia. Linear fit to the data (slope 0.3 %) in red. Data of example (b) in blue. **(d)** Fluorescence images of three cell bodies overlaid with a 1x1 and a 5x5 target pattern. **(e)** Bottom: RAMP fluorescence traces obtained from cells in (d) during 180 s with pulse-to-pulse alternation between 1x1 (black) and 5x5 (cyan) pattern excitation at 2.5 kHz sampling rate (2.5 kS/s). Top: Speed of the animal. **(f)** Histograms of the fluorescence traces in (e) including Gaussian fit to data obtained under 5x5 excitation. **(g)** Analysis of data like in (f) including 37 cells. Left: Relative noise defined as standard deviation (SD) of the time series data divided by the median of the fluorescence (F). Right: Excess kurtosis (Kurt). **(h)** Measurement of fluorescence yield under 1x1 and 3x3 (4x4 µm^2) excitation measured under isoflurane anesthesia (60 cells). Left: Normalized mean fluorescence during 2 s recordings versus mean excitation power (P; measured under the objective) with fits to the gain curve of two-photon absorption (solid lines). Right: Squared signal-to-noise ratio (SNR) of the same data. Error bars represent SD.

Removing neuropil activity from GCaMP6f CASH recordings

Grid illumination of neurons expressing a neuronal activity indicator will yield a mixed signal of single-cell and multicellular activity, with the latter originating from the surrounding neuropil covered by the grid and from out-of-focus excitation. To extract the single-cell signal, we record a neuropil reference signal from an excitation pattern composed of two lines of foci outside of the grid target (Fig. 4a). The two patterns are then toggled from pulse to pulse such that two laser pulses are deployed to each cell before moving on to the next cell. We tested this protocol in layer 2/3 (L2/3) and layer 5 (L5) neurons of primary visual cortex (V1) expressing GCaMP6f and tdTomato in presence of Cre recombinase. From an imaging stack we selected CaMP6f-positive neurons (Fig. 4b,c), with some of them co-expressing tdTomato, and recorded GCaMP6f and tdTomato fluorescence signals in 3D-CASH mode. GCaMP6f photobleaching was negligible during 300 s recording trials, which were equivalent to an exposure to 72,000 laser pulses, except for a fast initial bleaching transient of $9.5 \cdot 10^{-5}$ quantum yield (44 ± 15 s time constant at 0.24 kHz, 10 ± 5 % amplitude, 84 cells) appearing only in the very first trial. The fluorescence signals of the cell body (CB) and neuropil (NP) were strongly correlated, while the tdTomato signal remained flat (Fig. 4d). To estimate the true cellular signal, we subtracted the neuropil signal from the CB signal using a global weight factor (α). Noise regression yielded similar α values as correlation regression[31,32], which increased with depth (Fig. 4e and Supplementary Fig. 7). Both regressions descended to the same level of residual baseline noise in this example (3.1 ± 0.4 %; 74 cells; Fig. 4f) and in pooled data (3.3 ± 0.5 %; 4 animals; Fig. 4h). After neuropil correction, pairwise correlations of the fluorescence signals were reduced six-fold to a residual value of 0.13 in one example (Fig. 4g) and 0.15 ± 0.08 in pooled data (Fig. 4h) suggesting that holographic illumination does not impart higher neuropil contamination than standard imaging techniques[32,33]. Furthermore, simultaneous CASH and image acquisition revealed consistent GCaMP6f signaling (0.95 ± 0.1 median trace correlation; 19 cells; Extended Data Fig. 2). The GCaMP6f signal rises in many cells during locomotion (Fig. 4i), consistent with increased spike rates in V1 neurons during locomotion in the dark[34]; and overlay of the fluorescence traces with MLspike[35]-inferred spikes (Fig. 4j) showed an increased spike rate during locomotion (Supplementary Fig. 8). As a control for possible locomotion artefacts, MLspike detected only one false event in simultaneously recorded tdTomato traces (10 cells; 50 min recording time).

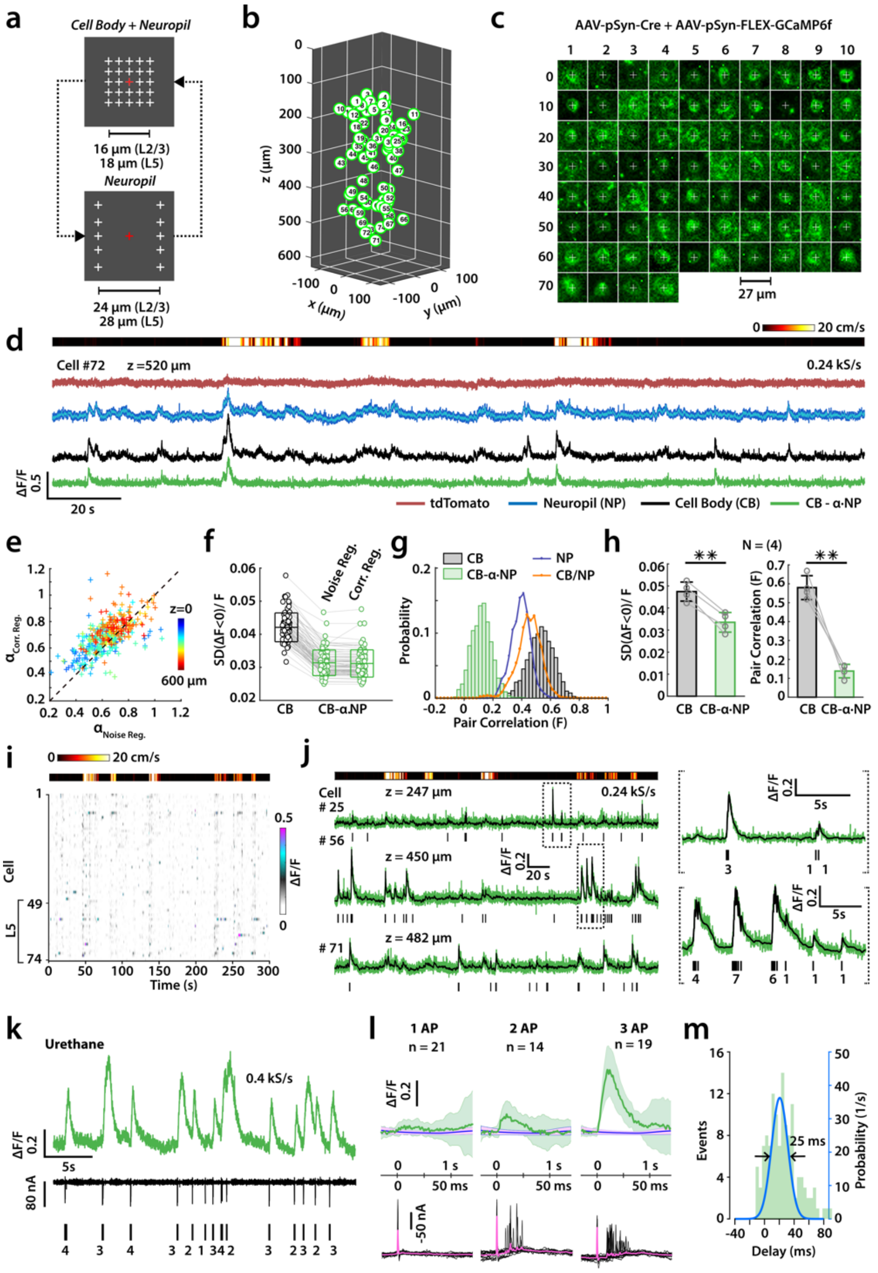
a
Cell Body + Neuropil
16 µm (L2/3)
18 µm (L5)
Neuropil
24 µm (L2/3)
28 µm (L5)
b
z (µm)
x (µm)
y (µm)
c
AAV-pSyn-Cre + AAV-pSyn-FLEX-GCaMP6f
27 µm
0 20 cm/s
d
Cell #72 z =520 µm
0.24 kS/s
ΔF/F 0.5
20 s
tdTomato
Neuropil (NP)
Cell Body (CB)
CB - α·NP
e
$\alpha_{\text{Corr. Reg.}}$
$\alpha_{\text{Noise Reg.}}$
z=0
600 µm
f
SD(ΔF<0)/ F
Noise Reg.
Corr. Reg.
CB
CB-α.NP
g
CB
CB-α·NP
NP
CB/NP
Probability
Pair Correlation (F)
h
N = (4)
**
SD(ΔF<0)/ F
Pair Correlation (F)
CB
CB-α·NP
i
0 20 cm/s
Cell
L5
Time (s)
ΔF/F
j
Cell #25 z = 247 µm
0.24 kS/s
#56 z = 450 µm
#71 z = 482 µm
ΔF/F 0.2
20 s
5s
3
1 1
4 7 6 1 1 1
k
Urethane
0.4 kS/s
ΔF/F 0.2
5s
80 nA
4 3 4 3 2 1 3 4 2 3 2 3 2 3
l
1 AP n = 21
2 AP n = 14
3 AP n = 19
ΔF/F 0.2
1 s
50 ms
-50 nA
m
Events
Probability (1/s)
25 ms
Delay (ms)

Fig. 4 Neuropil correction of GCaMP6f-RAMP recordings

(a) CASH target patterns for sampling a cellular signal with a neuropil component. Target center marked as red cross. **(b)** 3D coordinates of 74 cells selected from a full-frame z-stack obtained from a mouse expressing GCaMP6f in cortical neurons in layers L2/3 and 5. **(c)** Fluorescence images of cells in (b). **(d)** Example recordings of, from top to down, motion speed, tdTomato fluorescence (red), GCaMP6f neuropil fluorescence (NP, blue), cellular GCaMP6f signal (CB, black) and the corrected GCaMP6f signal after global noise regression (CB-αNP, green). **(e)** Regression parameter obtained from correlation versus noise regression of 300 s recordings (5 repetitions) with identity line (red dashes). **(f)** Baseline noise for raw and corrected data in 300 s recordings with box width representing SD. **(g)** Pearson pairwise correlation. **(h)** Mean baseline noise (left) and and mean pair correlation (right) of paired (gray lines) raw (black) and corrected data (green). Paired t-test (two-sided) $p = 0.003$ (**; N = 4 experiments; 4 animals). Error bars represent SD. **(i)** False-color representation of fluorescence traces after noise regression for all cells, shown in (b) and (c) with walking speed (top). **(j)** Left: Fluorescence traces (green), overlaid with MLspike-deconvoluted traces (black) and inferred spikes (black bars; below). Right: Extended views with numbers of spikes (below). **(k)** Simultaneous CASH (green) and electrode recording (loose patch; black) of a spontaneously active cell (L2/3; z=225 μm) under urethane anesthesia with burst spike counts (bottom). **(l)** Top row: Spike triggered average GCaMP6f responses (green; ± SD) for single spikes (1 AP; 21 events), spike doublets (2 AP; two spikes within a 30 ms window; 14 events) and triple spikes (3 AP; 30 ms window; 19 events) together with bootstrap noise (blue/magenta; ± SD). Bottom row: Electrode currents (black) with the first spike at time zero and current average (magenta). **(m)** Histogram of latency (green) of MLspike-inferred relative to electrode-detected spikes within a 0.2 s time window and Gaussian density (blue; 25 ms FWHM; 23 ms mean).

To estimate the goodness of spike inference, we applied spike deconvolution to simulated data. The combined error rate of spike detection decreased with increasing sampling rate, attaining 25 % or 10 % for SNR 2 or 4, respectively, at 200 Hz, provided neuropil correction was included (Extended Data Fig. 3). To test these predictions, we recorded the membrane activity through a cell-attached electrode simultaneously with CASH under urethane anesthesia (Fig. 4k, Extended Data Fig. 4). Event sorting revealed the spike-triggered average waveform of the GCaMP6f response to 1 to 3 action potential (APs) events within a 30 ms summation window (Fig. 4l). These events were detected by MLspike with probabilities of 0.46 (1 AP), 0.73 (2 AP) and 1 (3 AP), respectively (104 events, 1 cell, Extended Data Fig. 4e), with latencies of detected versus true spikes centering at 23 ms with a 25 ms distribution width (Fig. 4m). Receiver operating analysis with a probability discriminant (Extended Data Fig. 4e,f) revealed $\Delta F/F$ amplitude responses of 0.076 ± 0.01 (1 AP), 0.24 ± 0.02 (2 AP) and 0.46 ± 0.02

(3 AP), implying 1.64 ± 0.01 Hill non-linearity (Extended Data Fig. 4g) in agreement with the literature[36].

Tuning of V1 neurons to oriented visual contrast

Providing large volumetric depth (> 400 μm), 3D-CASH affords access to the columnar extent of cortical neuronal activity. We simultaneously recorded GCaMP6f activity of neurons in layers 2/3 and 5 of V1 cortex in response to moving contrast gratings in awake mice. For selection of active cells, we manually chose cells from a stack recorded during presentation of visual noise (Fig. 5a). Single-trial responses to contrast gratings displayed gain-modulation by motor activity[37] (Extended Data Fig. 5 and 6). To discount the effect of locomotion on measured tuning properties, we averaged the responses over 20 stimulus repetitions (Fig. 5b). In this experiment, 53 of 57 selected cells responded significantly ($p < 0.002$, bootstrap test) to the stimulus and among these 32 cells displayed significant orientation tuning ($p \leq 0.03$; Fig. 5c-f). The global tuning index (gOSI) ranged from 0.1 to 0.7 and was more pronounced than directional tuning (Fig. 5c). Projection of tuning angle on cell position indicates an absence of orientation clusters (Fig. 5d and Supplementary Fig. 9). Single-trial responses showed large variability including oscillatory, ramp-like and failure responses (Fig. 5g,h). In pooled data (3 animals), about 70 % of selected cells were responsive and 50 % orientation-tuned (Fig. 5i). The tuning angle obtained from the tuning curve (OSI, orientation sensitivity index; Fig. 5f) was consistent with the angle obtained from the vector sum (Fig. 5j). Across 270 tuned cells, tuning angles were homogeneously distributed between 0^{o} and 180^{o}, independent of depth (Fig. 5k) and of layer, and visual responses were positively correlated to locomotion (Fig. 5l). In one experiment, we recorded visual responses in the same cells (L2/3, 36 cells) in the awake and anesthetized state (Extended Data Fig. 7). Under isoflurane, layer 2/3 cells showed higher response probability with 3-fold larger mean response and lower inter-trial variance compared to the awake condition (Extended Data Fig. 7d-g), as well as higher spontaneous spike rates (Extended Data Fig. 8).

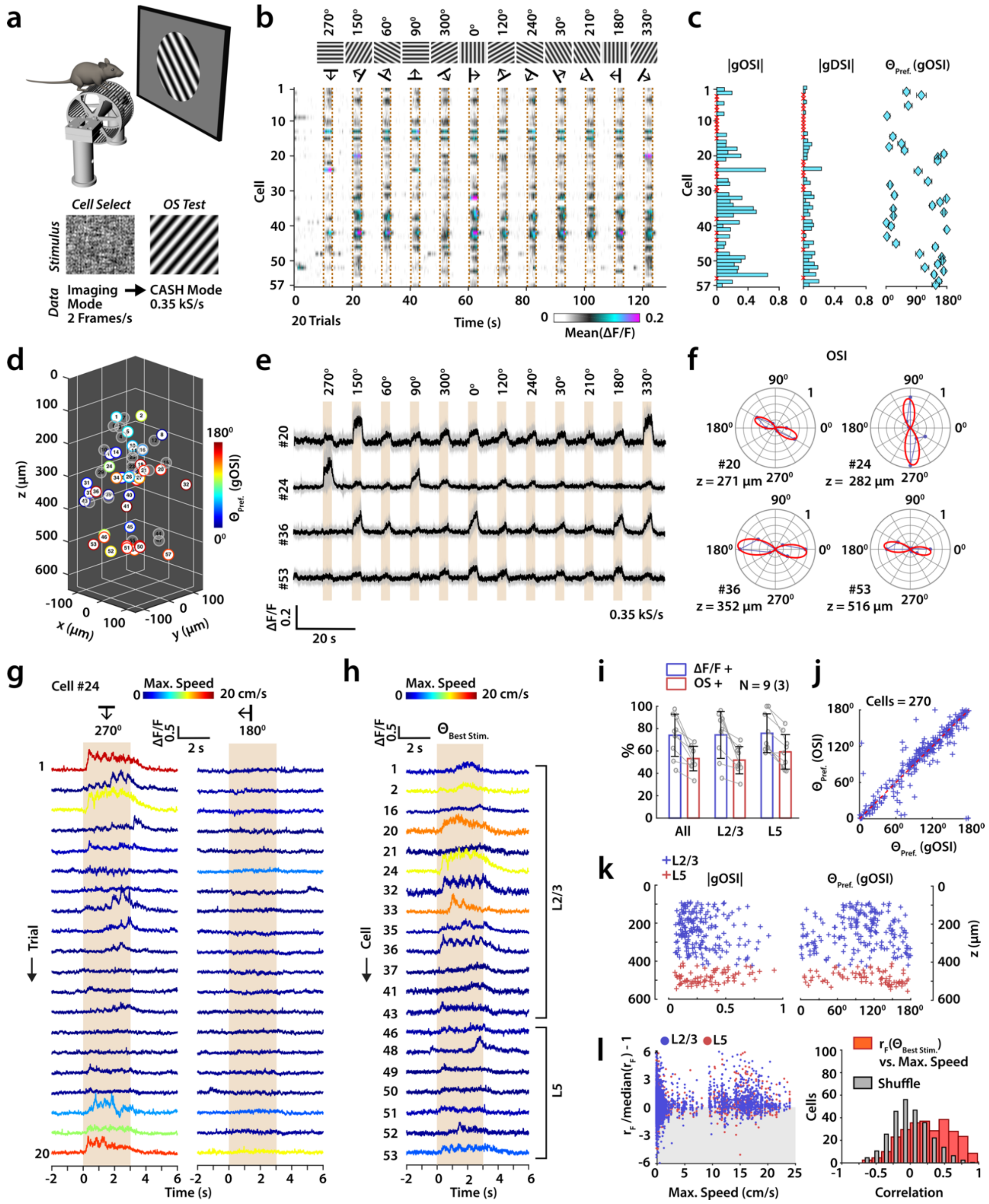

Fig. 5 Orientation tuning of neurons in V1 cortex

(a) Awake mouse on a treadmill with visual stimuli presented in the left visual field. The stimulus is a filtered noise movie (imaging mode) or moving contrast gratings (CASH mode; OS, Orientation Sensitivity). **(b)** Trial-averaged fluorescence traces of 57 neurons (20 trials; 350 Hz sampling) with grating stimuli of varying orientation (top). **(c)** Magnitude of global orientation selectivity index (gOSI), global direction selectivity index (gDSI) and gOSI tuning angle, evaluated for neurons exhibiting significant response and orientation tuning. Neurons that failed statistical testing marked as red crosses. **(d)** 3D coordinates of recorded neurons with color coding for tuning angle. Unresponsive neurons in gray. Z-axis aligned to the pia mater (z = 0). **(e)** Trial-averaged fluorescence traces (black) with SD (gray) of four example neurons. **(f)** Orientation selectivity index (OSI) calculated from the fluorescence responses in (e). **(g)** Single-trial fluorescence responses of cell #24 to the preferred orientation (270°) and orthogonal orientation (180°) with traces color-coded for the maximum speed of locomotion. **(h)** Montage of single-trial fluorescence responses of 20 cells selected from 36 tuned cells by choosing for each cell the stimulus trial of maximum integral response, using the same color code as in (g). Putative laminar cell position in layer 2/3 (L2/3) or layer 5 (L5) indicated by brackets. **(i)** Fractions of visual responsive (blue) and orientation-tuned cells (red). Paired data from 9 experiments (514 cells in total; 3 animals) connected by gray lines. Error bars represent SD. **(j)** Correlation diagram of gOSI- and OSI-derived tuning angles. **(k)** Amplitude of orientation tuning (|gOSI|) and gOSI-derived tuning angle for the whole dataset (270 cells; 3 animals) versus z-position and assignment to cortical layers 2/3 (blue) and 5 (red). **(l)** Left: Single-trial fluorescence amplitude (r_F) in response to the best stimulus normalized by the median of responses across all trials as function of maximum speed. Right: Histogram of correlation coefficient between single-trial response amplitude to the best stimulus and the maximum speed (red).

Temporal structure of the visual response and pairwise correlations

Finally, exploiting the temporal resolution of 3D-CASH (0.5 to 10 ms in the 3DScope, depending on sample size), we aimed to extract the temporal information present in single-cell GCaMP6f responses and across the entirety of simultaneously recorded cells. First, to test the dependence of the GCaMP6f response on a temporal stimulus parameter, we varied the stimulus frequency between 1 and 4 Hz for two orthogonal stimulus directions (0° and 90°; Fig. 6a). In the example cell (Fig. 6b,c), the GCaMP6f signal tracked the phase of the stimulus (Fig. 6b) and the time-resolved FFT spectrum exhibits an amplitude peak at each stimulus frequency tested (Fig. 6c) in absence of stimulus artefacts (Supplementary Fig. 10). For a set of orientation-sensitive cells we constructed the peri-stimulus time histogram (PSTH) of inferred spikes for the preferred angle and calculated for every PSTH the ratio of the first harmonic with respect to the mean rate (R_1/R_0; Fig. 6 d-f and Extended Data Fig. 9). The pooled data (Fig. 6g) show a broad distribution with weak bimodality, ranging from non-phasic to phasic responses (Extended Data Fig. 10).

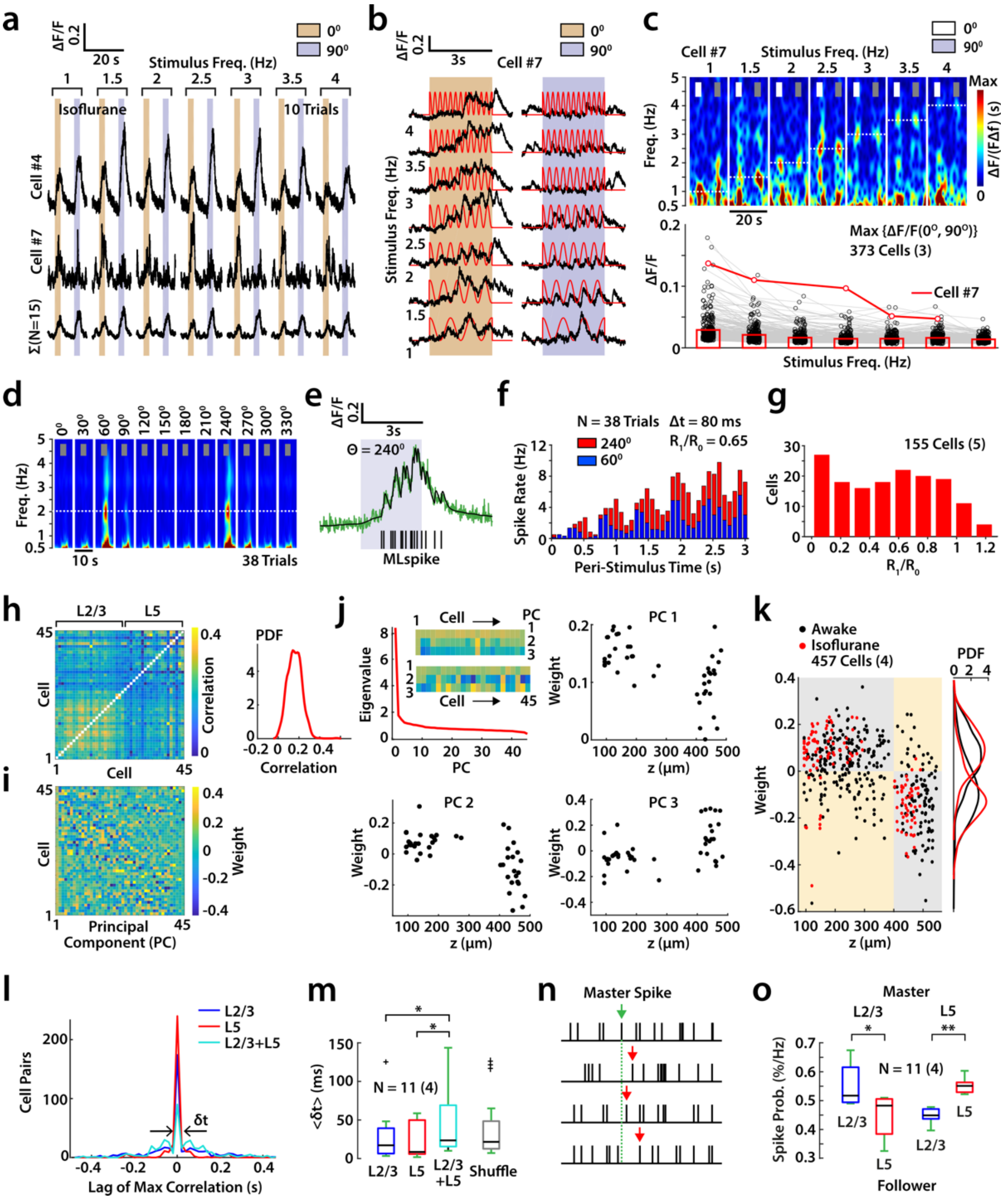

Figure 6: Temporal response properties and population correlation analysis

(a) Trial-averaged fluorescence responses (10 trials; 445 Hz sampling) to contrast gratings of 0° and 90° orientation and 1 to 4 Hz frequency for two example cells (top) and a 15-cell average (bottom) under isoflurane. **(b)** GCaMP6f responses (cell #7) overlaid with the temporal phase of the stimulus (red lines). **(c)** Top: Short time Fourier transform (STFT) of the trial-averaged stimulus response (cell #7) for 1 to 4 Hz stimuli (white dashed lines). Bottom: Maximum Fourier amplitude (0° and 90° orientation) of the GCaMP6f response versus stimulus frequency (10 trials; 373 cells; L2/3) with population mean (red bar). **(d)** STFT of the GCaMP6f response at constant temporal (2 Hz; dashed white line) and spatial (0.04 cpd, cycles per degree) frequency (example cell; 38 trials). **(e)** Single-trial GCaMP6f response (green) to the best stimulus (240°; gray) together with MLspike-reconstructed response (black) and inferred spikes (vertical bars, black). **(f)** Peri-stimulus time stacked histogram (PSTH) of the spike rate of the stimulus response to 240° (red) and 60° (blue) orientation (38 Trials, R_1/R_0

harmonic ratio). **(g)** R_1/R_0 histogram (155 cells; L2/3; 5 animals). **(h)** Left: Pearson correlation matrix of GCaMP6f data (45 cells; awake state) during visual stimulation (protocol Fig. 5b; 444 Hz sampling; 130 s). Correlation means: 0.25 (L2/3), 0.14 (L5) and 0.17 (interlaminar pairs). Right: Probability density function. **(i)** Principal Components (PCs) of the correlation matrix in descending order of eigenvalue. **(j)** Top left: Eigenvalues and (inset) the first three PCs. Bottom left and right: Weights of PCs 1 to 3 as a function of z-depth. **(k)** Pooled data (457 cells; 4 animals), including experiments under isoflurane (red) showing PC weights versus z-depth. **(l)** Time lag histogram of maximum cross-correlation between cell in L2/3 (blue), L5 (red) and inter-layer pairs (black). **(m)** Width, δt, of the zero lag correlation peak (SD; 11 recordings, 4 animals). Unpaired t-test (two-sided) of cross-laminar (L2/3+L5) neuron pairs versus pairs within L2/3 ($p = 0.03$) and L5 ($p = 0.04$). As control, cells were z-shuffled. Boxplot shows median (bar; black) 1st and 3rd quartile (box), ± 2.7 SD range (green) and outliers (black). **(n)** Schematic showing spike delays between a master spike (green) and follower spikes in three neurons (red). **(o)** Probability that the neuron to spike first following a spike in a master neuron is located in L2/3 or L5, normalized by cell count and mean firing rate in the follower layer. P-values $3 \cdot 10^{-2}$ (*) for L2/3 masters and $2.4 \cdot 10^{-3}$ (**) for L5 masters (unpaired t-test; two-sided; N=11 experiments; 4 animals; $8 \cdot 10^5$ spikes). Boxplot analogous to (m).

We then asked how GCaMP6f signals of V1 neurons are correlated among cells distributed across layers 2/3 and 5. Pairwise correlations evaluated from entire trials are higher among layer 2/3 than among layer 5 cells or pairs between the two layers (Fig. 6h). Principal component analysis of the correlation matrix (Fig. 6i) revealed a highest-ranking component (PC1) with uniform weights across neurons (Fig. 6j), suggesting global correlation, and a second-ranking component (PC2) with weights of opposite signs for neurons in layer 2/3 versus layer 5 (Fig. 6j and Fig. 6k for pooled data; 4 animals). From this we hypothesized higher spike synchronicity between intra-laminar versus inter-laminar neuron pairs. Indeed, the zero-peak width, δt, of the cross-correlation histogram (Fig. 6l) was significantly lower for intra-laminar compared to inter-laminar pairs ($p = 0.03$ and 0.04, t-test; Fig. 6m). Next, we asked how this observation is represented in the temporal structure of spike activity. For every cell, we calculated for every BSD[38]-inferred spike as master spike the time delay to the closest follower spike among all other cells (Fig. 6n). This analysis showed that spikes emitted from neurons in a given layer are more likely followed by a closest spike in a neuron of the same layer with a mean latency of 17 ± 60 ms (Fig. 6o and Supplementary Fig. 11).

Discussion

The present data highlight the utility of CASH to speed up *in-vivo* calcium measurement from cell somata in optically accessible 3D neuron populations. With a throughput of 20,000 neurons per second in CASH mode, the 3DScope constitutes a substantial gain over earlier 3D-AOD microscopes (< 1,000 neurons/s)[24,39]. In CASH, the number of single-cell POIs , n_{cells}, is given by $n_{cells} = r_{data}/r_{acq}$ with r_{data}, the data throughput of the microscope, and r_{acq}, the sampling rate. Larger sample size therefore entails lower sampling rate, while the GCaMP6f response-to-noise ratio (RNR) scales with $\sqrt{r_{acq}}$ (Supplementary Discussion). This trade-off between sample size and RNR ultimately defines how many POIs can be sampled at a given level of spike inference error. In the case of densely distributed cortical cells, we expect CASH to yield similar effective SNR as standard 2D two-photon imaging, whereas superior SNR is obtained for sparsely distributed targets (Supplementary Discussion). At the same time, sparse cell labeling helps to isolate single cells within the patterned excitation volume and, by minimizing background fluorescence, maintain high probe sensitivity under 2-photon excitation.

Earlier AOD-based 3D microscopes employed counterpropagating sibling gratings in two AODs in series to cancel focus drift induced by linear frequency chirp in asynchronous mode[20–22]. This scheme, however, does not prevent focus drift for non-linear chirps[40] and suffers from low power transmission, because of the second AOD receiving input in mismatch with the Bragg angle, and from vanishing duty cycle for large defocus[18]. Resonant 3D mirror scanners, on the other hand, are limited to low sampling rate (< 20 Hz) in few planes[8,41] in spite of high nominal throughput (> 10 megapixels/s) as only a minority of pixels contribute useful information. While recent smart sampling methods achieve up to kHz speed, these methods were limited to 2D-distributed targets in the focal plane[42–44]. To achieve similar sampling speed, but from 3D-distributed targets, 3D-CASH takes a fundamentally different approach. In CASH, the principal source of speed gain is random access, not large-scale multiplexing. Single-shot excitation volumes remain confined to individual cells and their immediate environments, which results in non-mixed cellular data at low laser power (< 0.4 mW per spot in the 5x5 grid) safely below known thresholds of heating damage[15].

Our data reproduce observations in the rodent visual system, in particular similar orientation tuning of neurons in layers 2/3 and 5[45], absence of spatial orientation clusters[46] and modulation by locomotion[37], while *a priori* selection of cells in CASH assessed a larger population of visual responsive V1 cells than previously reported[36]. Phase sensitivity of the visual response reflects excitation modulation of V1 neurons by contrast bars moving across neuronal receptive fields[47]. At fixed stimulus periodicity, and without distinguishing excitatory and inhibitory cells, we find a continuous distribution of non-phasic (complex) to phasic (simple) responses in line with receptive field diversity of V1 neurons[48–51]. Analysis of pairwise response correlations revealed the existence of a collective response, which segregates neurons of layer 2/3 and 5, in spite of similar orientation tuning, and involves layer-dependent millisecond spike delays. Given the present proof-of-principle, 3D-CASH acquisition supplies a handle to assess correlations of neuronal activity between 3D-distributed cells, like those of the mammalian columnar cortical circuit, on the true time scale of neuronal electrical activity.

Acknowledgments

We wish to acknowledge expert technical help by Gérard Paresys for electronic designs, Yvon Cabirou for mechanical engineering, El Mehdi Afif for advice on FPGA programming, François Le Fouiller for explanations of acousto-optic device design, the IBENS transgenesis platform and Caroline Maihes-Hamon for help with virus injections, Clara Dussaux (Institut Pasteur, Paris) for spin-coated fluorescent micro-slides, Philippe Rostaing for ultramicrotome sectioning of fluorescent nano-slides, Christophe Auger for help with pharmacology and the IBENS animal facility for animal care. We also want to thank Nathalie Rochefort, Frederic Chavane, Sylvain Gigan and David Ferster for discussions. Funding was provided by ANR (ALPINS ANR-15-CE19-0011-01, ANR-15-CE19-0011-02, EXPECT ANR-17-CE37-0022-01), Région Île de France (DIM Cerveau & Pensée, ALPINS), NIH BRAIN Initiative (1U01NS103464), Fondation pour l'Audition (FPA RD-2018-6), Institut de Convergence Qlife (Q-life ANR-17-CONV-0005) and the program Investissements d'Avenir launched by the French government and implemented by the ANR, with the references: ANR-10-LABX-54 (Memolife), ANR-11-IDEX-0001-02 (Université PSL) and ANR-10-INSB-04- 01 (France-BioImaging Infrastructure). SW was supported by postdoctoral fellowship SPF201809007064 from the Fondation pour la Recherche Médicale France.

Author Contributions

LB, SD and JFL initiated research and obtained funding, WA built the 3DScope, WA and BM coded the software, BM developed the user interface, JF and WA designed the detection unit, AT set up the transmission microscope, JF designed the tower head post, VV set up the treadmill, WA set up the visual stimulator and isoflurane anesthesia, VV and WA performed animal surgery, VV performed virus injections, WA performed experiments, SD and VV performed cell-attached recordings, WA and SW analyzed data and created figures, LB, SD, JFL, CV, VV, SW and WA discussed research, WA, LB, SD and JFL wrote the manuscript with contributions from all authors.

Competing interests

BM and SD are co-founders of the company Karthala System and hold shares in this company.

JFL, LB and SD are inventors in accordance with United States Patents 10423017 and 10191268 jointly owned by the Institut National de la Santé et de la Recherche Médicale (INSERM), the Centre National de la Recherche Scientifique (CNRS) and the École Normale Supérieure de Paris (ENS).

All other authors declare that they do not have competing interests.

Data Availability Statement

Data used for the main figures are available on https://www.opendata.bio.ens.psl.eu/3D-CASH/.

Further data are available from the authors upon request.

Code Availability Statement

Codes for hologram retrieval are available on https://github.com/walther007/3D-CASH. Other codes will be provided by the authors upon request.

References

1. Svoboda, K. & Yasuda, R. Principles of Two-Photon Excitation Microscopy and Its Applications to Neuroscience. *Neuron* **50**, 823–839 (2006).
2. Dombeck, D. A., Khabbaz, A. N., Collman, F., Adelman, T. L. & Tank, D. W. Imaging Large-Scale Neural Activity with Cellular Resolution in Awake, Mobile Mice. *Neuron* **56**, 43–57 (2007).
3. Göbel, W., Kampa, B. M. & Helmchen, F. Imaging cellular network dynamics in three dimensions using fast 3D laser scanning. *Nat. Methods* **4**, 73–79 (2007).
4. Grewe, B. F., Voigt, F. F., van ’t Hoff, M. & Helmchen, F. Fast two-layer two-photon imaging of neuronal cell populations using an electrically tunable lens. *Biomed. Opt. Express* **2**, 2035–2046 (2011).
5. Kong, L. *et al.* Continuous volumetric imaging via an optical phase-locked ultrasound lens. *Nat. Methods* **12**, 759 (2015).
6. Yang, W. *et al.* Simultaneous Multi-plane Imaging of Neural Circuits. *Neuron* **89**, 269–284 (2016).
7. Botcherby, E. J. *et al.* Aberration-free three-dimensional multiphoton imaging of neuronal activity at kHz rates. *Proc. Natl. Acad. Sci.* **109**, 2919 (2012).
8. Liu, R. *et al.* Aberration-free multi-plane imaging of neural activity from the mammalian brain using a fast-switching liquid crystal spatial light modulator. *Biomed. Opt. Express* **10**, 5059–5080 (2019).
9. Quirin, S., Peterka, D. S. & Yuste, R. Instantaneous three-dimensional sensing using spatial light modulator illumination with extended depth of field imaging. *Opt. Express* **21**, 16007–16021 (2013).

10. Ducros, M., Houssen, Y. G., Bradley, J., de Sars, V. & Charpak, S. Encoded multisite two-photon microscopy. *Proc. Natl. Acad. Sci.* **110**, 13138 (2013).

11. Thériault, G., Cottet, M., Castonguay, A., McCarthy, N. & De Koninck, Y. Extended tw-photon microscopy in live samples with Bessel beams: steadier focus, faster volume scans, and simpler stereoscopic imaging. *Front. Cell. Neurosci* (2014).

12. Song, A. *et al.* Volumetric two-photon imaging of neurons using stereoscopy (vTwINS). *Nat. Methods* **14**, 420 (2017).

13. Cheng, A., Gonçalves, J. T., Golshani, P., Arisaka, K. & Portera-Cailliau, C. Simultaneous two-photon calcium imaging at different depths with spatiotemporal multiplexing. *Nat. Methods* **8**, 139 (2011).

14. Picot, A. *et al.* Temperature Rise under Two-Photon Optogenetic Brain Stimulation. *Cell Rep.* **24**, 1243-1253.e5 (2018).

15. Podgorski, K. & Ranganathan, G. Brain heating induced by near-infrared lasers during multiphoton microscopy. *J. Neurophysiol.* **116**, 1012–1023 (2016).

16. Bullen, A., Patel, S. S. & Saggau, P. High-speed, random-access fluorescence microscopy: I. High-resolution optical recording with voltage-sensitive dyes and ion indicators. *Biophys. J.* **73**, 477–491 (1997).

17. Salomé, R. *et al.* Ultrafast random-access scanning in two-photon microscopy using acousto-optic deflectors. *J. Neurosci. Methods* **154**, 161–174 (2006).

18. Reddy, G. D. & Peter Saggau. Fast three-dimensional laser scanning scheme using acousto-optic deflectors. *J. Biomed. Opt.* **10**, 1–10 (2005).

19. Otsu, Y. *et al.* Optical monitoring of neuronal activity at high frame rate with a digital random-access multiphoton (RAMP) microscope. *J. Neurosci. Methods* **173**, 259–270 (2008).

20. Reddy, G., Kelleher, K., Fink, R. & Saggau, P. Three-dimensional random access multiphoton microscopy for functional imaging of neuronal activity. *Nat. Neurosci.* **11**, 713 (2008).

21. Katona, G. *et al.* Fast two-photon in vivo imaging with three-dimensional random-access scanning in large tissue volumes. *Nat. Methods* **9**, 201 (2012).

22. Fernández-Alfonso, T. *et al.* Monitoring synaptic and neuronal activity in 3D with synthetic and genetic indicators using a compact acousto-optic lens two-photon microscope. *J. Neurosci. Methods* **222**, 69–81 (2014).

23. Grewe, B. F., Langer, D., Kasper, H., Kampa, B. M. & Helmchen, F. High-speed in vivo calcium imaging reveals neuronal network activity with near-millisecond precision. *Nat. Methods* **7**, 399 (2010).

24. Szalay, G. *et al.* Fast 3D Imaging of Spine, Dendritic, and Neuronal Assemblies in Behaving Animals. *Neuron* **92**, 723–738 (2016).

25. Griffiths, V. A. *et al.* Real-time 3D movement correction for two-photon imaging in behaving animals. *Nat. Methods* **17**, 741–748 (2020).

26. Akemann, W. *et al.* Fast spatial beam shaping by acousto-optic diffraction for 3D non-linear microscopy. *Opt. Express* **23**, 28191–28205 (2015).

27. Kaplan, A., Friedman, N. & Davidson, N. Acousto-optic lens with very fast focus scanning. *Opt. Lett.* **26**, 1078–1080 (2001).

28. Botcherby, E. J., Juškaitis, R., Booth, M. J. & Wilson, T. An optical technique for remote focusing in microscopy. *Opt. Commun.* **281**, 880–887 (2008).

29. Wyrowski, F. & Bryngdahl, O. Iterative Fourier-transform algorithm applied to computer holography. *J. Opt. Soc. Am. A* **5**, 1058–1065 (1988).

30. Donnert, G., Eggeling, C. & Hell, S. W. Major signal increase in fluorescence microscopy through dark-state relaxation. *Nat. Methods* **4**, 81–86 (2007).

31. Dipoppa, M. *et al.* Vision and Locomotion Shape the Interactions between Neuron Types in Mouse Visual Cortex. *Neuron* **98**, 602-615.e8 (2018).

32. Kerr, J. N. D. *et al.* Spatial Organization of Neuronal Population Responses in Layer 2/3 of Rat Barrel Cortex. *J. Neurosci.* **27**, 13316 (2007).

33. Smith, S. L. & Häusser, M. Parallel processing of visual space by neighboring neurons in mouse visual cortex. *Nat. Neurosci.* **13**, 1144–1149 (2010).

34. Saleem, A. B., Ayaz, A., Jeffery, K. J., Harris, K. D. & Carandini, M. Integration of visual motion and locomotion in mouse visual cortex. *Nat. Neurosci.* **16**, 1864 (2013).

35. Deneux, T. *et al.* Accurate spike estimation from noisy calcium signals for ultrafast three-dimensional imaging of large neuronal populations in vivo. *Nat. Commun.* **7**, 12190 (2016).

36. Chen, T.-W. *et al.* Ultrasensitive fluorescent proteins for imaging neuronal activity. *Nature* **499**, 295 (2013).

37. Niell, C. M. & Stryker, M. P. Modulation of Visual Responses by Behavioral State in Mouse Visual Cortex. *Neuron* **65**, 472–479 (2010).

38. Tubiana, J., Wolf, S., Panier, T. & Debregeas, G. Blind deconvolution for spike inference from fluorescence recordings. *J. Neurosci. Methods* **342**, 108763 (2020).

39. Nadella, K. M. N. S. *et al.* Random-access scanning microscopy for 3D imaging in awake behaving animals. *Nat. Methods* **13**, 1001 (2016).

40. Kirkby, P. A., Srinivas Nadella, K. M. N. & Silver, R. A. A compact acousto-optic lens for 2D and 3D femtosecond based 2-photon microscopy. *Opt. Express* **18**, 13720–13744 (2010).

41. Weisenburger, S. *et al.* Volumetric Ca2+ Imaging in the Mouse Brain Using Hybrid Multiplexed Sculpted Light Microscopy. *Cell* **177**, 1050-1066.e14 (2019).

42. Zhang, T. *et al.* Kilohertz two-photon brain imaging in awake mice. *Nat. Methods* **16**, 1119–1122 (2019).

43. Kazemipour, A. *et al.* Kilohertz frame-rate two-photon tomography. *Nat. Methods* **16**, 778–786 (2019).

44. Wu, J. *et al.* Kilohertz two-photon fluorescence microscopy imaging of neural activity in vivo. *Nat. Methods* **17**, 287–290 (2020).

45. de Vries, S. E. J. *et al.* A large-scale standardized physiological survey reveals functional organization of the mouse visual cortex. *Nat. Neurosci.* **23**, 138–151 (2020).

46. Ohki, K., Chung, S., Ch'ng, Y. H., Kara, P. & Reid, R. C. Functional imaging with cellular resolution reveals precise micro-architecture in visual cortex. *Nature* **433**, 597 (2005).

47. Skottun, B. C. *et al.* Classifying simple and complex cells on the basis of response modulation. *Vision Res.* **31**, 1078–1086 (1991).

48. Yunzab, M., Cloherty, S. L. & Ibbotson, M. R. Comparison of contrast-dependent phase sensitivity in primary visual cortex of mouse, cat and macaque. *NeuroReport* **30**, 960–965 (2019).

49. Niell, C. M. & Stryker, M. P. Highly Selective Receptive Fields in Mouse Visual Cortex. *J. Neurosci.* **28**, 7520 (2008).

50. Chance, F. S., Nelson, S. B. & Abbott, L. F. Complex cells as cortically amplified simple cells. *Nat. Neurosci.* **2**, 277–282 (1999).

51. Bonin, V., Histed, M. H., Yurgenson, S. & Reid, R. C. Local Diversity and Fine-Scale Organization of Receptive Fields in Mouse Visual Cortex. *J. Neurosci.* **31**, 18506 (2011).

Methods

Optical Layout

The 3DScope (Supplementary Fig. 1) was set up on a 250 x 150 cm isolator table (Melles Griot 070T1035). The laser system (Pharos SP6, Light Conversion, Vilnius, Lithuania) consists of a diode-pumped Yb:KGW mode-locked seed oscillator (1028 nm emission, 76 MHz repetition, 90 fs pulse duration, 1 W power), a diode-pumped Yb:KGW chirped-pulse amplifier (80 kHz repetition, 190 fs duration, 75 µJ pulse energy, 6 W power) and an optical parametric amplifier (630-2600 nm tuning range, Orpheus OPA, Light Conversion) delivering 400 mW of signal output (800-1000 nm). Signal and idler beams are separated by a dichroic mirror of 1030 nm cut-off in a double pass configuration at Brewster angle and collimated to a 13 mm beam waist (~$1/e^2$) by 5x (signal) and 2.6x (idler) Galilean telescopes using AR-coated BK7 plano-spherical lenses. The acousto-optic (AO) devices of 15 mm active aperture were custom-made from TeO_2 monocrystals by AA Opto-Electronic (Orsay, France) with a surface cut for autocollimation of the input and coaxial direction of the first-order beam at the acoustic carrier frequency. The cycle time $t_C = d/v$ is 24.6 µs, with d = 16 mm, the crystal diameter, and v = 650 m/s, the velocity for acoustic wave propagation in non-rotated biaxial TeO_2[52]. The AO diffraction efficiency reaches at least 70 % at 36 MHz (800-1000 nm) and 28 MHz (1050-1300 nm) bandwidth through quasi-tangential phase match in anisotropic Bragg diffraction[52]. Two AODs are oriented with their active axis parallel to the horizontal (X-AOD) and vertical (Y-AOD) direction and 4f-conjugated by two achromats (f = 100 mm, d = 30 mm, Thorlabs). An AO modulator (AOM) in 45° orientation is set up to fully compensate the angular dispersion in the AODs at the carrier frequency and partially at side band frequencies[53]. The distance between the AOM and the AODs is adjustable through a two-mirror retro-reflection unit on a motorized translator (150 mm travel, VT-80, PI Instruments) for tuning of temporal dispersion correction[53]. The AODs are conjugated to the optical back aperture (OBA) of the objective (Olympus XLPlan N 25x 1.05 WMP; 8 mm focal length; 15.2 mm OBA diameter) through an achromatic scan lens (f = 300 mm, d = 2”, Thorlabs) and a tube lens (f = 200 mm, d = 36 mm, Nikon MXA 20696), yielding 1.5 angular magnification and 0.66 radial OBA fill factor. The maximum mean power available behind the objective was 25 mW at 940 nm (40 kHz). The microscope head uses the movable objective microscope (MOM; Sutter, Novato, CA) configuration, which permits (x y z)-translations (± 12 mm) and rotation of the objective, and an Olympus BX-RFA epifluorescence unit with a three-color light source (ScopeLED B 190). The detection unit was *de-novo* designed. Using a light diffusion model[54], we derived a 9° half-angle of diffusion-induced spread of emission light at the OBA for an assumed 1 mm thick tissue volume, which defined the collection power of the downstream optics[55] equal to a Helmholtz-Lagrange parameter of 45 mm^2. The detection unit features two detection channels for green and red emission light, a 42 x 35 x 2.5 mm dichroic mirror (Chroma 720dxxr) followed by IR block (d = 40 mm, Chroma ET750sp-1500), a large aperture collimator lens (f = 80 mm, d = 40, Edmund #48-239), a 46 x 34 x 1 mm secondary dichroic mirror (Chroma T562lpxr), emission filters (d = 30 mm, ET520/60 and ET575lp, Chroma), an aspheric condenser lens for each channel (f = 26.5 mm, d = 30 mm, Thorlabs ACL3026A) and two GaAsP hybrid detectors (Hamamatsu R11322U-40). Optical layout was based on ray optics using transfer matrices with subsequent refinement by ray tracing (OpticStudio; Zemax). The microscope, excluding the wide-field imaging path, was coded in Rhinoceros 5 (McNeel) using component CAD files from Thorlabs, Newport, Linos, Turbo Squid, Light Conversion and AA Optoelectronic.

Electronic layout

In Bragg diffraction, the diffraction angle of the first order beam, Θ, is given by $\Theta = \lambda f/v$, with λ, the optical wavelength in air, f, the acoustic carrier frequency, and v, the acoustic velocity in TeO_2. To preserve this angle between different wavelengths of excitation, our design keeps λf constant by adapting the carrier frequency according to $f_{AOD}(\lambda) = 81\,MHz \cdot 1000\,nm/\lambda$ and $f_{AOM}(\lambda) = \sqrt{2} \cdot f_{AOD}(\lambda)$. While the AOM operates at constant RF frequency (MDS1, AA Opto-Electronic), the AODs operate on the basis of real-time RF frequency and power update in time-locked FM/AM mode using fast-switching direct digital synthesizer (DDS) circuits with 2.5 W power amplifiers (DDSPA, AA Opto-Electronic). A synchronisation signal is generated with a Schmitt trigger (74VHC123A, Fairchild Semiconductors) from the output of a fast photodiode at the exit of the Pharos pulse compressor by picking every second pulse from the initial 80 kHz laser output. This timing signal (Laser SYNC) then triggers two clock signals on a timer counter board (14 MHz, 345 cycle; NI PXIe-6612, National Instruments) to clock the real-time data transfer between digital I/O channels (50 MHz; NI PXIe 6537, National Instruments) as the sender and the AOD DDS boards (23 bit frequency resolution, 8 bit power resolution, 64 ns sweeping time) as receivers. The FM/AM data are calculated on the host computer for every laser pulse and streamed with forerun to the output devices through first-in-first-out (FIFO) memory stacks using direct memory access (DMA). Data acquisition is gated by the laser SYNC to reject detector dark noise during 25 μs inter-pulse intervals. As the expected photon flux amounts to several 100 emitted photons per laser pulse, and because the R11322U-40 photomultiplier has a picosecond response time, 0.45 quantum efficiency and up to 2x10^5 gain, the expected detector signal is a 3 ns anode current pulse of the order of 200 μA, or 10 mV at 50 Ω, when assuming a 3 ns excited state decay time of EGFP[56]. The detection chain consists of a 200 MHz RC filter, a programmable low noise voltage amplifier (DHPVA, Femto, Berlin, Germany) and a two-channel 800 MHz AC analog-to-digital converter (ADC) with ± 1 V input range at 12 bit resolution (NI-5772, FLEX-RIO, National Instruments) in combination with a 50,950 slice field-programmable gate array (FPGA) (NI PXIe 7971R, National Instruments). While the ADC runs continuously, the FPGA circuit was set up to pick the wanted data from the data stream and send them to the host. For this, the circuit runs a 200 MHz loop in phase with the 800 MHz converter clock to read the ADC data (4 data words per cycle and channel) and keeps them in a circular buffer. Once the laser SYNC trigger is received, pre-trigger samples (195 ns pretrigger) of fixed length (75 ns gate window), to account for the delay of the SYNC signal relative to the laser pulse, are retrieved from the buffer, summed and written to output FIFOs. The amplifier gain (10 to 100) was adapted to match the ± 1 V ADC input range. The anode output of the R11322U-40 was a linear function of the input light up to 10 μA mean and 30 mA peak anode current (measured with 200 MHz bandwidth). Low-incidence (< 0.001 per sample) detector popcorn noise, possibly by bremsstrahlung-induced spurious photoelectron emission, was removed in post-processing by outlier filtering with negligible loss of information. The software operating the 3DScope was coded in LabVIEW 2015 (National Instruments). The FPGA circuit was created with the Vivado 2014.4 compiler (Xilinx) under NI RIO 17.0 (National Instruments).

Iterative Fourier-Transform Algorithm

In complex notation, the light electrical field is given by $A(x, y)\ e^{i\varphi(x,y)}$, with A, the amplitude, and φ, the phase. In the iterative Fourier-Transform algorithm (Gerchberg-Saxton) the electric field is transformed between the holographic plane (the back focal plane of the microscope objective) and the Fourier plane (the front focal plane,) by forward and inverse Fourier transforms under the constraint of a fixed constant amplitude in the holographic plane and the wanted target amplitude distribution in the Fourier plane (Fig. 2a). Since the hologram needs to be separable along the x- and y-coordinates[57], $A(x,y) = A_x(x) \cdot A_y(y)$ and $\varphi(x,y) = \varphi_x(x) + \varphi_y(y)$, we performed independent searches for 1D holograms on the two axes using a 10,000 point discretization grid of 30 mm length. The search loop was initiated in the Fourier plane with a random phase. We then recovered the 2D hologram by combining the two solutions in x-y coordinate space and reconstructed the intensity distribution in Fourier space which included a non-linear propagator to obtain the light field outside of the Fourier plane. However, valid holograms are not univocally defined by the target intensity distribution in the focal plane. By looping through a number of searches (~10), we selected for low FM and AM bandwidths to maximize the remaining modulation bandwidth and power transmission of the system, respectively. As a consequence of AM modulation, the transmission dropped by 45 %, 65 % and 65 % in AM/FM versus FM only mode for 3x3, 5x5 and 2x5 spot grids, respectively. In about a third of the experiments AM modulation was prohibited because of insufficient laser power. In this case we used the FM-only mode with a modified target pattern which included side lobes up to 5th order with up to 30 % primary target spot intensity to achieve homogeneous intensity in primary target spots comparable to the FM/AM mode. Finally, the RF signal to drive the AODs is obtained as the derivative of the unwrapped holographic phase in x- and y-direction[57].

Point-Spread-Function Measurement

We used a custom-made transmission microscope to directly image the intensity distribution in the focal plane from a thin fluorescent layer in the xy plane (Fig. 2c) through a high NA objective (LEICA HC PL APO 40x/1.1 W) used with synthetic water immersion fluid (ZEISS Immersol W). Samples were a fluorescein-doped spin-coated PMMA layer, a nano-plastic slide[58] and a bulk layer of aqueous fluorescein (20 mM) of 10-20 μm thickness under a cover slip. While the nano-slide was the only sample to provide a sub-resolution nominal thickness (500 nm), the axial FWHMs of the measured PSF (0.25 μm z-steps) were consistent among the three samples (Supplementary Fig. 3b), presumably because of the large NA difference of focusing and imaging objective.

Cell Motion Measurements

To estimate x,y movements of brain cells during mouse behavior under our experimental conditions we recorded time-lapse movies of EGFP-expressing neurons at 6-16 Hz frame rate and registered the frames using NoRMCorre[59] which yielded cell displacements Δx, Δy with respect to a fixed reference frame. For estimating axial movement, we additionally recorded a reference z-stack of the same cell at 0.25 μm axial resolution, but with the animal held under isoflurane anesthesia to suppress cell movement. In this case we used the focal image frame of the z-stack as registration reference for the t-stack and calculated the correlation coefficients between all t- and z-frames. For each t-frame a Δz-displacement is estimated as the z-position of the z-frame yielding maximal correlation.

Visual Stimulation

Visual stimulus movies were generated in Matlab (R2013b, Mathworks) as a 8 bit gray scale image stack at 500 x 400 pixel resolution. During run time, images were resized to 1280 x 1024 screen resolution of a 17” LED back-illuminated computer monitor (Dell E1715S) and played at 30 Hz in sync with the vertical display retrace clock of the monitor using synchronization tools from the Psychtoolbox (PTB-3) for Matlab. In addition, the screen back-illumination was gated at 40 kHz under control of the laser SYNC such that the screen was off during a 20 μs time window which included the acquisition gate (see Supplementary Fig. 11a). The screen was placed at ~12 cm distance from the left eye of the animal such that the eye axis was approximately normal and central to the screen covering a 110^o (h) x 100^o (v) lateral eye field. We used three stimulus movies. A noise movie, shown to the animal during image stack acquisition, was created by inverse Fourier transformation of a random spatial-temporal frequency spectrum subject to a temporal cutoff of 4 cycles per second (cps) and a 1/f spatial frequency envelope with half maximum value of 0.04 cycles per degree (cpd) and 0.15 cpd cutoff[60]. The second movie was composed of a sequence of moving sinusoidal gratings with different orientations and fixed temporal (2 cps) and spatial frequency (0.04 cpd) at high contrast (0.8). Each grating was shown for 3 s followed by 7 s of gray screen. Stimulus sequences were repeated in following trails after a 30 s pause showing a black screen and in each case started with 10 s of gray screen. The third movie showed sinusoidal gratings in pairs of 0^o and 90^o orientation with each pair given another temporal frequency between 0.5 and 4 cps, at constant 0.04 cpd. The movies were shown on a gray background within a circular field of 75^o centered to a position on the screen which elicited largest activation of cells within the imaged brain region (~250 x 250 μm^2). Stimulus on- and offset-times were annotated by logging the CPU time and by recording the signal of a photodiode placed at the right lower corner of the screen to record the contrast switch upon stimulus on- and offset. The photodiode signal was acquired at 5 kHz on a PCIe-6351 ADC board (National Instruments) using the microscope acquisition flag as a start trigger.

Animal Welfare

Experimental procedures were conducted in compliance with French and European laws, including the "European Convention for the Protection of Vertebrate Animals used for Experimental and other Scientific Purposes" (ETS 123), and following INSERM and NIH institutional guidelines. All procedures were approved by the "Charles Darwin"-Ethics Committee of École Normale Supérieure under project number 04828.02 and 12007.

Surgical Procedures

This work includes data from five female heterozygous pGAD65-EGFP[61] mice (C57BL/6 background), aged 7-9 months, and 12 wild-type male C57BL/6 mice (Janvier Labs, France), aged 3-6 months (ventilated home cage; 23 ± 1° C; 50 ± 5 % humidity; 12 h light/dark). The animals received surgery for implantation of an optical cranial window. The skin over the cranial bone was incised along the midline and retracted to both sides. The bone was treated with hydrogen peroxide solution and adhesion primers (Optibond, Kerr), before a 6 mm craniotomy of the parietal bone was performed over primary visual cortex of the right hemisphere at -2.8 mm antero-posterior and 2.5 mm medio-lateral of Bregma. In the case of the wild-type mice, 0.5 μL virus solution was injected (Legato 130, KD Scientific) at 0.1 μL/min under stereotaxic control (# 942, Knopf) 300 μm below the pia mater using quartz electrodes (~20 μm tip size) with a 10 μL Hamilton syringe. Per animal, up to 3 injections were done with lateral offsets of 200 to 500 μm. Solutions were made up of AAV2/1-pSyn(h)-Cre-WPRE-GH ($1.9 \cdot 10^{13}$ GC/mL; 1:1000) and AAV2/1-pSyn(h)-FLEX-GCaMP6f-WPRE-SV40 ($1.4 \cdot 10^{13}$ GC/mL; 1:30) using a Ringer base solution. In two mice, AAV2/1-pCAG-FLEX-tdTomato-WPRE-SV40 ($8.52 \cdot 10^{12}$ GC/mL 1:150) was added as a third virus. All viruses were supplied by the Vector Core Facility of the University of Pennsylvania (Penn Vector Core, USA). Finally, the craniotomy was covered with a 5 mm BK cover glass (0.15 mm thickness; Warner Instruments) and sealed with UV-curable dental cement (Tetric Evoflow, Ivoclar Vivadent). In the last step, a headpost was fixed to the skull with dental cement. The headpost was either an inox plate or a titan-printed tower (Fig. 3a), both providing comparable mechanical rigidness. Virus-injected mice were used for experiments during a time window of 1 to 4 weeks after injection.

Additional procedures for in-vivo electrophysiology

A total of seventeen 2-4 weeks old C57BL/6 mice (both genders; Charles River) were prepared for simultaneous optical and cell-attached (loose patch) electrophysiological recordings. At P17-30 a small injection craniotomy was performed over visual cortex and 250 nL of a virus mixture of AAV2/1-pSyn(h)-Cre-WPRE-GH ($1{\cdot}10^{10}$ GC/mL) and AAV2/1-pSyn(h)-FLEX-GCaMP6f-WPRE-SV40 ($2{\cdot}10^{12}$ GC/mL) was injected at 75 nL/min with an angle of 64^{o} against the normal at 2.8 mm posterior and 2.7 mm lateral of Bregma in the right hemisphere. After 1-2 weeks, the bone was thinned over the injection site and a head plate was cemented to the skull. Under wide field excitation, the site of GCaMP6f expression was determined and a craniotomy of approximately 0,7 x 1 mm was performed over the indicated region, followed by a small durectomy about 450 µm lateral of the intended recording site. Under the 3DScope, anesthetized mice (1.65 g/kg urethane in 0.9 % NaCl i.p.) were kept on a heating pad under continuous monitoring of the breathing rhythm. A 5-15 MOhm borosilicate patch pipette filled with artificial cerebral spinal fluid (ACSF) solution (in mM: 140 NaCL, 2.5 KCl, 1.5 $CaCl_2$, 1.5 $MgCl_2$, 30 Hepes, pH 7.3 with NaOH, 0.1 Alexa 954 hydrazide) and a supplement to increase cell firing during membrane approach (3.5 mM potassium gluconate or 20 nM kainaite) was lowered into the durectomized area and slowly advanced towards the target region (PatchStar Micromanipulator, Scientifica) under an angle of ~70^{o} versus normal at positive electrode pressure. During experiments, the craniotomy was superfused with HEPES-buffered ACSF of 34^{o}C at 2 ml/min using a peristaltic pump (IPC, Ismatec) with an in-line solution heater (SF-28, Warner). Membrane sealing was helped by hyperpolarizing the electrode to -70 to -40 mV in voltage-clamp mode (MultiCamp 700 B, Molecular Devices). A frame sync signal was recorded together with the electrode current (20 kHz; Digidata 1440 A, Molecular Devices) for post-alignment of optical and electrophysiological recordings.

Experimental Protocol

Four days before start of recording sessions novice mice were accustomed to human handling, head fixation and walking on a treadmill. The custom-made treadmill[62] featured a PLA-printed outward treadmill of 7.7 cm diameter with grip bars fitting the size of the mouse paw, side barriers to safeguard the animal on the track and an optoelectronic rotation decoder to report the walking distance (HEDS-5645#A06, Broadcom). The decoder signal (two phase-shifted pulse trains of 500 counts per rotation (cpr) and 1 cpr, respectively) were digitized at 10 kHz on a USB-ADC unit (USB-6259 BNC, National Instruments) and decoded for locomotion direction and speed by a custom virtual instrument in LabVIEW 2017. In 21 experiments, we anesthetized the animal under head clamp with a custom-designed anesthesia mask effusing 3 % isoflurane with 20 % O_2 and 80 % N_2O (1 L/min). Following induction, we reduced to 1.2 to 1.5 % isoflurane, installed a heat pad for homeothermic control to 37^{o}C (H-800156, Harvard

Instruments) and began monitoring the respiration rate using a piezoelectric diaphragm (7BB-20-6, Murata). After administration of a sedative (Astenodex, 0.1 mL/kg i.p.) isoflurane was further reduced to 0.25 to 0.5 %. At this stage, the respiratory rhythm was low (1-2 beats/s), vibrissae were inactive, the animal was not reacting to whisker touch or body squeezes, but would weakly react to strong paw pinches. This condition was stable for at least one hour. For longer recordings, a second Astenodex dose was given. Experimental sessions were limited to a maximum of two hours.

Data Acquisition

Image stacks were acquired at 300 x 300 pixel resolution at 2 to 2.5 μm z-steps and using one laser pulse per pixel resulting in 2.25 frames/s acquisition speed. Every stack extended 200 μm above and below the focal plane which was set at 300 to 380 μm below the pia mater in layer 4. From these stacks, cell bodies were manually selected as POIs using custom tools in the 3DScope GUI to add the (xyz) center coordinates to a job list for the scan engine together with the laser power and hologram to be applied, making these parameters freely eligible for every POI and laser pulse. In this work we used point grids (5x5 and 2x5) for all POIs, but adapted the size depending on laminar position of target cells in layer 2/3, 16x16 μm^2 (5x5) and 24x24μm^2 (2x5), or layer 5, 18x18 μm^2 (5x5) and 28x28 μm^2 (2x5). The laser power was adapted assuming a scattering length of 200 μm. After every experiment performed in the CASH mode, we verified the cell coordinates by acquiring micro-frame images of 25x25 pixel size centered at the programmed cell coordinates. In cases where we found a drift, we discarded the CASH data and repeated the measurement. All GCaMP6f recordings were using 940 nm excitation.

Data Analysis

Fluorescence traces were normalized by the median using a running window of 50 s and detector popcorn noise was removed with a three-point Hampel filter. Our infection protocol yielded expression in neurons of layer 2/3 and layer 5 close to the injection site whereas neurons in intermediate layer 4 were generally not infected. Our assignment of neurons to layer 2/3 or 5 was therefore unambiguous in most cases. However, in a few cases, GCaMP6f-expressing cell bodies were found in positions that seemed to belong to the granular rather than the supra-granular layer. In our assignment we did not distinguish these cells and labeled them layer 2/3 throughout. For evaluating the effect of locomotion on GCaMP6f visual responses we determined the maximum velocity of the animal during a time window starting

6 s before presentation of the stimulus onset and ending at stimulus offset (3 s after stimulus onset). This ad-hoc choice was motivated by the observation that locomotion episodes often lasted longer than the stimulus (3s) and that the effect of neuromodulation may last over several seconds[63]. In case of EGFP signal-to-noise (SNR) was calculated as $SNR \coloneqq \langle F\rangle / SD(F)$ and in case of GCaMP6f as $SNR{:} = S_{peak}/SD_{baseline}$ with S_{peak}, the peak response amplitude, and $SD_{baseline}$, the standard deviation of the baseline defined as width of the negative tail of the ΔF/F trace histogram or, alternatively, as the standard deviation of the ΔF/F trace after high-pass filtering with 4 Hz cutoff. Central tendency and spread of measured data are given as mean ± SD, unless stated otherwise. Sampling rates are given in Hertz or, for avoidance of ambiguity, in kilo samples per second (kS/s).

Neuropil Correction

Corrections for neuropil activity were obtained by subtracting the neuropil traces (NP) from the traces obtained from the cell body (CB) using a global weight factor alpha, $[\Delta F/F](t;\alpha) = [\Delta F/F]_{CB} - \alpha\, [\Delta F/F]_{NP}$. We used two different algorithms to determine the α parameter. In noise regression, we minimized the width of the negative tail of the trace histogram, departing from the idea that low frequency baseline fluctuation is a consequence of population calcium activity as reported in $[\Delta F/F]_{NP}$, thus $\alpha = argmin\{SD(\Delta F/F\,(t;\alpha) \leq 0)\}$. Alternatively, we performed correlation regression seeking to decorrelate the baselines of the cellular and the neuropil traces, e.g. $\alpha = argmin\{corr(\Delta F/F\,(t;\alpha) \leq 0, [\Delta F/F]_{NP}(t) \leq 0)\}$. In this case, we obtained the alpha value as the slope of a linear fit to $[\Delta F/F(t)]_{NP}$ and $[\Delta F/F(t)]_{CB}$ data pairs presented as xy-plot (Supplementary Fig. 7c). To exclude the contribution of neuronal activity, we divided the $[\Delta F/F]_{CB}$ axis into 50 bins and included into the fit only those pairs with $[\Delta F/F]_{CB}$ values smaller or equal to the 10 %-tile of $[\Delta F/F]_{CB}$ in every bin. Corrected traces were smoothened with a three-point running average filter.

Deconvolution of GCaMP6f recordings

For MLspike event detection, we used as template for the GCaMP6f response: τ_{on} (50 ms), τ_{off} (300 ms), ΔF/F amplitude (0.075) for a single spike and a hill coefficient (1.7) based on data given in[36], together with maximal baseline drift (0.02/s). For the analysis of the dataset with synchronous membrane current recording the template was updated to:

τ_{on} (90 ms), τ_{off} (370 ms), ΔF/F amplitude (0.075) for a single spike and a hill coefficient (1.7).

Spike-triggered average GCaMP6f waveforms were fitted with a bi-exponential response function $f\left(t; a, b, \tau_{on}, \tau_{off}\right) := b + a \cdot \left(1 - exp\left[-\left(t - t_{spike}\right)/\tau_{on}\right]\right) \cdot exp\left[-\left(t - t_{spike}\right)/\tau_{off}\right]$, with τ_{on}, τ_{off}, the rise and decay time constants of the GCaMP6f response, respectively, and t_{spike}, the MLspike-inferred spike time.

Visual Stimulus Response

For neuron response to a contrast-grating stimulus, we defined the fluorescence stimulus response $r_F(\Theta) := 1/n \sum_{i=1}^{n} [\Delta F/F]\,(i; \Theta)$ with n, the number of samples from onset to offset of the stimulus, and Θ, the stimulus orientation. We judged a response significant (ΔF/F+), if among all orientations of a given grating the mean response to at least one orientation surpassed three times the baseline noise given by the standard error of the mean (SEM) of the signal during a 3s pre-stimulus period. For (ΔF/F+) neurons, we calculated the global orientation selectivity index, gOSI, as vector sum of the responses over all orientations: $gOSI := \sum_\Theta r_F(\Theta)\, e^{i2\Theta} / \sum_\Theta r_F(\Theta)$. Likewise, the global direction selectivity index: $gDSI := \sum_\Theta r_F(\Theta)\, e^{i\Theta} / \sum_\Theta r_F(\Theta)$. To judge statistical significance of orientation selectivity, we calculated gOSI from bootstrap data by drawing bootstrap responses for every orientation of the grating by random selection with replacement from the set of responses of the same neuron across all orientations and stimulus repetitions. We then evaluated the SD of |gOSI| from 10^4 bootstraps as an estimate of |gOSI| variance of isotropic responses and defined orientation-selective neurons (OS+) as neurons with |gOSI| equal or larger than two times the SD of the index in the isotropic case. For (OS+) neurons, we evaluated the preferred orientation as $\Theta_{Pref} = 0.5 \cdot atan(Im(gOSI)/Re(gOSI))$ and the specific orientation selectivity index $OSI(\Theta) := [r_F(\Theta) - r_\perp(\Theta)]/[r_F(\Theta) + r_\perp(\Theta)]$ with $r_\perp(\Theta)$, the mean response to orientations orthogonal to Θ. From OSI we obtained a second estimate for the preferred orientation by global fit to a biphasic von Mises function $OSI_{fit}\left(\Theta; \theta_{pref}, c_1, c_2, c_3\right) = c_1 \cdot e^{\left(cos\left(\Theta - \Theta_{Pref}\right) - 1\right)/c_2} + c_3 \cdot e^{\left(cos\left(\Theta - \Theta_{Pref} + 180^o\right) - 1\right)/c_2}$. The R_1/R_0 ratio was calculated from R_1, the peak-to-peak amplitude of the Fourier component at stimulus frequency, ν_{Stim}, of the spike PSTH $R_1 := 2 \cdot \sum_{\nu_{Stim} - 0.5Hz}^{\nu_{Stim} + 0.5Hz} [FFT\{PSTH(R; \Delta t)\}(\nu)]$, with R, the spike rate, and Δt, the binning width (80 ms) and the mean spike rate $R_0 := mean\{PSTH(R; \Delta t)\}$. We determined R_1/R_0 separately for the forward and counterpropagating stimulus of preferred orientation to identify the larger of the two.

Evaluation of Spike Detection Error

To simulate a fluorescence signal $F(t)$, we generated poisson trains of spikes $N(t)$ at a firing rate of 0.2 Hz, we sampled the signal at 250 Hz, convolved it with a kernel modeling GCaMP6f kinetics $K(\tau) \coloneqq exp(-\tau/\tau_{decay})(1 - exp(-\tau/\tau_{rise}))$ with a rising time (τ_{rise}) and decay time (τ_{decay}) of, respectively, 100 ms and 300 ms, and added Gaussian photonic noise $\epsilon(t)$. In order to model the neuropil component, we added a neuropil signal $FNP(t)$ extracted from the experiments, to obtain the the simulated fluorescence $F(t) = \int K(\tau)N(t-\tau)d\tau + \epsilon(t) + FNP(t)$. To probe the neuropil correction estimator, we first corrected $F(t)$ using noise regression or correlation regression and inferred spike trains from the corrected fluorescence signal using MLspike and BSD. Spikes were considered as detected, if they were found in a fixed incidence time window of either 12 or 20 ms around the true spike. The estimation accuracy was quantified by the error rate (*ER*), the complement of the F-score: $ER = 1 - 2 \cdot Sensitivity * precision/(Sensitivity + Precision)$, with sensitivity and precision defined as:

$\text{sensitivity} = (\text{number of detected true spikes})/(\text{total number of true spikes})$

and $\text{precision} = (\text{number of detected true spikes})/(\text{total number of detected spikes})$.

ER, sensitivity and precision were evaluated for SNRs from 2 to 5 from 600 spikes in simulated trials of 3000 s duration.

Correlation analysis

To characterize the structure of pairwise neuronal correlation, we performed principal component analysis (PCA) on the Pearson correlation matrix calculated from GCaMP6f traces. For each data set, the first three eigen vectors (principal components, PCs), sorted by their eigenvalues, were kept for explanation of largest variance. For these three PCs, we extracted the weights of individual cells and correlated the weights of all cells with their z-position obtained from the imaging stack. Among the three highest PCs we identified for each dataset the PC that showed the highest correlation of weight and z-position. To analyze synchronicity, we computed the cross-correlation of ΔF/F traces between all cells and extracted the time lag from -500 to 500 ms yielding the highest correlation coefficient. From these data we calculated the histograms of the maximal time lags for cell pairs within layer 2/3, within layer 5 and across the two layers. We used the widths of these distributions, given by their standard deviation, δt, as a measure of synchronicity among cells in each group.

Spike propagation analysis

We reconstructed spike trains from the GCaMP6f traces using blind sparse deconvolution (BSD). For every neuron i and every emitted spike s at time $t_{i,s}$ we searched for all neurons j the spike s' such that $t_{j,s'} - t_{i,s}$ is minimal with $d_{i,j,s} := \min_{s'}\left(t_{js'} - t_{i,s} > 0\right)$, the corresponding time delay, see Fig. 6n. To distinguish intra- and inter-laminar temporal spike order, we computed N_i^j, the number of spikes emitted by neuron i having a closest follower spike in a neuron j, $n_k^l := \sum_{i \in L_k} \sum_{j \in L_l} N_i^j$, the number of spikes emitted by neurons in layer k having first follower spikes in layer l, and $n_k^T := \sum_l n_k^l$, the total number of spikes emitted by neurons in layer k, with L_k, the subset of cells in layer k, k = [2/3,5]. From these numbers we calculated $p_k^l := n_k^l / n_k^T$, the probability of a spike emitted by a neuron in layer k having a first follower spike in layer l (Supplementary Fig. 11b). We also calculated the normalized probabilities $\hat{p}_k^l := p_k^l / (f_l \cdot N_l)$, the probabilities p_k^l divided by the number of cells in the follower layer l, N_l, and the mean spike rate, f_l, in the follower layer l (Fig. 6o). Data analysis was performed in Matlab R2019b (Mathworks).

References Methods

52. Xu, J. & Stroud, R. *Acousto-Optic Devices*. (John Wiley, 1992).
53. Kremer, Y. *et al.* A spatio-temporally compensated acousto-optic scanner for two-photon microscopy providing large field of view. *Opt. Express* **16**, 10066–10076 (2008).
54. Beaurepaire, E. & Mertz, J. Epifluorescence collection in two-photon microscopy. *Appl. Opt.* **41**, 5376–5382 (2002).
55. Oheim, M., Beaurepaire, E., Chaigneau, E., Mertz, J. & Charpak, S. Two-photon microscopy in brain tissue: parameters influencing the imaging depth. *J. Neurosci. Methods* **111**, 29–37 (2001).
56. Striker, G., Subramaniam, V., Seidel, C. A. M. & Volkmer, A. Photochromicity and Fluorescence Lifetimes of Green Fluorescent Protein. *J. Phys. Chem. B* **103**, 8612–8617 (1999).
57. Akemann, W. *et al.* Fast spatial beam shaping by acousto-optic diffraction for 3D non-linear microscopy. *Opt. Express* **23**, 28191–28205 (2015).
58. Antonini, A., Liberale, C. & Fellin, T. Fluorescent layers for characterization of sectioning microscopy with coverslip-uncorrected and water immersion objectives. *Opt. Express* **22**, 14293–14304 (2014).

59. Pnevmatikakis, E. A. & Giovannucci, A. NoRMCorre: An online algorithm for piecewise rigid motion correction of calcium imaging data. *J. Neurosci. Methods* **291**, 83–94 (2017).

60. Niell, C. M. & Stryker, M. P. Highly Selective Receptive Fields in Mouse Visual Cortex. *J. Neurosci.* **28**, 7520 (2008).

61. Erdélyi, F. *et al.* Preferential Origin and Layer Destination of GAD65-GFP Cortical Interneurons. *Cereb. Cortex* **14**, 1122–1133 (2004).

62. Villette, V., Levesque, M., Miled, A., Gosselin, B. & Topolnik, L. Simple platform for chronic imaging of hippocampal activity during spontaneous behaviour in an awake mouse. *Sci. Rep.* **7**, 43388 (2017).

63. Reimer, J. *et al.* Pupil fluctuations track rapid changes in adrenergic and cholinergic activity in cortex. *Nat. Commun.* **7**, 13289 (2016).

Extended Data Figures

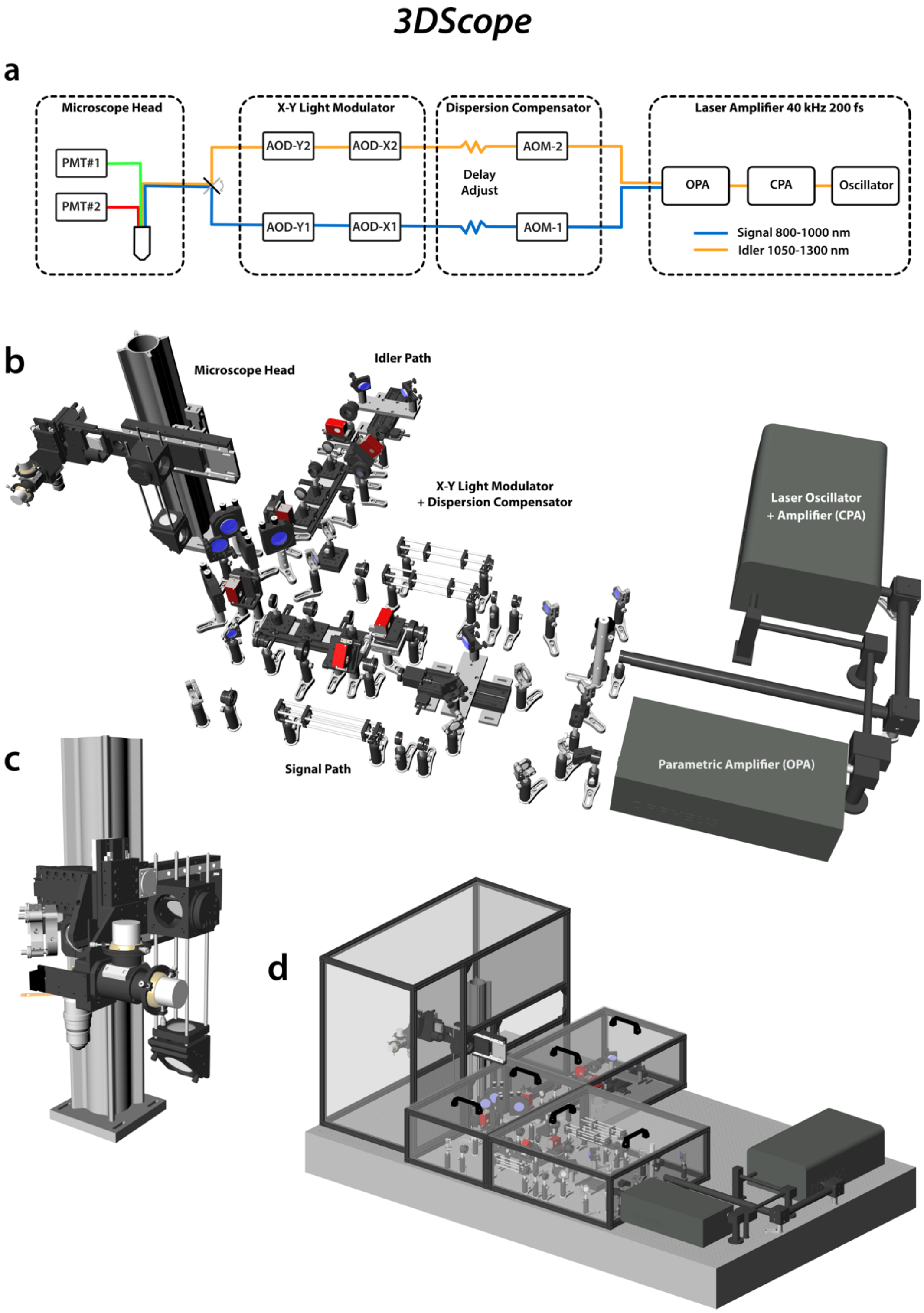

Extended Data Fig. 1 Optical hardware (3DScope)
a) Schematic representation of the active components in the signal and idler paths of the microscope (PMT: photomultiplier tube detector; AOD: acousto-optic deflector; AOM: acousto-optic modulator; OPA: optical parametric amplifier; CPA: chirped pulse amplifier). **(b-d)** 3D-rendered views of the microscope. **(b)** Top view without table and safety walls. **(c)** Microscope head with XYZ-movable objective (modified Movable Objective Microscope, MOM, Sutter Instruments) with added 2” periscope and custom-designed relay optics and detection unit. **(d)** Complete view with transparent safety walls for the purpose of visualization.

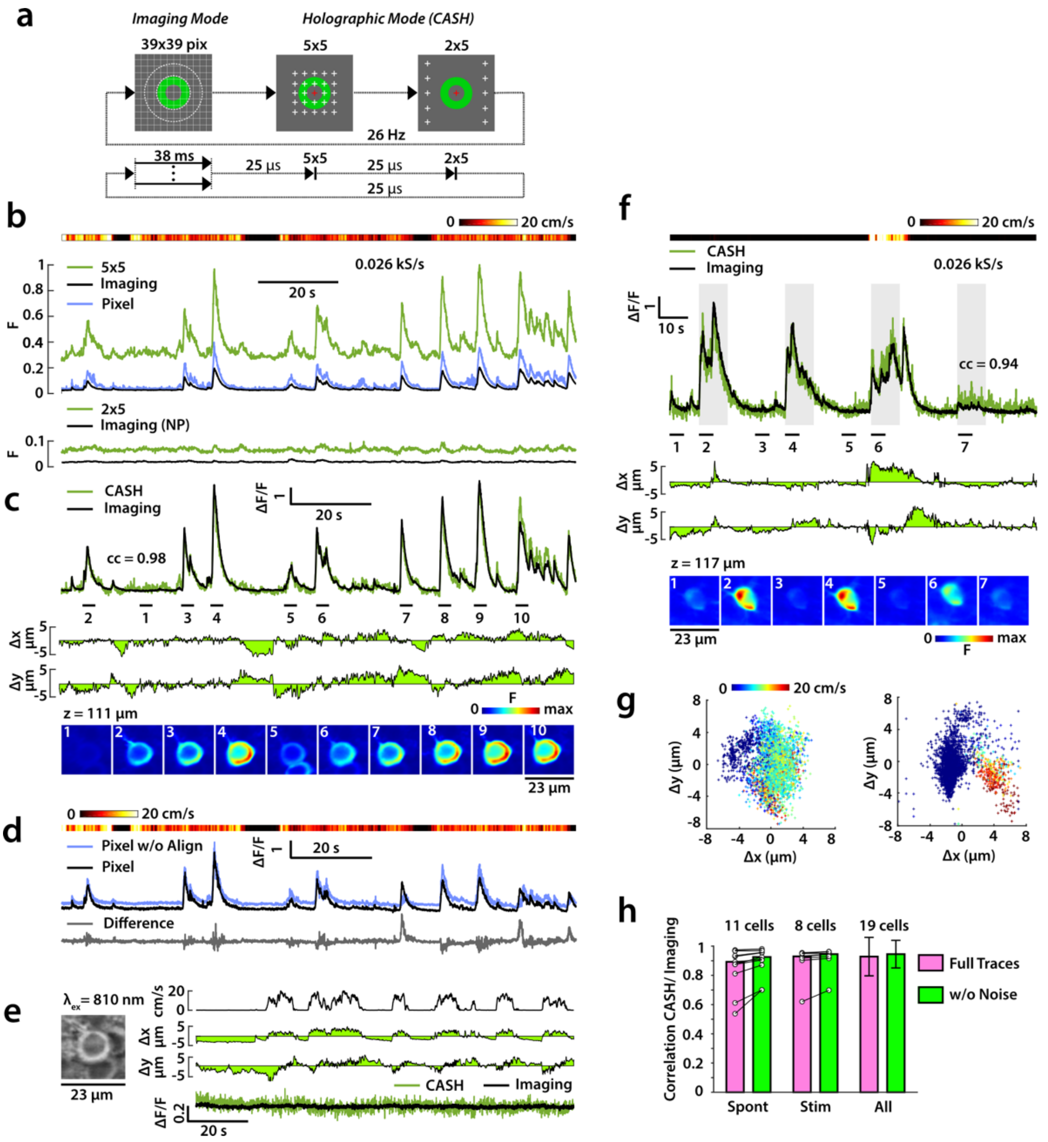

Extended Data Fig. 2 Simultaneous CASH and image-scan recording

(a) Experimental design: A single GCaMP6f-expressing cell is targeted first with a cell-centered image scan (39x39 pixels, 38 ms scan time) followed by a two-shot CASH acquisition (50 µs) resulting in 26 Hz loop rate. **(b)** Example recording (130 s) of spontaneous activity showing (*top to bottom*) the motion of the animal, absolute fluorescence signal obtained from 5x5 CASH (green), imaging (black; pixel mean after image stack alignment), the brightest pixel of the aligned image stack (blue), the 2x5 CASH signal (green) and the imaging-derived neuropil signal (black; pixel mean across a concentric region around the cell body). **(c)** *Top*: Overlay of ΔF/F fluorescence traces after neuropil (NP) correction and normalization minimizing the global mean squared difference. The alignment yields 0.98 coefficient of correlation (cc). *Middle:* amplitudes of cell motion in x and y direction from alignment of image frames. *Bottom:* fluorescence images of the targeted cell at different instants as marked above (black lines). **(d)** Overlay of the single pixel trace before (blue) and after (black) x,y-alignment of the time lapse image sequence. **(e)** Overlay of a CASH (green) and imaging (black; same cell as above), but with 810 nm excitation for Ca^{2+}-independent fluorescence (*bottom*), with x,y cell motion (*middle*) and running speed of the animal (*top*). **(f)** *Top*: overlay of single-trial CASH (green) and imaging (black) recordings (different cell) during presentation of a visual noise stimulus (gray bars) yielding 0.94 correlation. *Middle:* x,y cell motions. *Bottom:* Snapshot fluorescence images of the cell at instants indicated by bars above (black). **(g)** 2D representation of x,y cell motion during recordings in (b; *left*) and (f; right) with moving speed of the animal in false color. **(h)** Coefficient of correlation of GCaMP6f traces of simultaneous CASH and imaging recordings, analogous to (b) and (f), for all recorded cells (violet bars; median) and of the same traces after removal of photon noise by MLspike deconvolution fit (green bars; median). The number of observed cells are indicated above. Error bars represent SD.

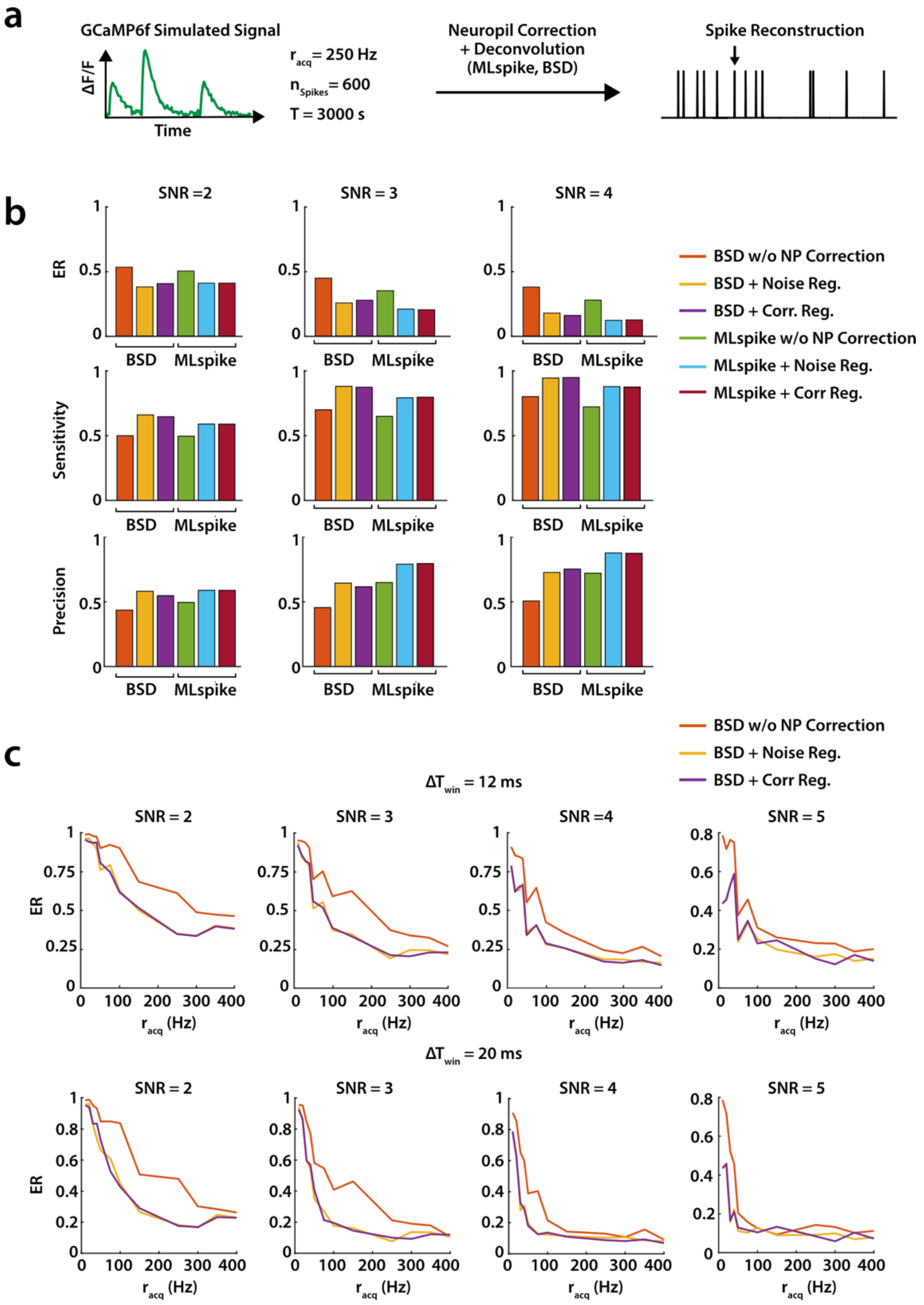

Extended Data Fig. 3 Event Detection accuracy evaluated on simulated data

a) Workflow schematic: We generated GCaMP6f-like neural calcium activity ($r_{acq} = 250\ Hz$, 600 spikes, mean firing rate 0.2 Hz, 3000 s) contaminated with a neuropil signal. After neuropil correction, we deconvoluted the data and from inferred spikes evaluated the error rate (ER), the sensitivity and the precision of inference. **(b)** Error rates for artificial data (SNR 2, 3 and 4) according to neuropil correction (noise- or correlation regression) and inference algorithm (MLspike and BSD). **(c)** Error rate as function of acquisition rate, r_{acq}, for data with SNR between two and five obtained with the BSD algorithm for two window sizes ΔT_{win} (12 and 20 ms). A spike is rated as detected, if the spike falls within this time window centered around the time of the true spike.

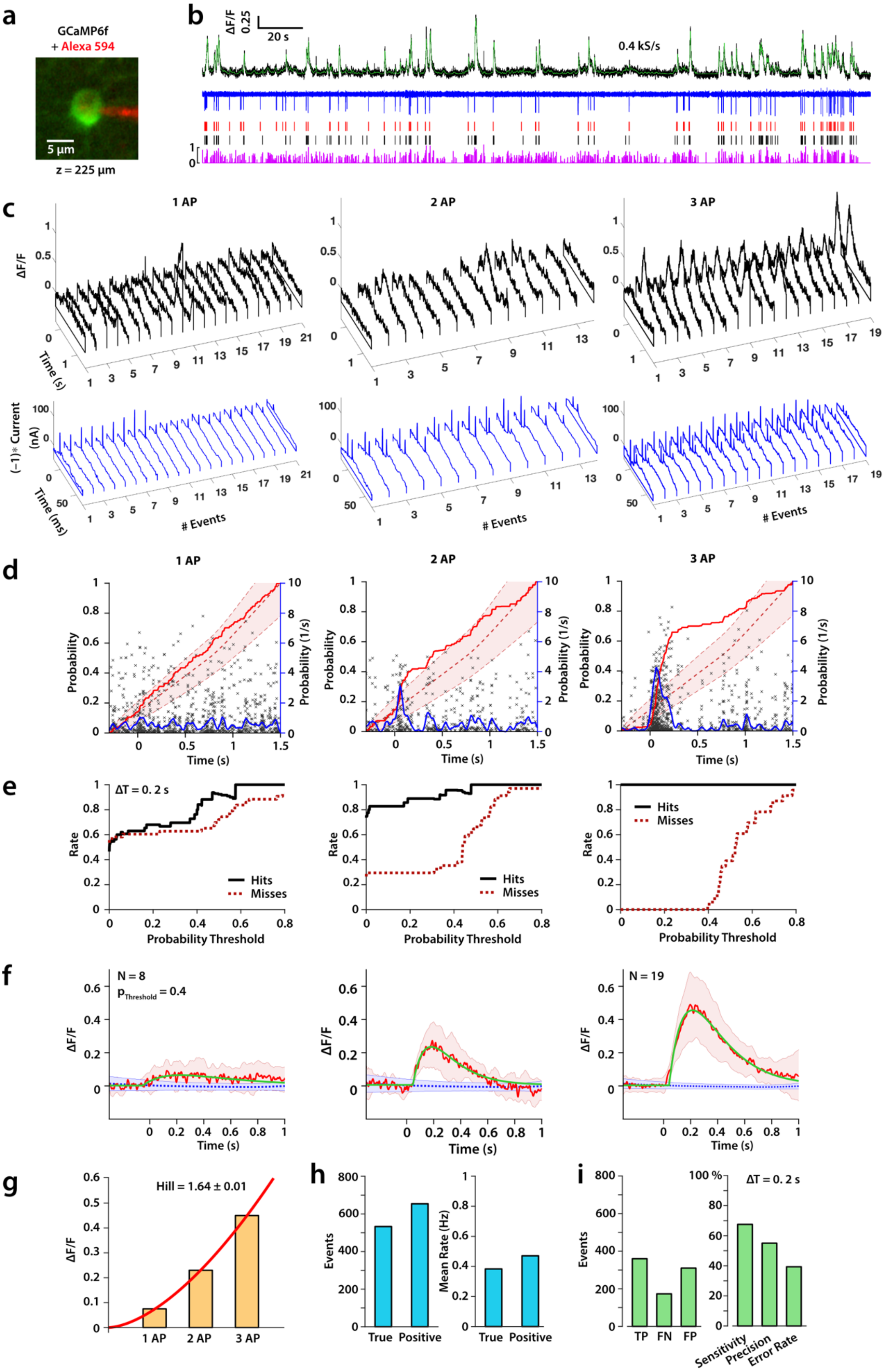
a
GCaMP6f
+ Alexa 594
5 µm
z = 225 µm
b
ΔF/F 0.25
20 s
0.4 kS/s
1
0
c
1 AP
2 AP
3 AP
ΔF/F
1
0.5
0
Time (s)
(−1)* Current (nA)
100
0
Time (ms)
50
Events
d
1 AP
2 AP
3 AP
Probability
Probability (1/s)
Time (s)
e
ΔT = 0. 2 s
Rate
Hits
Misses
Probability Threshold
f
N = 8
$p_{Threshold}$ = 0.4
N = 19
ΔF/F
Time (s)
g
Hill = 1.64 ± 0.01
ΔF/F
1 AP
2 AP
3 AP
h
Events
Mean Rate (Hz)
True
Positive
i
Events
100 %
ΔT = 0. 2 s
TP
FN
FP
Sensitivity
Precision
Error Rate

Extended Data Fig. 4 Simultaneous CASH and cell-attached patch recording
(a) Image of patch electrode-targeted neuron expressing GCaMP6f (green) and membrane-attached electrode filled with Alexa 594 (red). **(b)** Five minutes example recording from the neuron shown in (a) with GCaMP6f signal (black), MLspike-retrieved GCaMP6f signal (green), electrode current at -65 mV holding potential (blue), position of spikes inferred from the current trace (red), spikes obtained from MLspike deconvolution (black) and MLspike-estimated spike probability (magenta). **(c)** Spike-sorted GCaMP6f transients in black (first row) and electrode-measured spikes in blue (second row) for single (1 AP; 21 events), double (2 AP; 14 events) and triple (3 AP; 19 events) action potential events with the first spike at time zero and drawn from 23 minutes total recording time. Detection was subject to the condition that no further event is found during 0.6 s before the first spike and 0.7 s after the last spike. The incidence window was 30 ms. **(d)** MLSpike-estimated spike probability (black crosses) for events shown in (c) in the -0.3 to 1.5 s from the electrode-detected spike event at time zero, together with the normalized cumulative probability (red) and probability density calculated with a gaussian kernel (20 ms; blue). Dotted curve (red) represents the cumulative ensemble probability at ± SD confidence (dotted red band) bootstrapped from segments of the recordings (10^4 repetitions) where no spikes were detected. **(e)** Diagnostic of optical spike detection for 1-3 AP events as function of a probability threshold with a 0.2 s detection window following an electrode-detected spike. The true positive (hit) and false negative (misses) rate was calculated from the MLspike-detected events reaching a probability beyond threshold anywhere within the detection window. **(f)** Spike-triggered average of the GCaMP6f transient for 1 AP (8 events), 2 AP (6 events) and 3 AP (19 events) which surpassed a 0.4 probability threshold (red) with ± 1 SD (red band), biexponential fit to the mean (green; 0.33 ± 0.4 decay time constant) and the ± 1 SD bootstrap distribution of GCaMP6f transients in absence of spike events (blue). **(g)** Mean GCaMP6f response amplitude for 1-3 AP events obtained from the thresholded spike response in (f), together with polynomial fit (red). **(h)** *Left:* Total number of electrode-detected spike events (true events) and MLspike-detected events (positive events). *Right:* Mean firing rate across the whole data set evaluated from true or from positive events, respectively. **(i)** *Left:* True positives (TP), false negatives (FN) and false positives (FP) counts across the whole data set when applying a 0.2 s detection window. *Right:* MLSpike inference sensitivity, precision and error rate evaluated from the counts in (h, *left*) and (I, *left*).

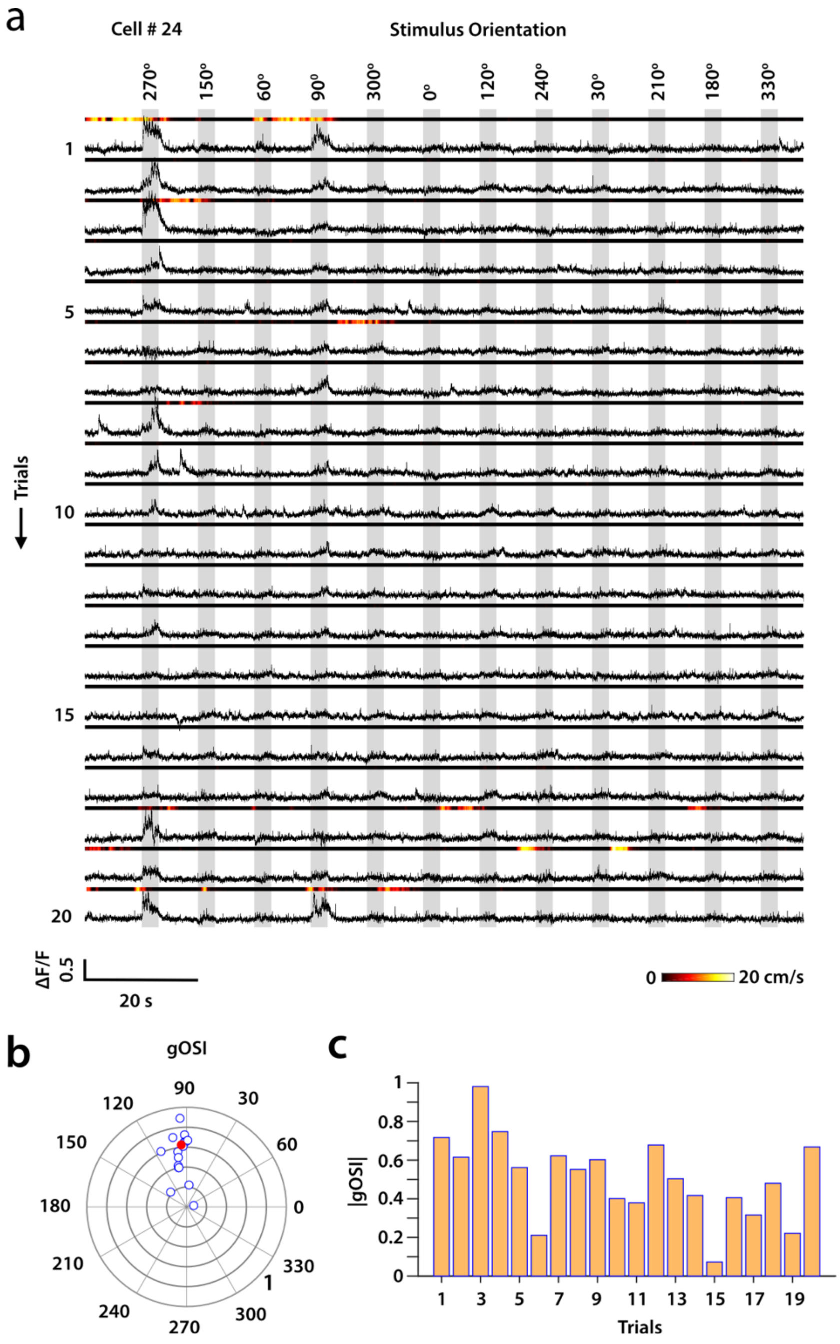

Extended Data Fig. 5 Example cell with orientation-tuned response

GCaMP6f orientation-sensitive visual responses (cell # 24 in Fig. 5d-f). **(a)** GCaMP6f fluorescence signal in response to the repeated presentation (20 repeats) of the same stimulus series (gray bars) with orientations indicated on the top of the figure. The moving speed of the animal is shown for every trial as a false-color bar together with the GCaMP6f trace (black). **(b)** Global orientation sensitivity index (gOSI) derived from single trials (blue dots) and from the trial average (red dot). **(c)** gOSI amplitude for all trials.

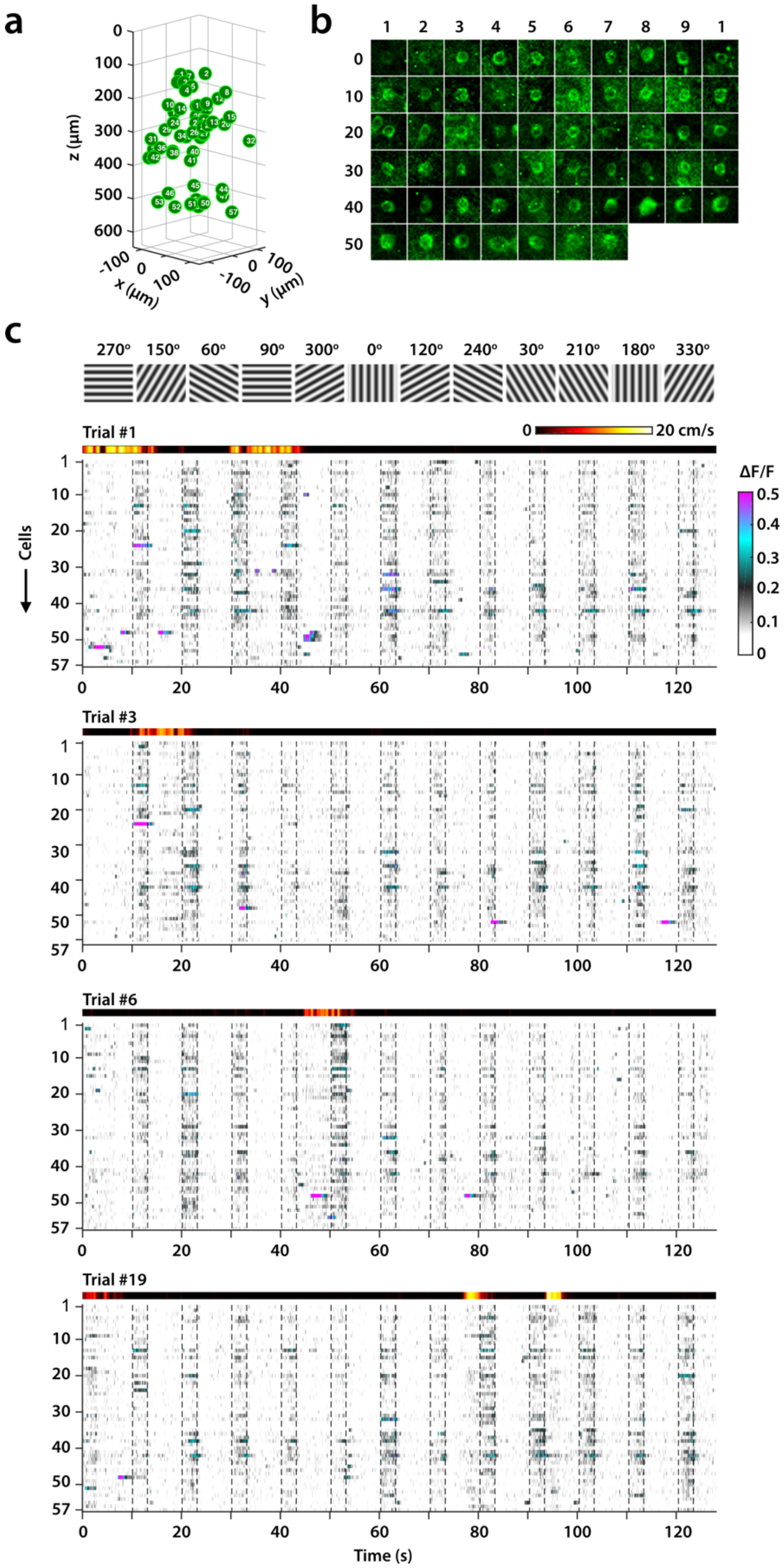

Extended Data Fig. 6 Single trial visual responses in a cell population

(a) 3D coordinates of cells in the dataset (same as in Fig. 5b-h). **(b)** GCaMP6f fluorescence images of all cells in the dataset. **(c)** False-color representation of GCaMP6f fluorescence responses to visual contrast grating stimuli (vertical dotted lines). Shown are the responses in trials n° 1, 3, 6 and 19 of a total of 20 trials (trial average shown in Fig. 5b) together with the locomotion velocity as horizontal color bar. The orientation of stimulus gratings, same for all trials, are shown on the very top.

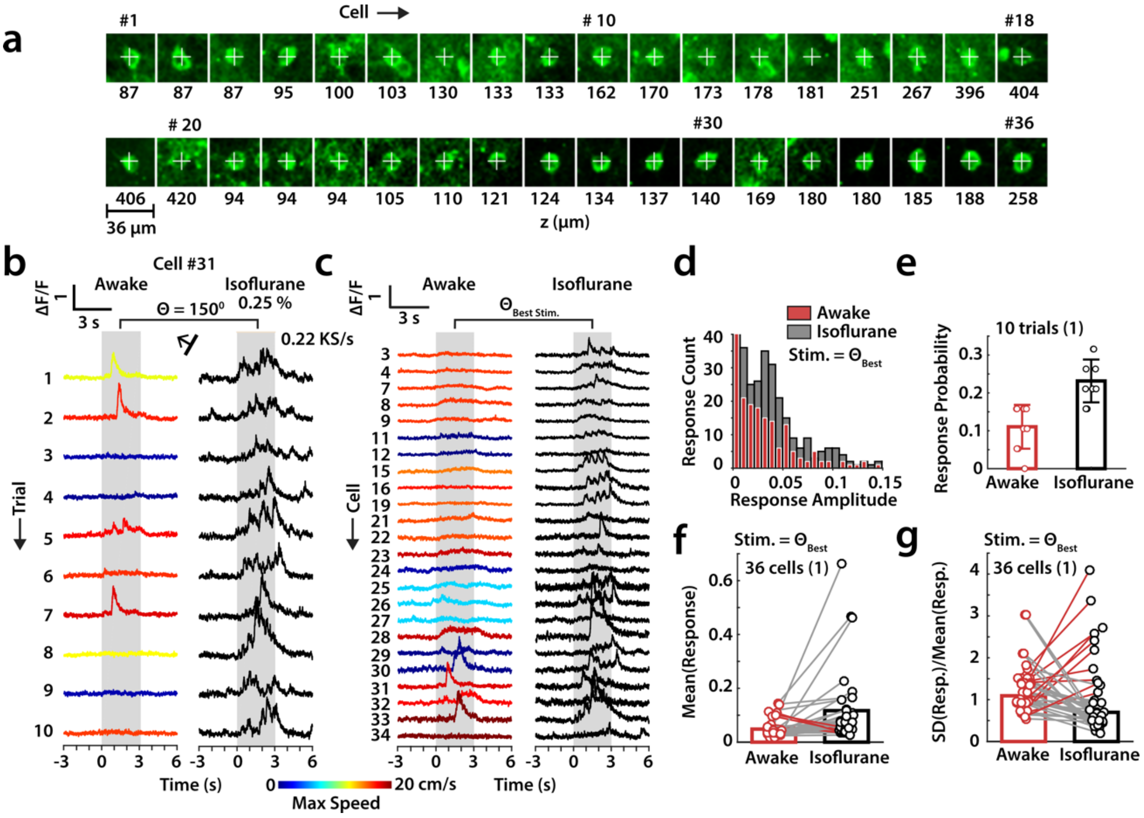

Extended Data Fig. 7

GCaMP6f responses of V1 cells in the awake versus the anesthetized state

(a) Fluorescence images of 36 cells (L2/3; two experiments; one animal) that passed the test for significant tuning response in both states ($p \leq 0.03$, bootstrap test). Values below indicate the z position below pia. **(b)** Single-trial fluorescence responses of cell #31 to the preferred orientation (150°) in the awake state (*left*) and in the anesthetized state under 0.25 % isoflurane (*right*). Traces in the awake state are color-coded according the maximum speed of locomotion of the animal. **(c)** Single-trial fluorescence responses of 24 cells by choosing for each cell the stimulus trial of maximum integral response in the awake (*left*) and anesthetized (*right*) state, using the same color code as in (b). **(d)** Overlaid histograms of response amplitude for the best stimulus across all trials and all cells in the awake (red) and anesthetized (gray) state. Responses with amplitude above 0.15 have low counts and are omitted from the figure. The zero-response bar was cropped at the top. **(e)** Measured cell-averaged response probability in single trials (mean; 10 repetitions; SD error). Trial responses to the best stimulus, as judged from the average response, were considered as positive when their amplitude was at least three times larger than baseline noise, otherwise as failures. Number of animals given in brackets. **(f)** Trail-averaged integral response amplitude for the best stimulus for all cells when recorded in the awake (red) and anesthetized (black) state. Connecting lines indicate data belonging to the same cell with red lines for cells featuring larger response in the awake state. **(g)** Standard Deviation (SD) of trial responses for the best stimulus normalized to the mean of the response for cells when recorded in the awake (red) and (black).

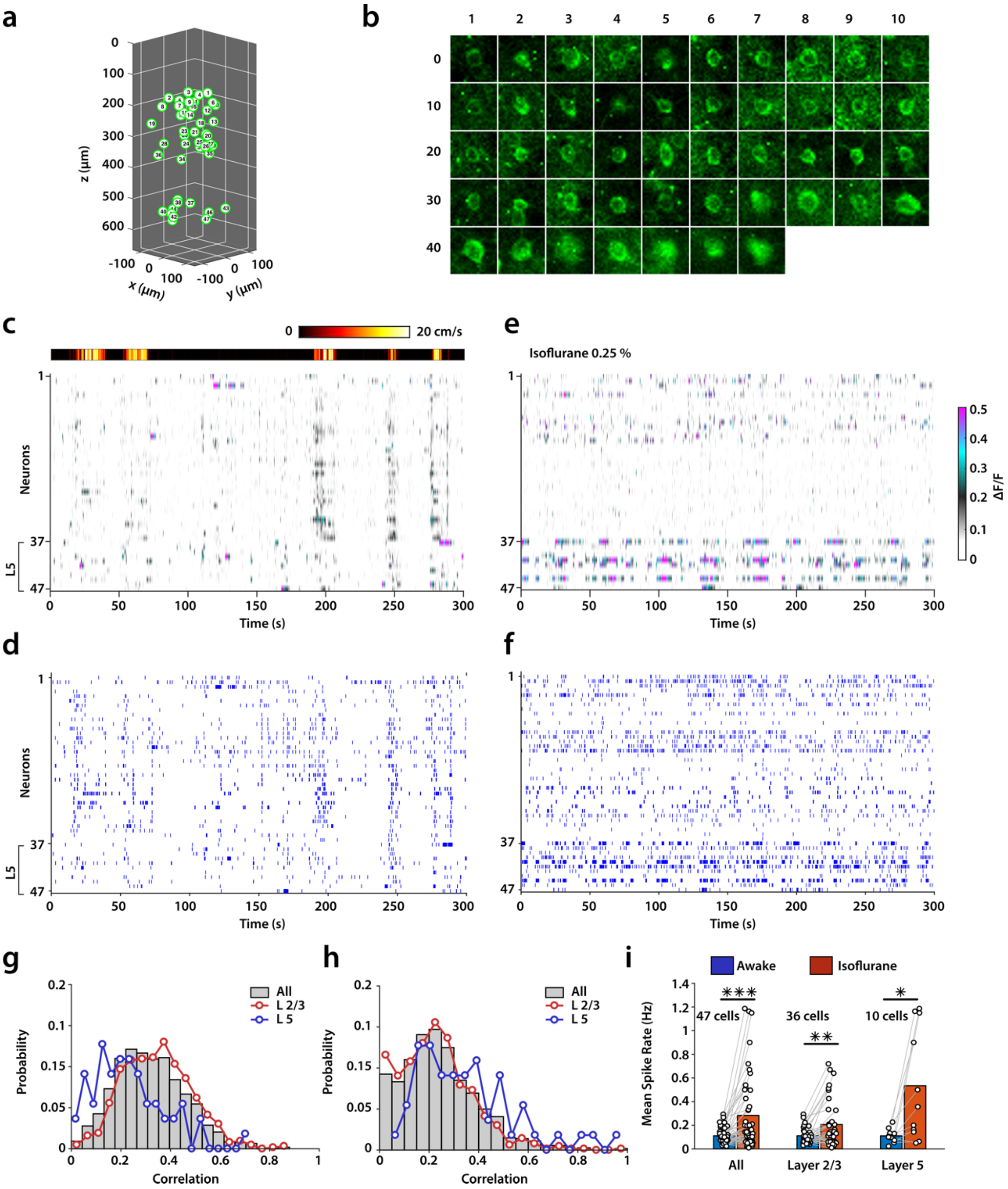

Extended Data Fig. 8 Spontaneous Ca^{2+} activity in the awake versus anesthetized state
a) 3D coordinates of cells in the dataset (47 cells). **(b)** GCaMP6f Fluorescence images of all cells. **(c)** Fluorescence traces in false colors, according to the color bar on the right side of (e) recorded in the awake state. Color bar on the top indicates locomotion velocity of the animal. **(d)** Spikes found in (c) by MLspike. **(e)** Fluorescence traces from the same cells as in (c), but with the mouse under 0.25 % isoflurane anesthesia. **(f)** Spikes found in (e) by MLspike. **(g)** Histogram of pairwise spike correlations in (d) between all cells (black), between layer 2/3 cells (red) and between layer 5 cells (blue). Spikes were counted as synchronous if they fall within a 10 ms time window. **(h)** Same as in (g), but evaluated from the dataset in (f). **(i)** Mean spike rates calculated from the spike maps in (d) and (f). Paired t-test, $p = 2 \cdot 10^{-4}$ (***; 47 cells), $2 \cdot 10^{-3}$ (**; 36 cells), $1 \cdot 10^{-2}$ (*; 10 cells). Pairs of same cells connected by lines (gray).

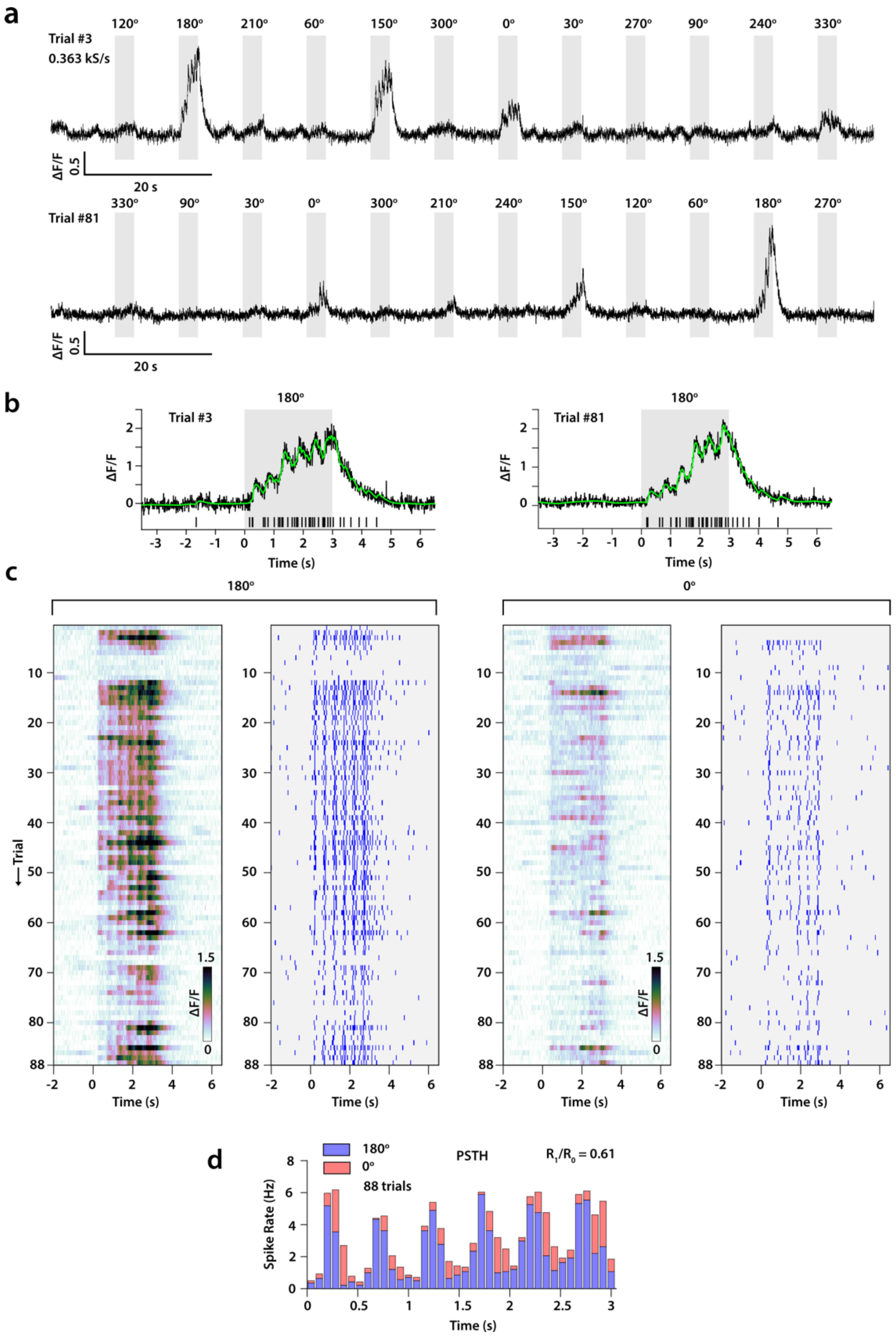

Extended Data Fig. 9 Example cell with phase-sensitive response

(a) GCaMP6f response of a layer 2/3 example cell to a stimulus series of contrast gratings with grating orientations between 0° and 360° randomized between trials and moving at a speed of 2 cycles per second (cps) under isoflurane (0.25-0.5 %) anesthesia. Sampling with 363 Hz. *Top*: Trial #3. *Bottom*: Trail # 81 (Gaussian-filtered, sigma 2.5 ms). **(b)** Responses to 180° stimulus orientation of trial #3 (*left*) and # 81 (*right*) with MLspike-infered spikes indicated as black vertical marks (*bottom*) and convolution of inferred spikes with the GCaMP6f response template (green curve). **(c)** False-color representation of the GCaMP6f responses to the 180° (left) and 0° counterpropagating stimulus (right) for 88 consecutive trials together with MLspike-inferred spikes (blue vertical lines). **(d)** Stacked peristimulus time histogram (PSTH).

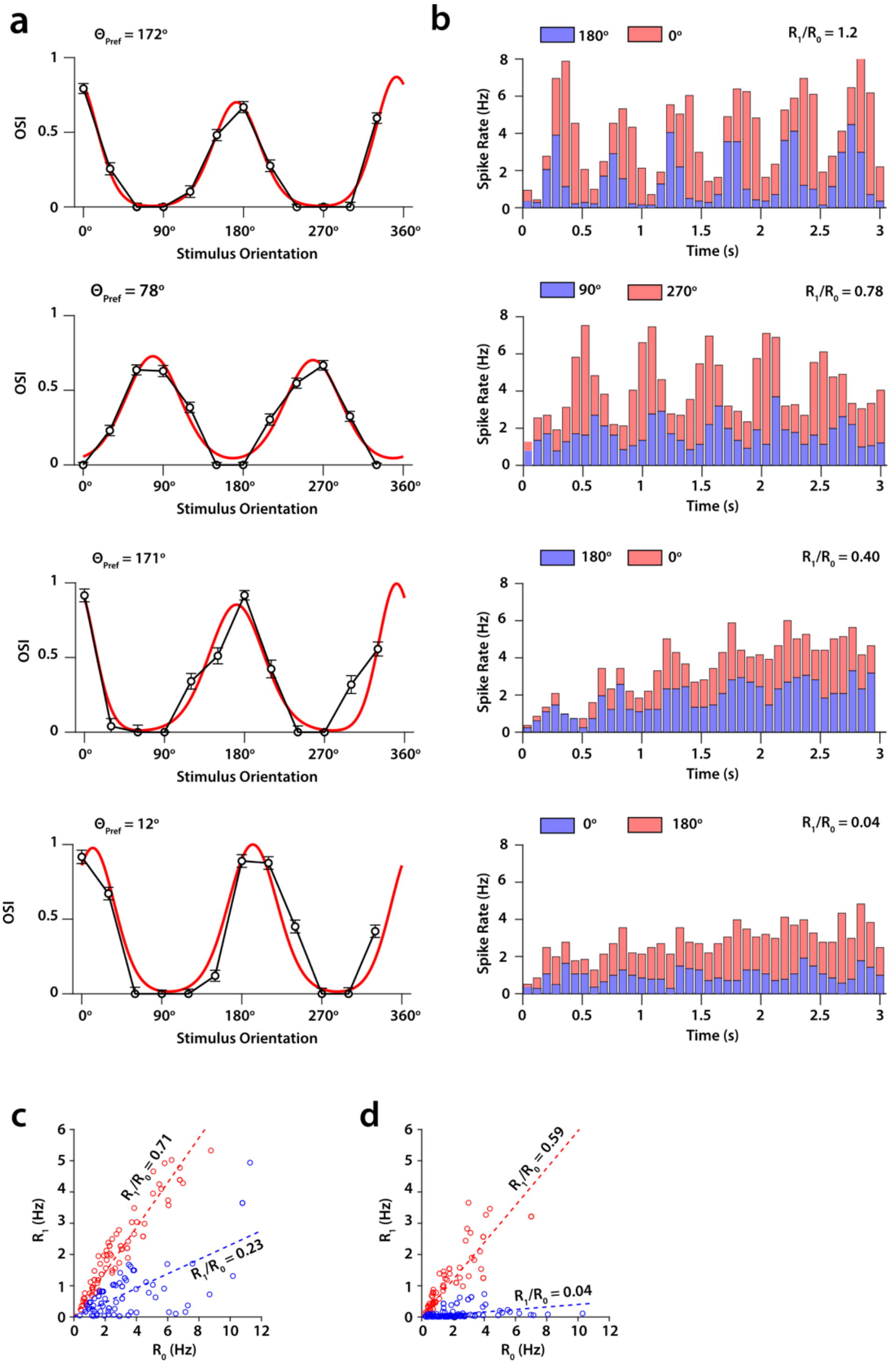

Extended Data Fig. 10 Orientation and phase sensitive responses(a) Orientation sensitivity index (OSI) for four example neurons with orientation preferences (Θ_{Pref}) 178°, 78°, 171° and 12° (*top to bottom*). Experimental (black) with biphasic fit (red). Error bars indicate SEM. **(b)** Stacked peristimulus time stacked histograms (PSTH) obtained for the neurons in (a) from 80 (# 1, #2, #4) or 50 (# 3) trials with 80 ms binning width resulting in R_1/R_0 ratios ranging from 1.2 to 0.04 (top to bottom). **(c)** Harmonic spike Rate R_1 as function of the mean rate R_0 in response to the preferred stimulus orientation and preferred direction for 155 neurons in layer 2/3. Responses classified according to R_1/R_0 larger (red) or lower (blue) than the R_1/R_0 ensemble mean. Linear fits to the data given as dashed lines. **(d)** Same as (a) for the counterpropagating direction of the preferred stimulus.

SUPPLEMENTARY MATERIAL

Fast Optical Recording of Neuronal Activity by 3D Custom-Access Serial Holography

Walther Akemann, Sébastien Wolf, Vincent Villette, Benjamin Mathieu, Astou Tangara, Jozsua Fodor, Cathie Ventalon, Jean-François Léger, Stéphane Dieudonné, Laurent Bourdieu

Supplementary Figures

Supplementary Discussion

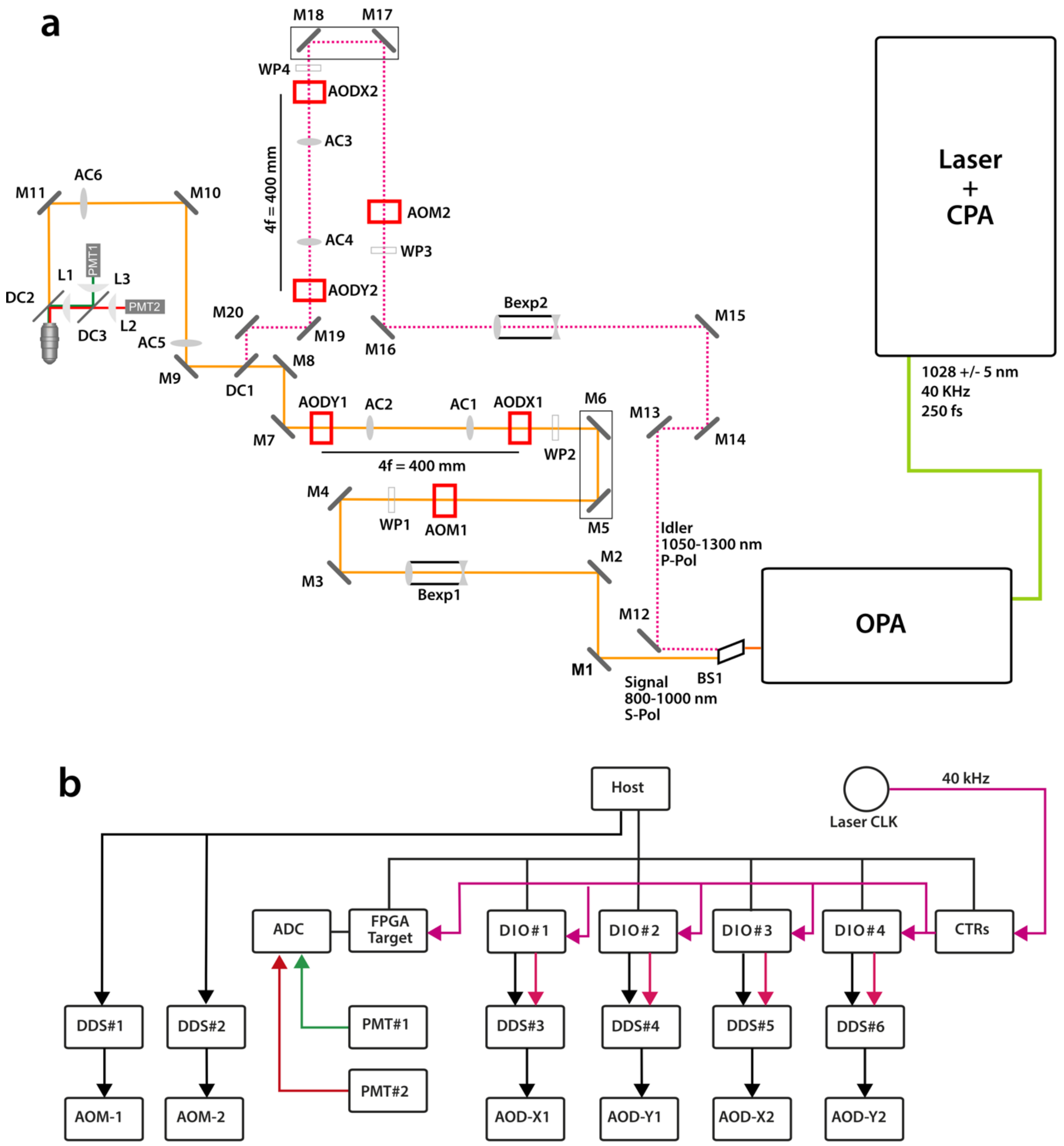

Supp. Fig. 1 3DScope: optical and electronic layout

(a) Optical layout using the following abbreviations: CPA, chirped pulse amplifier, OPA, optical parametric amplifier, M, mirror, DC, dichroic mirror, AC, achromat, L, lens, BS, beam splitter, Bexp, beam expander, WP, λ/2 waveplate, P-Pol, horizontal polarization, S-Pol, vertical polarization. **(b)** Schematic of the control layout: DDS, direct digital synthesizer, ADC, analog to digital converter, DIO, digital I/O, PMT, photomultiplier tube, CLK, laser synchronous clock signal, CTR, digital counter. Connections serve data transfer (black), timing signals (pink) and detector signals (green, red).

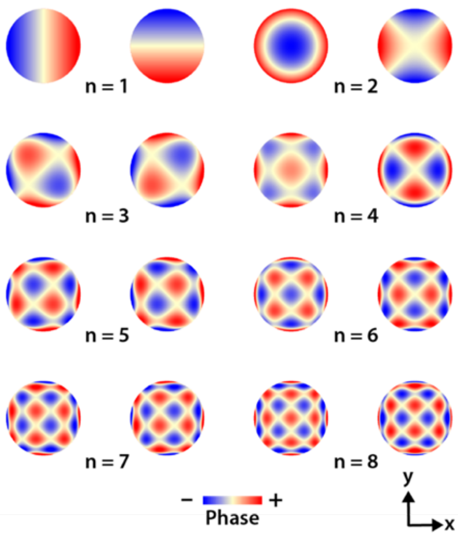

Supp. Fig. 2 Ortho-normal phase functions for biaxial spatial light modulation

Circular polynomial phase functions compatible with the geometry of a two-axis spatial light modulator (XY-SLM) up to 8th polynomial order. The functions, separable with respect to x- and y-coordinates, of the form $\varphi_n^{\pm}(x,y) = c_{\pm}(n) + \sum_{i=1}^{n}(a_{\pm}(i)\cdot x^i \pm b_{\pm}(i)\cdot y^i)$ are numerically constructed by successive Gram-Schmidt orthogonalization starting from $\varphi_0(x,y) = 1/\sqrt{\pi}$, $\varphi_1^{+}(x,y) = 2/\sqrt{\pi}\cdot x$ and $\varphi_1^{-}(x,y) = 2/\sqrt{\pi}\cdot y$ and $\varphi_n^{\pm}(x,y) = x^n \pm y^n, n \geq 2$. The zero-order mode of constant amplitude (Piston) is omitted. The total number of normal modes grows with polynomial order n as 2n+1. These modes are the two-axis equivalents to the Zernike polynomials to 8th order, used in optics to characterize aberrations in instruments with circular aperture.

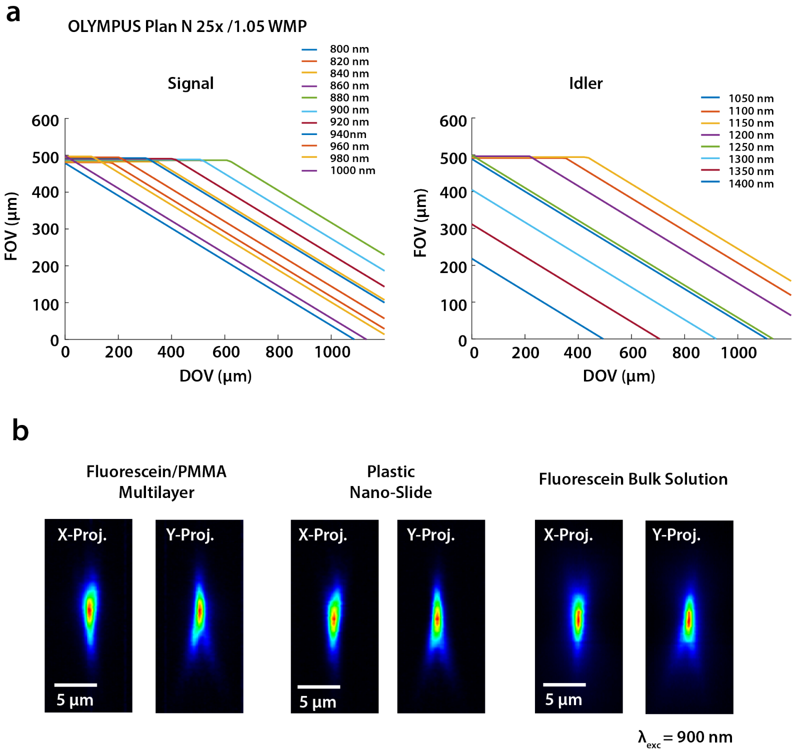

	Fluorescein/PMMA Multilayer	Color Plastic Slide D = 500 nm	Aqueous Fluorescein Layer D = 10-20 μm	Diffraction Limit
Axial FWHM	4.3 μm	4.7 μm	4.2 ± 0.8 μm	4.4 μm
Lateral FWHM	1.0 μm	1.1 μm	1.1 ± 0.2 μm	0.8 μm

Supp. Fig. 3 Optical characteristics of the 3DScope

(a) Modeled relationship between depth of view (DOV) and field of view (FOV) in the 3DScope taking into account the objective magnification (25x) and the acoustic bandwidths available at different excitation wavelengths in the signal and the idler paths. **(b)** Measurement of the fluorescence point focus in the 3DScope under two-photon excitation (900 nm) using three different fluorescence samples, a cover slip spin-coated with a Fluorescein/ PMMA layer, a plastic slide (Chroma) cut to a thickness of 0.5 µm with a microtome using a diamond knife and an aqueous 20 mM solution of fluorescein sandwiched between a glass slide and a coverslip.

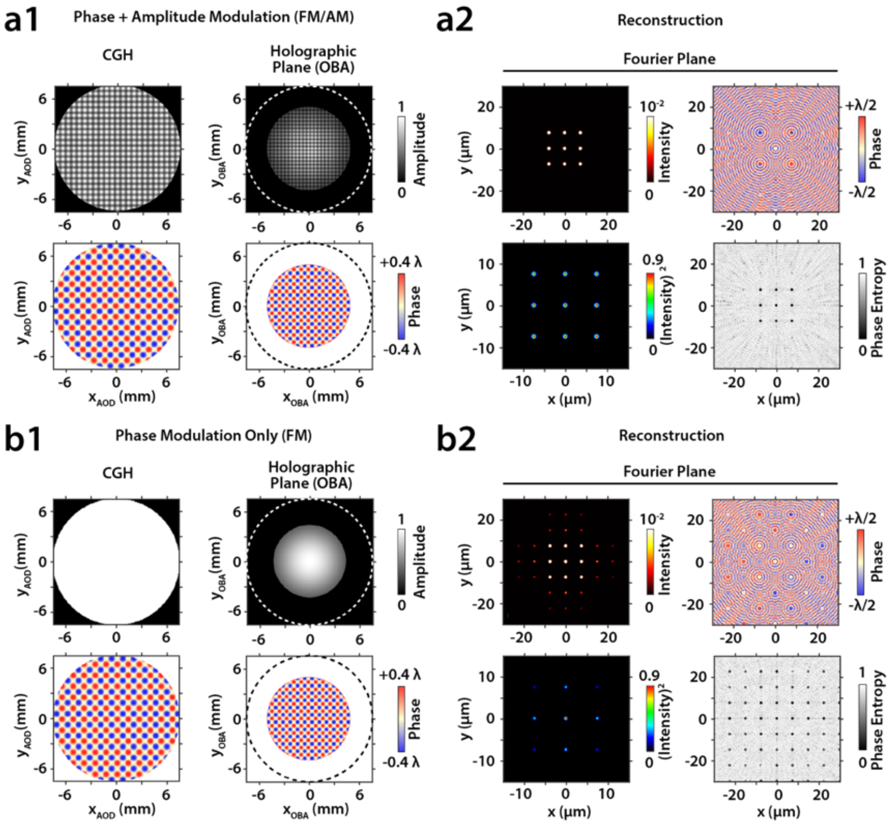

Supp. Fig. 4 Holography in the FM/AM versus FM mode

FFT reconstruction of the computer-generated hologram (CGH) given in Fig. 2b in either FM/AM mode (a) or FM mode (b). **(a1)** *Left Column*: CGH. *Right column*: Light field in the plane of the objective back aperture (OBA) of a Gaussian laser beam carrying FM/AM modulation given by the CGH. Size of the OBA indicted with a dashed line. **(a2)** Light field in the Fourier (focal) plane obtained by FFT of the OBA light field. *Left column*: Intensity and the intensity squared, with the squared intensity as a proxy for the two-photon fluorescence intensity distribution. *Right column*: Phase and phase entropy. **(b1)** and **(b2)** same as (a1) and (a2), but without AM. Notably, the reconstructed phase in the Fourier plane exhibits disc-like regions of constant phase and minimal entropy at the target sites in the FM/AM mode, while the phase outside the target sites is scrambled, indicating destructive interference. In the FM only mode, on the other hand, the reconstructed phase exhibits local flatness at side lobe positions.

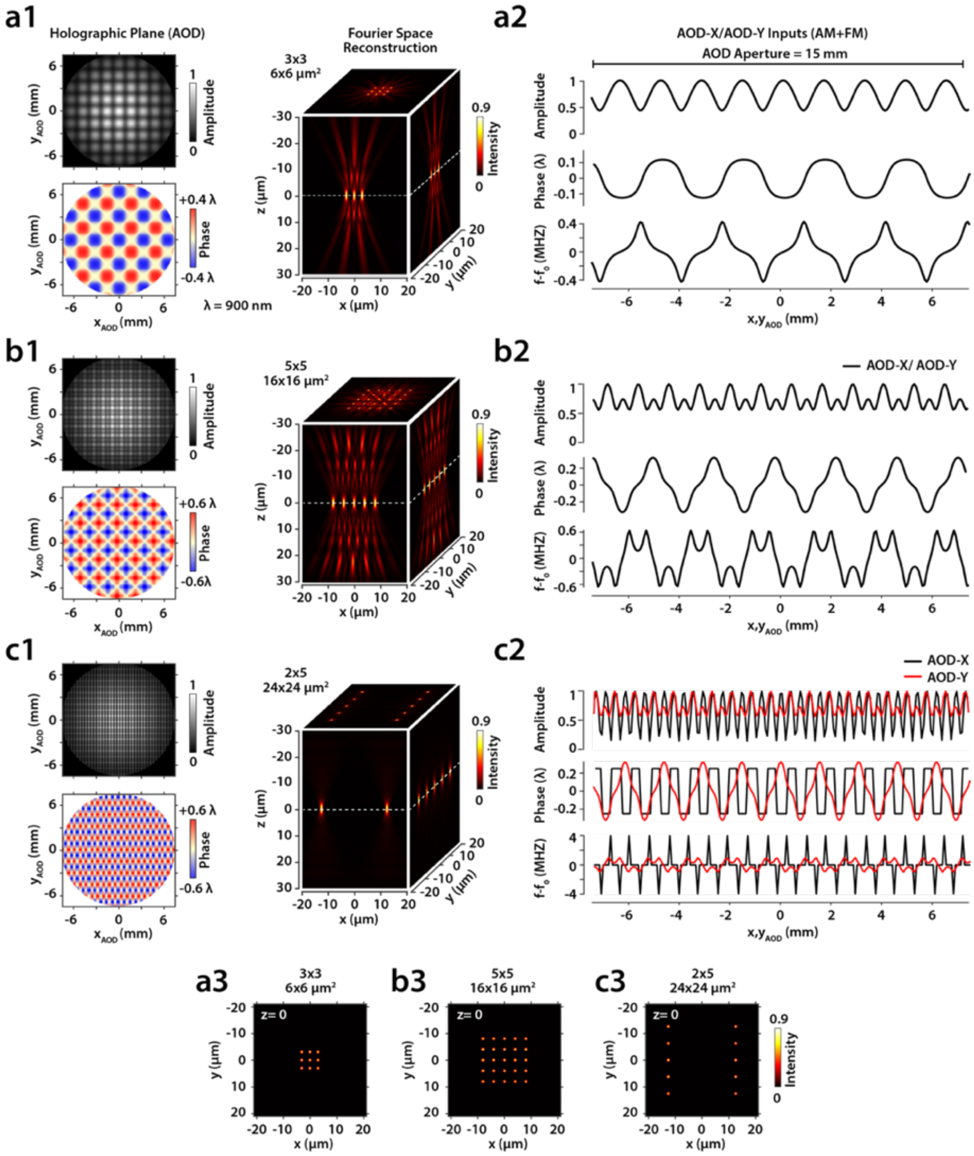

Supp. Fig. 5 3D reconstructions of 3x3, 5x5, 2x5 target CGHs

(a) 3x3 (6x6 µm^2) target. **(a1)** Left Column: Light field in the AOD plane. Right: Intensity reconstruction in Fourier space using Fourier transform and a linear phase propagator. **(a2)** AOD phase and RF input signals: AM signal (top), phase (middle) and FM signal (bottom). **(a3)** Intensity distribution in the focal plane. **(b1-3)** 5x5 (16x16 µm^2) target. **(c1-3)** 2x5 (24x24 µm^2) target.

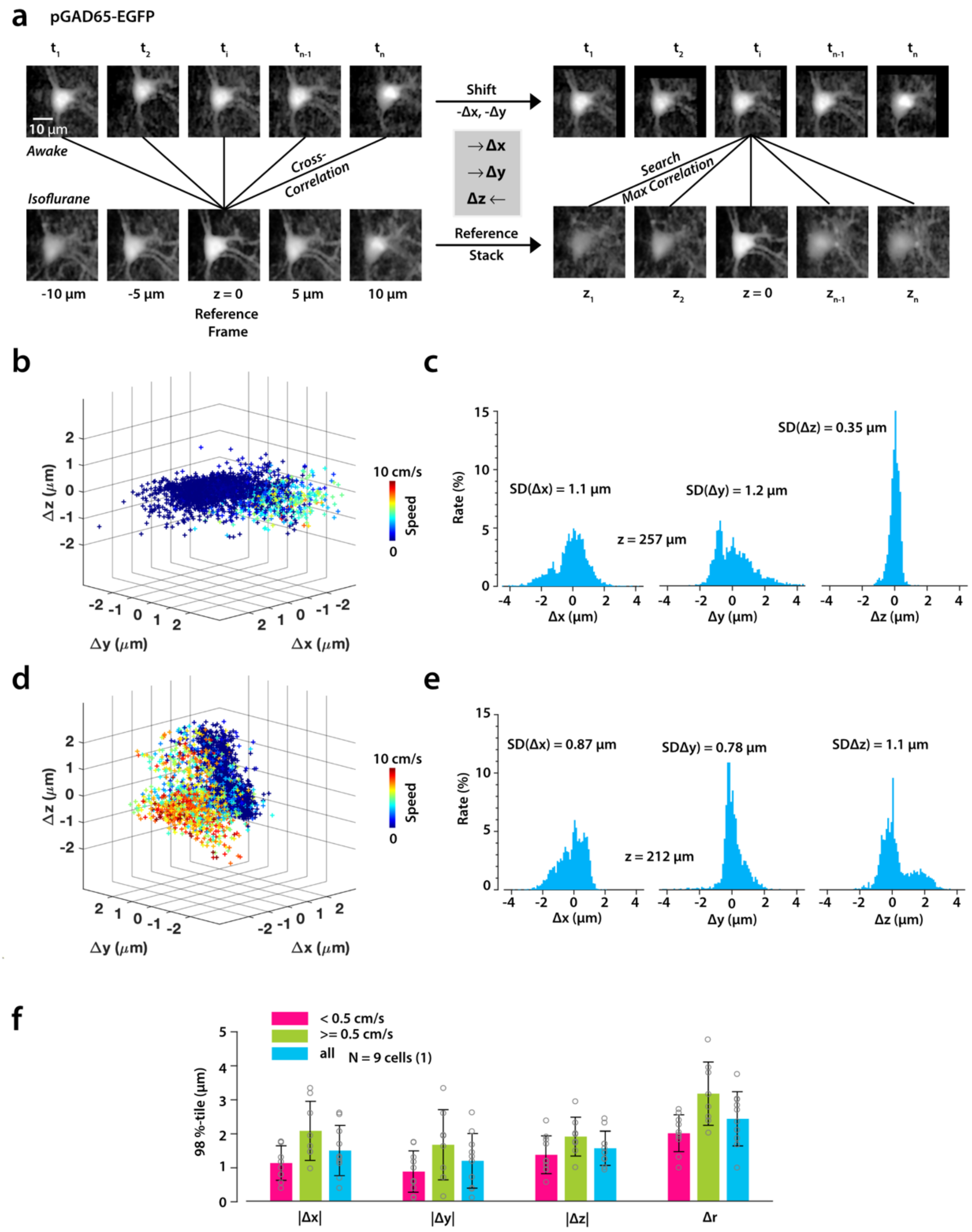

Supp. Fig. 6: Estimation of in vivo 3D movement of supra-granular neuronal cell bodies

(a) Experimental design: first, a time-lapse image stack from a recording of a single EGFP-expressing cell in a pGAD65-EGFP transgenic mouse (50x50 pixels; 16 frames/s) is x,y-aligned by frame-wise cross-correlation with the focal image of an z-image stack (50x50 pixels, $\Delta z = 0.25$ µm) of the same cell in the anesthetized animal. In a second step, the 2D-correlation between every t-frame and all z-frames is calculated and the z-position is assigned to the z-frame of highest correlation. **(b)** x-, y- and z-displacement amplitude of the cell represented in (a), color-coded according to the motion speed of the animal. **(c)** x-, y-, z-displacement histograms of the same data indicating the SD of each distribution. **(d, e)** Same estimation for a different cell in a different recording session (38 days earlier; 14 days after surgery) in the same animal. **(f)** Pooled displacement data (mean ± SD of the 98 percentile of x-, y-, z- and radial displacements; N = 9 cells; 1 animal) discriminated according to those movements that occur in the resting animal (red; motion speed < 0.5 cm/s) and the moving animal (green; motion speed >= 0.5 cm/s). Data taken from 14 to 55 days post surgery. Number of animals given in brackets.

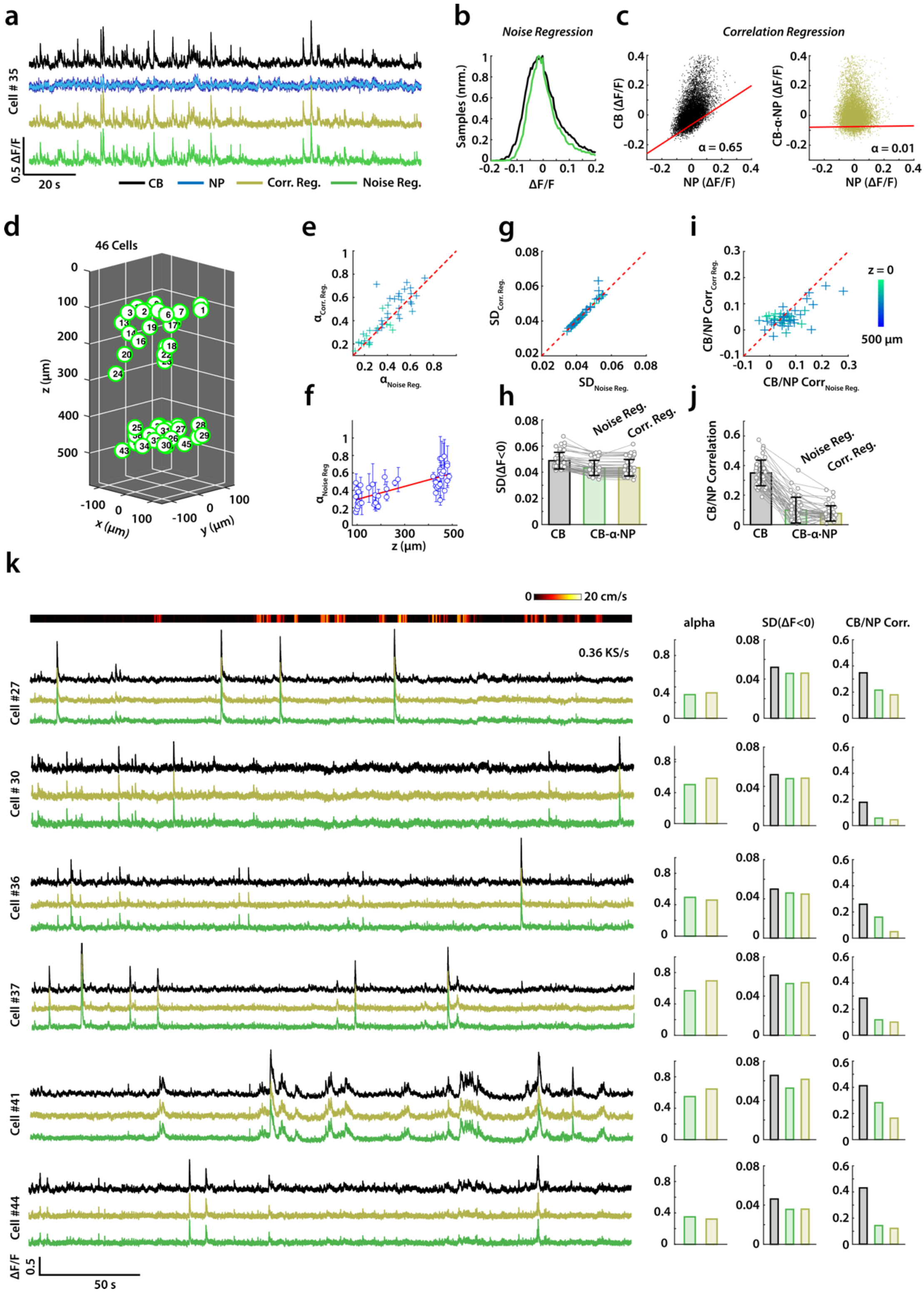

Supp. Fig. 7 Correction of neuropil signaling

Legend continues next page.

Supp. Fig. 7

Subtraction of neuropil signaling

(a) Example traces with the CB signal (black), the NP signal (dark blue), the NP signal smoothed with a 50 ms window (light blue) and the corrected signal using correlation regression (yellow) or noise regression (green). **(b)** Trace histogram of the CB trace (black) and the corrected trace using noise regression (green). **(c)** *Left*: XY-plot of NP and CB data with linear fit (red) excluding data points with large CB values owing to cellular activity, with the slope (0.65) identical to the α value. *Right*: XY-plot of NP and corrected CB data with linear fit (red) excluding cellular activity, with residual correlation reduced to 0.01. **(d)** Coordinates of 46 neurons of the data set shown in this figure. **(e)** α regression parameters (mean and SD; 3 repetitions; 46 cells) for all cells in the data set obtained from noise regression (x-axis) and correlation regression (y-axis). Dashed red line indicates the identity manifold. **(f)** Noise regression-derived α values for all cells, plotted as function of the z coordinates. Red line indicates a linear fit to the data. Error bars represent SD. **(g)** Residual baseline noise, SD(ΔF/F < 0), after noise regression (x-axis) and correlation regression (y-axis). **(h)** Baseline noise, mean and SD for all cells, of the CB raw data (black) and after noise (green) and correlation (yellow) regression. Error indicated as SD. Lines (gray) connect same cells. **(i)** Residual correlation coefficient of CB and NP trace, for all cells in the data set, after noise regression (x-axis) and correlation regression (y-axis). Error indicated as SD. **(j)** Correlation of CB and NP trace, mean and SD for all cells in the dataset, before regression (black), after noise (green) and correlation (yellow) regression. CB parameter obtained with noise regression. **(k)** Six example cells (#27, #30, #36, #37, #41, #44). *Left column*: CB raw trace (black), and same trace after noise (green) and correlation (yellow) regression. Color bar on top indicates walking speed of the animal. *Right column*: Regression parameter (*left*), baseline noise SD(ΔF<0) (*middle*) and correlation coefficient of CB and NP trace (*right*) with the same color code as for the traces on the left side.

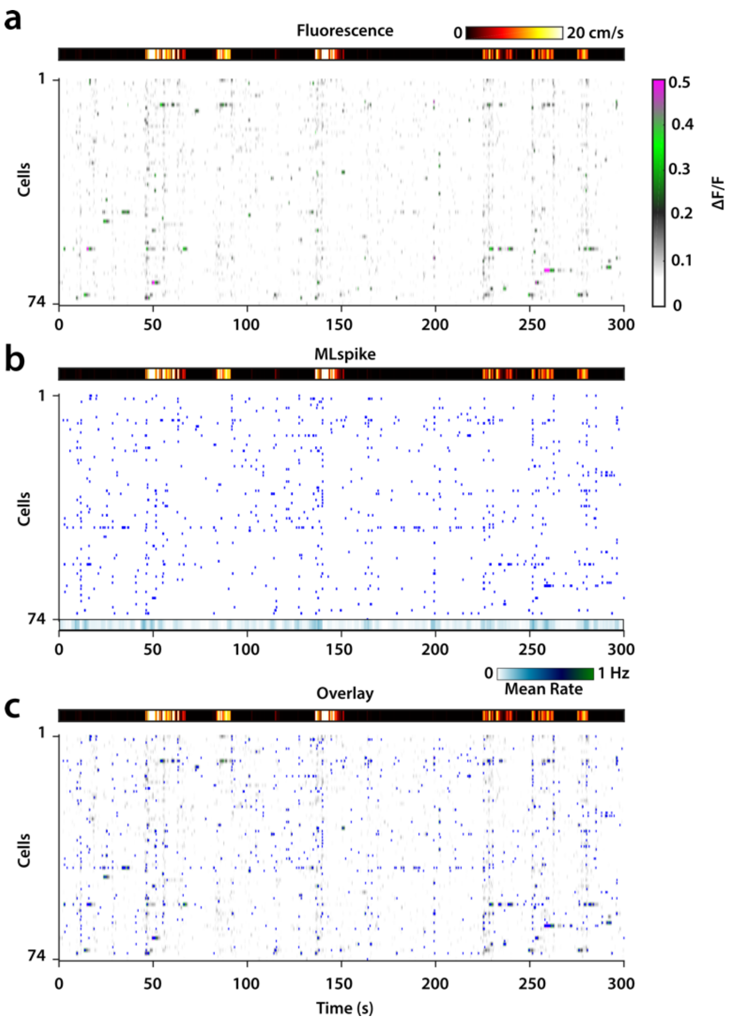

Supp. Fig. 8 Event detection from GCaMP6f CASH recordings

(a) GCaMP6f fluorescence traces from 74 cells in false-color representation according to color bar on the left. Same dataset as in Fig. 4. Color bar on the top represents locomotion velocity of the animal. **(b)** MLspike-detected spike events with mean spike rate (74 cells; 0.2 s bin width; *bottom*). **(c)** Overlay of (a) and (b).

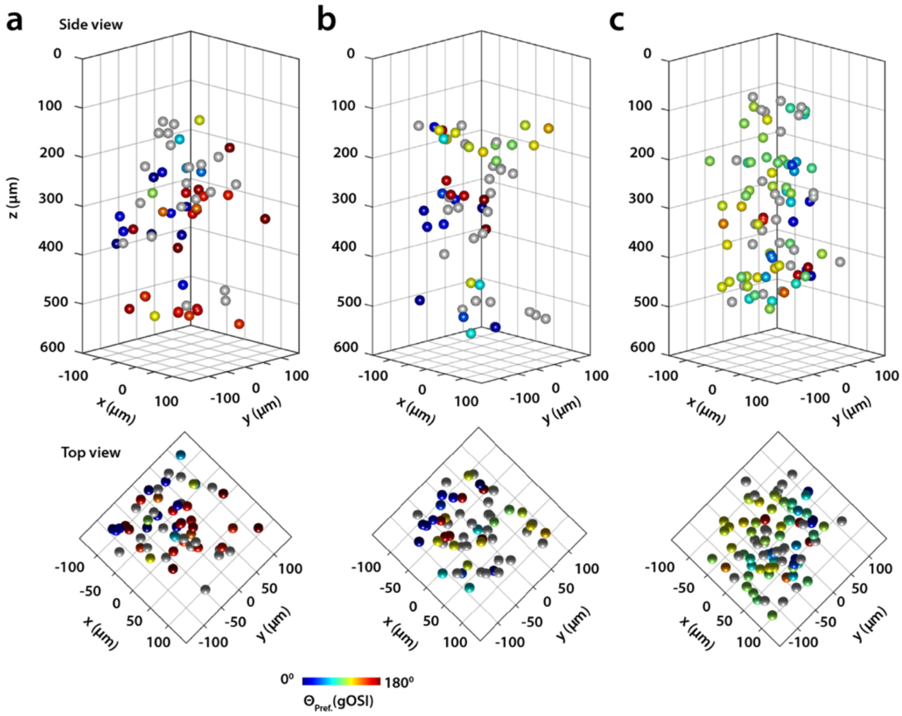

Supp. Fig. 9 3D distribution of orientation sensitivity
Measured angles of orientation tuning of neurons obtained from the vector sum of responses across all stimulus orientations, gOSI, in three different experiments in the painted ball representation in side view (top) and top view (bottom). **(a)** Same data as given in Fig. 5d. **(b)** and **(c)** display data from two different experiments in the awake state performed in the same mouse, but different selections of cells.

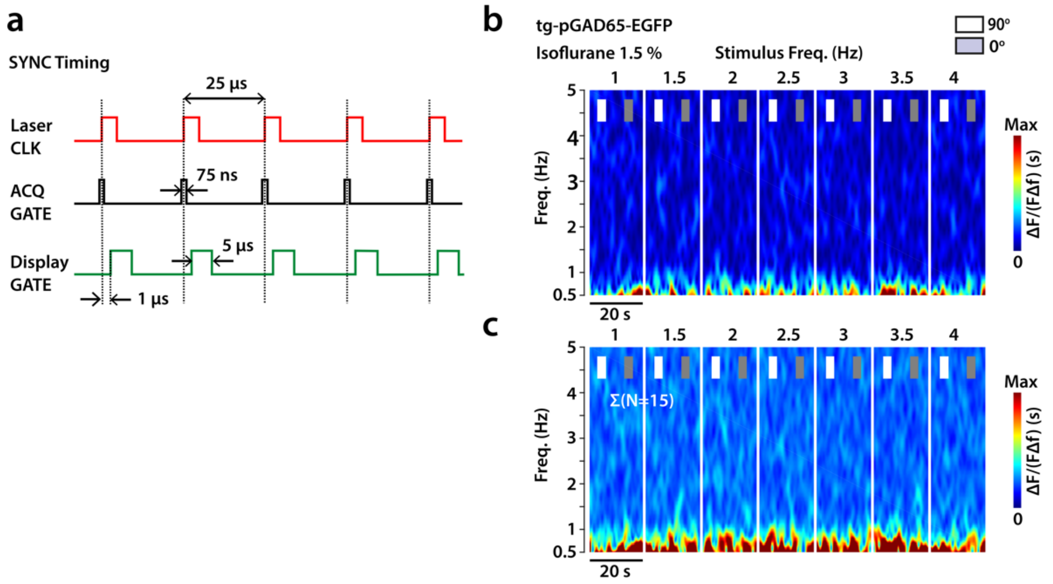

Supp. Fig. 10 Suppression of stimulus artifacts in recordings of visual responses (Control)

(a) Timing protocol for gated stimulus presentation. The screen is switched on and off in sync with the laser clock in such a way that the screen gate is off at least 18 µs before the acquisition gate opens. **(b)** Control experiment using the same stimulus protocol as in Fig. 6c, but with a mouse expressing EGFP instead of GCaMP6f (1.5 % isoflurane). *Top*: STFT calculated from the 10 trial average of the data of one cell. *Bottom*: Average STFT average including data from 15 cells.

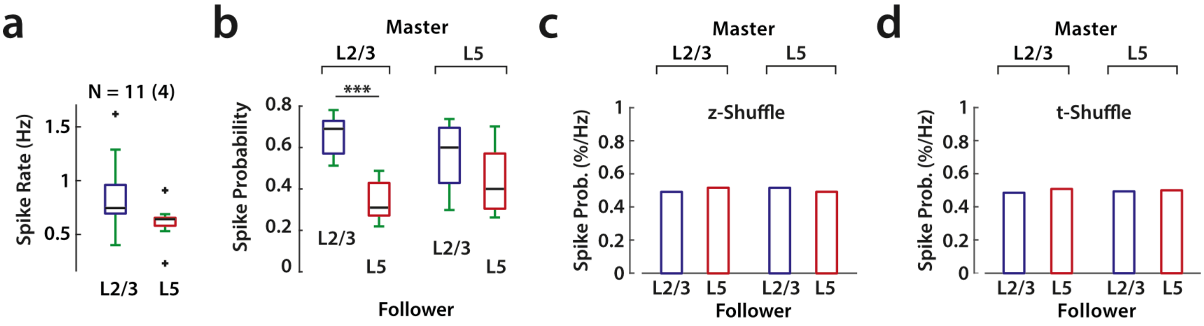

Supp. Fig. 11 Master-follower spike propagation analysis (Controls)

(a) Median rate (black bar; N = 11 experiments; 4 animals) of BSD-inferred spikes of layer 2/3 (L2/3) and 5 (L5) neurons including awake and anesthetized conditions with 1st and 3rd quartile (box), ± 2.7 SD range (green whiskers) and outliers (black crosses). **(b)** Probability, p_k^l (median; black bar), of a spike emitted in a cell of layer k (master) having the first follower spike emitted in a neuron in layer l (follower). Same data as in (a). P-value $p = 1.8 \cdot 10^{-4}$ (***; T-test, unpaired, two-sided t-test) between layer 2/3 versus layer 5 follower cells if cells in layer 2/3 were the master, whereas the difference was not significant if cells in layer 5 were the master. The probability p_k^l is equivalent to the probability $\hat{p}_k^l$ shown in panel Fig. 6o, but without normalization with regard to cell count and mean firing rate. **(c-d)** Spike probability (mean) obtained from master-follower analysis analogous to Fig. 6o of the same dataset after shuffling the z-positions of cells (c) or shuffling the spike trains for each follower cell (d).

Supplementary Discussion

Response-to-noise ratio of the GCaMP6f response

Signal-to-noise ratio (SNR) specifies the amplitude of the probe response relative to the amplitude of the noise in a given recording. In this way, SNR evaluates the information present in single data points close to the maximum of the response rather than the information carried by the entirety of sample points covering the response transient. In consequence, SNR underestimates the information available in highly oversampled signals. As a measure of the effective signal-to-noise ratio of the integral response, we define the response-to-noise ratio (RNR) as the integrated response above baseline noise divided by the standard error of the noise signal. Assuming a biexponential time course of the GCaMP6f response with fixed rise (50 ms) and decay (300 ms) time constants and fixed single-spike response amplitude (7.5 %), numerical integration of the response at variable level of noise (SNR from 1 to 3.5) reveals the RNR gain to be expected from accelerated sampling (Supp. Fig. 12).

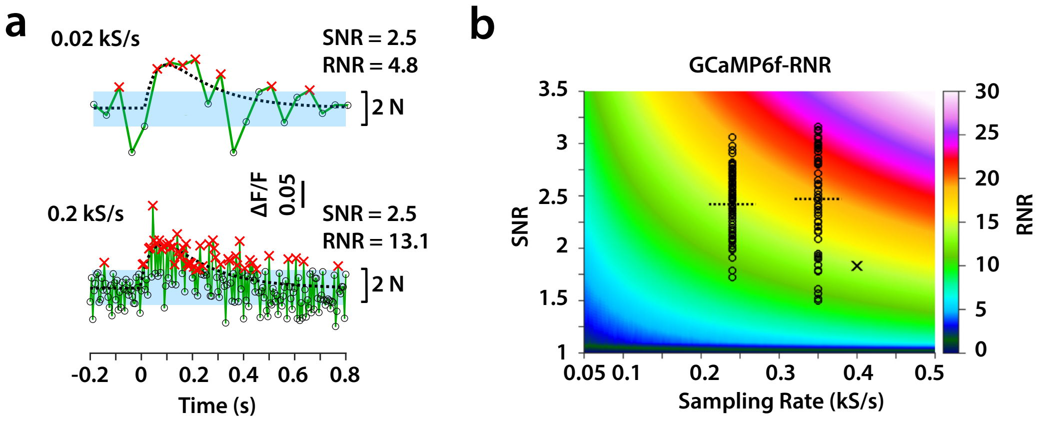

Supp. Fig. 12: GCaMP6f response-to-noise ratio (RNR)

(a) *Schematic of an isolated GCaMP6f spike response (τ_{ON} = 0.05 s, τ_{OFF} = 0.3 s, $\Delta F/F$ = 0.075; dashed line) when sampled at 0.02 kHz (top) and 0.2 kHz (bottom) with N, the baseline noise (SD). In green: GCaMP6f response with simulated Gaussian noise (SNR 2.5). The response-to-noise ratio (RNR) is defined as the mean of samples (red crosses) above baseline noise (blue horizontal band) divided by the error of the mean of the noise.* ***(b)*** *RNR for the GCaMP6f response to single spikes as function of SNR and sampling rate (in kilo samples/s). Presumed single spike RNR of recordings shown in Fig. 4b-j (0.24 kHz; first trial) and Fig. 5a-h (0.35 kHz; first trial) as black circles (single cells; horizontal dashed line: ensemble mean). RNR of the recording with simultaneous electrophysiology (0.4 kHz; Fig. 4k-m) indicated as black cross.*

The relationship between SNR and RNR follows from the following estimation. Because of the fast onset and slow decay of the GCaMP6f response, the response may be approximated by an instantaneous step onset followed by an exponential decay with time constant τ_{off} giving rise to a $FWHM \approx \ln(2) * \tau_{off}$. By considering response values above half maximum, the integrated mean response, *R*, and the the standard error of the noise, SEM_{noise}, are then given as:

$$R \approx f_R \cdot S_{peak} \;\; with \;\; f_R := \left(ln(2)\,\tau_{off}\right)^{-1} \int_0^{ln(2)\tau_{off}} e^{-t/\tau_{off}}\, dt$$

$$SEM_{noise} = SD_{baseline} / \sqrt{ln(2)\tau_{off} r_{acq}}$$

with $r_{acq} = r_{data}/n_{cells}$, the sampling rate, $r_{data} = 2 \cdot 10^4/s$, the total data throughput of the 3DScope, and n_{cells}, the number of sampled cells (POIs). The response-to-noise ratio, $RNR := R/SEM_{noise}$, therefore follows as:

$$RNR \approx f_R \cdot \sqrt{ln(2)\tau_{off}r_{acq}} \cdot SNR$$

Therefore, with SNR fixed by the experimental conditions of the recording, RNR increases with the square root of the applied sampling rate. With τ_{off} (0.33 s), f_R (0.72) and the measured single spike peak response S_{peak} (≈ 7.5 %) and baseline noise $SD_{baseline}$ (≈ 3.3 %, see Fig. 4f) this results in the following estimates, valid under recording conditions in this work: $SNR \approx 2.3$ and $RNR \approx 0.83\sqrt{r_{acq}/Hz} = 116/\sqrt{n_{cells}}$.

Signal-to-noise ratio of GCaMP-CASH recordings

The 3DScope was designed to perform fluorescence recording close to the photon shot noise limit, thus:

$$SNR \leq \mathrm{SNR}_{\text{shot noise}} = \Delta F/F \cdot \sqrt{n_{ph}} \qquad \text{(Eq. 1)}$$

with $\Delta F/F$, the effective fluorescence response amplitude of the probe (APs < 4; Ext. Fig. 4g), and n_{ph}, the mean number of baseline photons detected during sampling time bins. In the following, we estimate n_{ph} in GCaMP-CASH from given experimental parameters in comparison to standard 2-photon imaging.

Abbreviations

	Two-photon excitation and optical detection
λ_0	Laser wavelength in vacuum
n	Index of refraction of water (n = 1.33)
τ_L	Laser pulse FWHM
T_L	Laser pulse repetition time interval
P_L	Mean laser power applied in one focal spot
E_L	Pulse Energy
d_L	Laser duty cycle $d_L = \tau_L/T_L$
f_C	Geometrical collection yield of the objective
f_F	Optical filter and lens transmission of the detection optics
q_{det}	Quantum yield of the detector
c_{probe}	Cytosolic concentration of the probe
V_{ex}	Single spot two-photon excitation volume
q_{em}	Fluorescence quantum yield of the probe
p_{TPA}	Probability of molecular two-photon absorption of the probe
σ_2	Two-photon cross section of the probe in the resting state
Φ_{ex}	Instantaneous laser photon flux in the focal plane
NA	Numerical aperture (NA = 1.05; OLYMPUS XLPlan WMP 25x)
f_{obj}	Objective focal length
D	Size of objective entrance pupil (Diameter)
f_{fill}	Radial fill factor of the objective pupil in the excitation path (f_{fill} = 0.66 in the 3DScope)
w_0	Gaussian beam waist in the objective focal plane $w_0 \cong 2\lambda_0 f_{Obj}/(\pi\, n\, f_{fill}D)$
z_R	Rayleigh length of a Gaussian beam $z_R \cong \pi w_0^2\, n/\lambda_0$
	Data acquisition
r_{acq}	Sampling rate
n_{Cell}	Number of cells sampled
n_{acq}	Number of laser pulses contributing to one sampling bin of one cell
ρ_C	Volume density of cells in the population of interest
A_C	Surface area of the cytosolic compartment of cells of interest (cell body) in the focal plane

Abbreviations continued

	CASH mode
n_{holo}	Number of focal spots generated by the hologram
f_{holo}	Holographic yield; fraction of focal spots contributing to the cellular signal
n_{foci}	Number of focal spots contributing to the cellular signal; $n_{foci} = f_{holo}\, n_{holo}$
l_x	Feed size of the focal grid in x-direction (generated by the X-AOD)
l_y	Feed size of the focal grid in y-direction (generated by the Y-AOD)
$\hat{P}_L$	Total laser power $\hat{P}_L = n_{holo}\, \mathrm{P_L}$
r_{data}	Data throughput of the microscope (number of sampled neurons per second)
	Imaging mode
f_{pix}	Pixel yield; fraction of pixels in a frame used to extract the fluorescence signal of single cells
l_z	Axial segmentation length

As n_{ph} depends on details of the sampling protocol applied in each case, it is useful to first estimate, n_{ph}^1, the number of detected photons per laser pulse emanating from one focal spot:

$$n_{ph}^1 = \frac{1}{2}\, c_{probe}\, V_{ex}\, f_C\, f_F\, q_{det}\, q_{em}\, p_{TPA} \qquad \text{(Eq. 2)}$$

Approximating the spatial-temporal profile of the laser pulse within the two-photon excitation volume by a square hat function of temporal width τ_L, p_{TPA} is given by[1]:

$$p_{TPA} \cong 1 - exp(-\sigma_2 \phi_{ex}^2 \tau_L) \qquad \text{(Eq. 3)}$$

which simplifies to $p_{TPA} \cong \sigma_2 \phi_{ex}^2 \tau_L$ for $P_{TPA} < 0.5$. Making use of $\phi_{ex} \cong \frac{\lambda_0}{hc}\frac{T_L}{\tau_L}\frac{1}{\pi w_0^2} P_L$ gives:

$$p_{TPA} \cong \sigma_2 \left(\frac{\lambda_0}{hc}\right)^2 \frac{\tau_L}{d_L^2}\, \frac{1}{(\pi w_0^2)^2}\, P_L^2 \qquad \text{(Eq. 4)}$$

and using[2] $V_{ex} \cong \pi w_0^2 \cdot 2 z_R \cong 2(\pi w_0^2)^2\, n/\lambda_0$:

$$n_{ph}^1 \cong\; c_{probe}\, f_C\, f_F\, q_{det}\, q_{em}\, \sigma_2 \frac{n\lambda_0}{(hc)^2}\, \frac{\tau_L}{d_L^2}\, P_L^2 \qquad \text{(Eq. 5)}$$

Notably, n_{ph}^1 does not depend on the actual size of the excitation volume as long as the excitation falls into the cytosolic space of the target cell. Once n_{ph}^1 is known, n_{ph} follows from:

$$n_{ph} = n_{acq}\, n_{foci}\, n_{ph}^1 \qquad \text{(Eq. 6)}$$

where n_{foci} is the number of grid spots contributing to excitation of the probe in cells of interest. In general, $n_{foci} \leq n_{holo}$.

The case of CASH acquisition

In CASH, cells are sampled with one laser pulse per sample bin, thus $n_{acq} = 1$, using amplified laser pulses for excitation, to maximize the photon yield per pulse, and distributing the pulse energy equally among the grid spots, to avoid saturation of the probe. In the following we assume excitation at 30 % saturation ($P_{TPA} = 0.3$), which according to Eq. 3 implies 17 µW mean laser power (E_L 0.42 nJ) per focal spot, and hence 0.42 mW in case of the 5x5 grid pattern (Fig. 4a), by using the two-photon cross section of EGFP of $3 \cdot 10^{-57}$ $m^4 s$ (940 nm; pH 8)[3]. From Eq. 6 we calculate n_{ph} and SNR as function of c_{probe} and n_{foci} (Supp. Fig. 13), while regarding all other quantities as fixed parameters defined either by the optical design (3DScope) or the molecular properties of the probe (GCaMP6f).

Parameters used in evaluating SNR in CASH mode

f_C	0.2 (NA 1.05)	p_{TPA}	0.3	f_{obj}	8 mm
f_F	0.8	T_L	25 µs	D	15.12 mm
q_{det}	0.45	τ_L	200 fs	f_{fill}	0.66
q_{em}	0.6	d_L	$8 \cdot 10^{-9}$	n_{acq}	1
σ_2	$3 \cdot 10^{-57}$ m^{4}s	λ_0	940 nm		

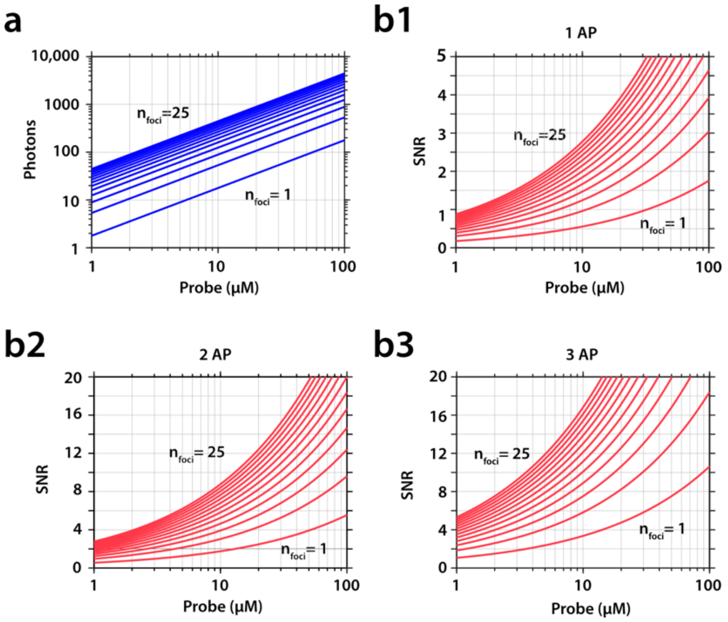

Supp. Fig. 13
(a) *Number of estimated baseline photons n_{ph} per sample bin as function of cytosolic concentration of the probe and the number of focal spots, n_{foci} = 1,3,…,25.* ***(b1-3)*** *Estimated signal-to-noise ratios for the GCaMP6f response to single (1 AP), double (2 AP) and triple action potentials (3 AP) using the data in (a) and the response amplitudes given in Ext. Fig. 4g. For consistency with the experimental CASH data, the SNR calculation includes the effect of a three-point smoothing filter.*

The case of imaging acquisition

In imaging mode, n_{holo} = 1 and $n_{acq} = f_{pix}/(r_{acq}T_L)$. Because of the large difference in duty cycle between a standard 2-photon microscope, with 80 MHz pulse rate and 200 fs pulse width ($d_L = 1.6 \cdot 10^{-5}$), and the 3DScope ($d_L = 8 \cdot 10^{-9}$) saturation occurs at much higher laser power (Supp. Fig. 14a), at 34 mW to reach 30 % saturation (Eq. 3), for instance, which is unsustainable because of tissue heating (see Discussion). For estimation we therefore reduced the laser power to 8 mW (E_L 0.1 nJ) equivalent to 2 % probe saturation (Eq. 3). Using Eq. 5 and Eq. 6 we estimate n_{ph} and SNR as function of c_{probe} and f_{pix}.

Parameters used in evaluating SNR in imaging mode

f_C	0.2 (NA 1.05)	P_L	8 mW	f_{obj}	8 mm
f_F	0.8	T_L	12.5 ns	D	15.12 mm
q_{det}	0.45	τ_L	200 fs	f_{fill}	0.66
q_{em}	0.6	d_L	$1.6 \cdot 10^{-5}$	n_{holo}	1
σ_2	$3 \cdot 10^{-57}$ m^{4}s	λ_0	940 nm	r_{acq}	20 Hz

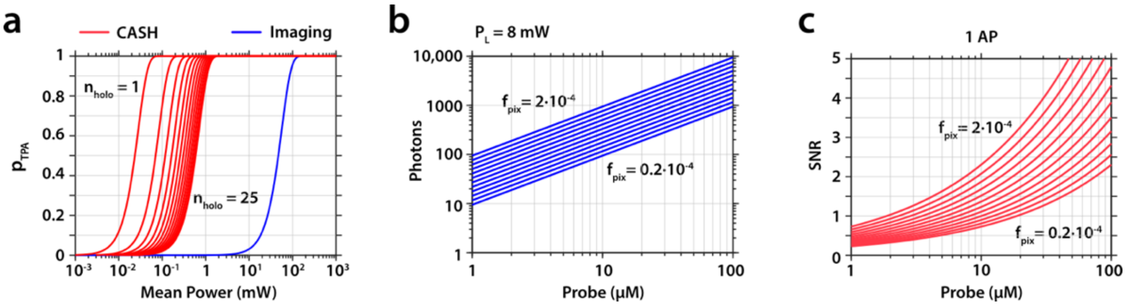

Supp. Fig. 14

***(a)** Probability of 2-photon absorption (pTPA) as function of mean power of excitation in the focal volume according to Eq. 3 in the imaging case* ($16\cdot10^{-6}$ duty cycle) as compared to CASH ($8\cdot10^{-9}$ duty cycle; 1,3,…25 spots). ***(b)** Number of estimated baseline photons (n_{ph}) per sample bin in the imaging case as function of cytosolic concentration of the probe and the fraction of pixels in the imaging frame (f_{pix}) used for extracting single cell responses. Values of f_{pix} vary 2, 1.6, 1.3, 1.1, 0.86, 0.7, 0.57, 0.46, 0.37, 0.3, 0.25 and 0.2 ($x10^{-4}$). **(c)** Expected SNR of the GCaMP6f response to single action potentials (1 AP) in the imaging case as function of probe concentration and f_{pix}. In the case of 500 x 500 pixels imaging frame size, the given values of f_{pix} correspond to ROI sizes of 50, 40, 33, 27, 22, 18, 14, 12, 9, 7, 6, and 5 pixels. The assumed sampling rate is 20 frames/s.*

SNR of CASH and imaging compared

The relationship of SNR between CASH and imaging acquisition follows immediately from Eqs. 1, 5 and 6:

$$\frac{SNR^C}{SNR^{Im}} = \alpha^C_{Im}\cdot\frac{\hat{P}^C_L}{P^{Im}_L} \quad \text{with} \quad \alpha^C_{Im} := \sqrt{\frac{f_{holo}\, r^{Im}_{acq}\, T^{Im}_L}{n_{holo}\, f_{pix}}}\;\frac{d^{Im}_L}{d^C_L} \qquad \text{(Eq. 7)}$$

with superscripts: *Im* = imaging and *C* = CASH. $\hat{P}^C_L$ = the total excitation power summed over all grid spots.

Eq. 7 has the advantage of eliminating the shared molecular and experimental parameters difficult to estimate, notably the two-photon cross section and cytosolic concentration of GCaMP. Since in CASH the SNR is independent of the sampling rate, α^C_{Im} in Eq. 7 does not explicitly depend on the sampling rate r^C_{acq}. However, $r^C_{acq} \gg r^{Im}_{acq}$ and therefore the GCaMP-CASH signal is, in general, highly oversampled with respect to the GCaMP imaging signal.

For a fair comparison of the noise, and thus SNR, we equalize the sampling rate by summing r^C_{acq}/r^{Im}_{acq} data bins of the CASH signal and impose $n^C_{Cell} = n^{Im}_{Cell}$:

$$\left[\frac{SNR^C}{SNR^{Im}}\right]_{eq} = \beta^C_{Im}\cdot\frac{\hat{P}^C_L}{P^{Im}_L} \quad \text{with} \quad \beta^C_{Im} := \sqrt{\frac{r^C_{acq}}{r^{Im}_{acq}}}\cdot\alpha^C_{Im} \qquad \text{(Eq. 8)}$$

In an imaging experiment, the pixel yield f_{pix} scales inversely with n^{Im}_{Cell}, the number of simultaneously imaged cells, according to $f_{pix} = \rho_C A_C l_z / n^{Im}_{Cell}$ with the segmentation length l_z measuring the axial length of the volume containing all cells positively segmented from the image frame. We estimate this length to correspond to the sum of the optical sectioning length of the microscope and the mean diameter of the nucleus in the cell population of interest. The holographic yield in CASH, on the other hand, equals $f_{holo} = A_C/(l_x l_y)$.

Substituting for f$_{pix}$ and f$_{holo}$ in Eq. 7 and Eq. 8 and making use of $r^{C}_{acq} = r^{C}_{data}/n^{C}_{Cell}$:

$$\alpha^{C}_{Im} = \sqrt{\frac{r^{Im}_{acq}}{r^{C}_{acq}}}\ \sqrt{\frac{n^{Im}_{cell}}{n^{C}_{Cell}}}\ \sqrt{\frac{r^{C}_{data}T^{Im}_{L}}{n_{holo}l_{x}l_{y}l_{z}\rho_{C}}}\ \frac{d^{Im}_{L}}{d^{C}_{L}} \qquad \text{(Eq. 9)}$$

and using $n^{C}_{Cell} = n^{Im}_{Cell}$:

$$\beta^{C}_{Im} = \sqrt{\frac{r^{C}_{data}\,T^{Im}_{L}}{n_{holo}l_{x}l_{y}l_{z}\rho_{C}}}\ \frac{d^{Im}_{L}}{d^{C}_{L}} \qquad \text{(Eq. 10)}$$

As f$_{pix}$, and thus α^{C}_{Im} and β^{C}_{Im}, depends on ρ_C, evaluation of Eqs. 9 and 10 needs a morphological model of the target cell distribution in the imaged field of interest.

The following table reproduces values of ρ_C from neuron reconstructions in mouse somato-sensory cortex (SS1) found in the literature[4].

Species	Brain Region	Neuron Type	ρ_C (x10^{-5} µm^{-3})
Mouse	SS1	L2/3 pyramid	8.24 ± 0.9
	SS1	L2/3 interneuron	1.122 ± 0.15
	SS1	L4 pyramid	13.78 ± 0.7
	SS1	L4 interneuron	1.16 ± 0.8
	SS1	L5 pyramid	5.13 ± 0.5
	SS1	L5 interneuron	1.04 ± 0.1

We calculate the scale factors α^{C}_{Im} and β^{C}_{Im} as function of cell density ρ_C from Eqs. 9 and 10. With β^{C}_{Im} known and using Eq. 8, we then estimate the ratio of the SNR offered by CASH and imaging under equalized conditions of sampling as function of cell density ρ_C and relative excitation power $\hat{P}^{C}_{L}/P^{Im}_{L}$.

Parameters used in evaluating α^{C}_{Im}, β^{C}_{Im} and $\lfloor SNR^{C}/SNR^{Im} \rfloor$:

r^{Im}_{acq}	*20 Hz*	n_{Holo}	*25*	l_z	*7 µm*
r^{C}_{data}	*40,000/s*	l_x	*16 µm*	d^{C}_{L}	$8\cdot 10^{-9}$
T^{Im}_{L}	*12.5 ns*	l_y	*16 µm*	d^{Im}_{L}	$16\cdot 10^{-6}$

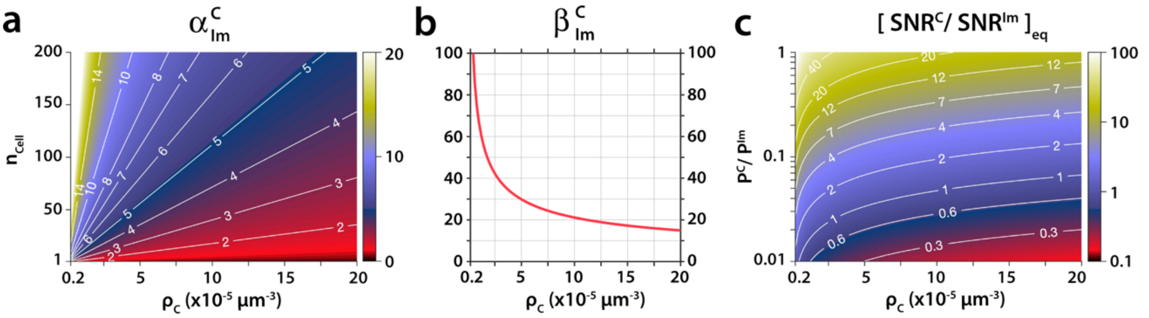

Supp. Fig. 15

***(a)** Scale factor α^{C}_{Im} as function of the cell density, ρ_C, and number of imaged cells, n^{Im}_{Cell}, for a 5x5 spot grid covering a 16x16 µm^2 space. **(b)** Scale factor β^{C}_{Im} as function of the cell density ρ_C. **(c)** Ratio of expected SNRs in CASH versus imaging with equalized sampling as function of cell density ρ_C and the ratio of the mean excitation power in CASH (5x5 grid) versus imaging, $\hat{P}^{C}_{L}/P^{Im}_{L}$.*

β^{C}_{Im} exceeds α^{C}_{Im} up to one order of magnitude (Supp. Fig. 15a,b) as expected from the temporal oversampling of the GCaMP signal in CASH with respect to the assumed 20 Hz rate of image frame acquisition. By taking into account maximally sustainable excitation level, limited in CASH by onset of probe saturation (Supp. Fig. 13 and associated text) and in imaging by tissue heating (Supp. Fig. 14 and associated text), and not withstanding other possible limiting effects, we consider as useful power range $0.03 < \hat{P}^{C}_{L}/P^{Im}_{L} < 0.3$. In this range, the estimated effective SNR_{eq} in CASH may exceed the SNR in imaging by up to a factor twelve (Supp. Fig. 15c).

In our estimation above (Supp. Fig. 13 and 14), in particular, the power ratio was 0.05 ($\hat{P}^{C}_{L} = 0.42\,mW$, $P^{Im}_{L} = 8\,mW$). This results in SNR of similar magnitude ($[\mathrm{SNR}^{C}/\mathrm{SNR}^{Im}]_{eq} = 1.2$) in case of a target cell density resembling the pyramidal neuron population in the supra-granular layer of mouse cortex[4] ($\rho_C = 8.2\cdot10^{-5}\ \mu m^{-3}$), and about three times higher SNR in case of the same layer interneuron population[4] ($[\mathrm{SNR}^{C}/\mathrm{SNR}^{Im}]_{eq} = 3.1$; $\rho_C = 1.1\cdot10^{-5}\ \mu m^{-3}$), for instance.

Spatial resolution of the 3DScope acousto-optic light modulator

The spatial resolution of an AOD defines the maximum number of distinct spots the AOD permits to create in the far field or, equivalently, in the focal plane of an added ideal focusing element which is: $N = \Delta\Theta_{scan}/\Delta\Theta_{beam}$, where $\Delta\Theta_{scan}$ is the AOD angular tuning range and $\Delta\Theta_{beam}$, the angular spread of the laser beam[5]. $\Delta\Theta_{scan}$ can be expressed as $\Delta\Theta_{scan} = M_{ang}\,\lambda/v\,\Delta f = 4.2°$, with Δf, the total scan bandwidth (36 MHz), M_{ang}, the angular magnification (1.5) of the AOD-objective relay, and λ, the wavelength (900 nm). In the diffraction limit, $\Delta\Theta_{beam} = M_{ang}\cdot 1.22\,\lambda/D_{AOD}$, with D_{AOD}, the AOD aperture diameter (15 mm). Therefore, $N_{diff} \approx 680$ for λ = 900 nm. In the 3DScope, the laser beam is additionally broadened by angular chromatic dispersion at AOD side band frequencies while angular dispersion is compensated for the acoustic carrier wave. In this case, $\Delta\theta_{beam} \leq M_{ang}\cdot\Delta\lambda/v\cdot\Delta f/2$, with $\Delta\lambda = 0.44\,\lambda^2\cdot\tau_{laser}/c$, the FWHM wavelength broadening of a Gaussian laser pulse (6 nm for τ_{laser} = 200 fs) and ± $\Delta f/2$, the extremal frequencies in the side bands. Thus, $N_{disp} \geq 2\,c\tau_{laser}/(0.44\cdot\lambda) \approx 300$. Notably, the diffraction and dispersion limits, N_{diff} and N_{disp} are far below the digital frequency resolution ($N_{digital} = 6\cdot10^5$) of the DDS (59.6 Hz/bit; 23 bit; 36 MHz AO bandwidth). Finally, the FM resolution depends on the pixelization of the AOD-shaped wavefront as a consequence of RF-AOD being synthetized on a 14 MHz DDS write clock. Given the 15 mm size of the aperture, the discretization grid has a size of $n_{pix} = 324$. The digital pixelization limits the FM spatial frequency in the AOD pupil to $\pm 0.5\,n_{pix}/D_{AOD}$. Therefore, the maximal spot number N_{pix} due to the pixelation limit becomes $N_{pix} < 0.5\,n_{pix} \approx 162$.

Supplementary References

1. Xu, C. & Webb, W. W. Multiphoton excitation of molecular fluorophores and nonlinear laser microscopy. in *Topics in Fluorescence Spectroscopy* vol. 5 471–540 (Plenum Press, 1997).
2. Tsai, P. S. & Kleinfeld, D. In Vivo Two-Photon Laser Scanning Microscopy with Concurrent Plasma-Mediated Ablation Principles and Hardware Realization. in *In Vivo Optical Imaging of Brain Function* (ed. Frostig, R. D.) (CRC Press/Taylor & Francis, 2009).
3. Drobizhev, M., Makarov, N. S., Tillo, S. E., Hughes, T. E. & Rebane, A. Two-photon absorption properties of fluorescent proteins. *Nat. Methods* **8**, 393–399 (2011).
4. Lefort, S., Tomm, C., Floyd Sarria, J.-C. & Petersen, C. C. H. The Excitatory Neuronal Network of the C2 Barrel Column in Mouse Primary Somatosensory Cortex. *Neuron* **61**, 301–316 (2009).
5. Iyer, V., Losavio B.E., & Saggau, P. Compensation of spatial and temporal dispersion for acousto-optic multiphoton laser-scanning microscopy. *J. Biomed. Opt.* **8**, 460–471 (2003).